The mesoscale atmospheric analysis of the Boothbay 28 Oct 2008 event

Project: TMEWS
Type: Report
Date: 03/31/2012
Author: Kristian Horvath, DHMZ

1. Introduction

Analysis of the tide gauges and buoy data suggested that the large sea level oscillations observed around 19 UTC 28 Oct 2008 in Boothbay harbor may be considered a meteotsunami. The rapid pressure oscillations were estimated to travel at the phase speed of 24 m/s. In addition, the synoptic analysis showed the presence of a wave-like cloud bands crossing over the Boothbay harbor between 18 and 19 UTC, with the speed of 30-32 m/s. Both analyses suggest the pressure perturbation was moving roughly SSE-NNW (SE-NW).

To study the mesoscale atmospheric features prior to and during the meteotsunami, the analysis was performed with the mesoscale model and available in-situ, remote sensing and reanalysis data. The mesoscale model employed in this study was a non-hydrostatic, fully-compressible Advanced Research version of the Weather Research and Forecasting model (WRF-ARW).

Section 2. describes the model setup and sensitivity experiments. Section 3. studies the sensitivity of model simulations to different sources of initial and lateral boundary conditions data and verifies the simulations. Sensitivity to simulation time-horizon is presented in section 4., followed by the analysis of sensitivity to microphysical schemes in section 5. and convective schemes in section 6. Additional analysis and discussion is provided in section 7., while section 8. concludes the report.

2. Description of the model setup and sensitivity experiments

The control mesoscale model setup consists of 3 nested domains (Fig.1), with the horizontal grid spacing of 9 km, 3 km and 1km respectively, and 40 vertical levels. The set of parametrizations used in

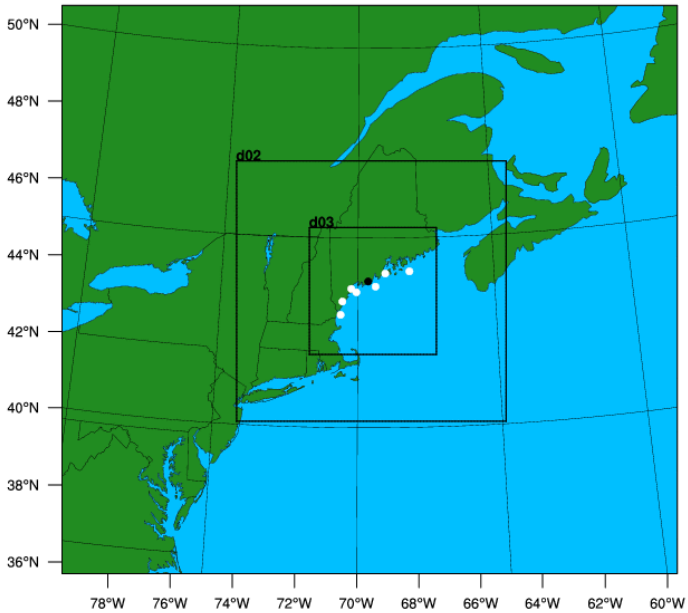

Figure 1: The computational domains of the WRF model. White circles denote sites of interest (buoy and tide gauge stations) and the black dot denotes the Boothbay harbor. The buoy closest to the Boothbay was 44032 (E01).

the control WRF model setup included Morrison two-moment microphysics scheme, Grell-Devenyi cumulus parametrization scheme (only outermost domain), and Mellor-Yamada-Janjic PBL. Dudhia sheme was used for short-wave radiation, and the Rapid Radiative Transfer Model was chosen to parametrize long-wave radiation. The Noah land-surface model was used to simulate the vertical transport of soil moisture and heat. The model was set up not to damp vertical velocities and with reduced amount of explicit smoothing.

The exact conditions leading to meteotsunamis are often hard to simulate with current state-of-the art mesoscale models, such as WRF. Therefore, the numerical experiments assessed the sensitivity of mesoscale simulations to:

1) initial and boundary conditions (ICs and LBCs), since the atmospheric conditions generating meteotsunamis are hard to model and predict, and small uncertainties in ICs and LBCs may have a large influence on mesoscale simulation results.
2) convective parametrization, since meteotsunamis may occur associated with convective activity, such as the Boothbay event. In addition, some of the mechanisms proposed for generating atmospheric conditions favoring meteotsunamis is wave-CISK, the interaction between

convection and internal gravity-waves (IGWs).

3) microphysics parametrization, since these scheme controls the explicit precipitation (both convective and stratiform) in higher-resolution modeling domains when convection parametrization is switched off.
4) nesting strategy, which may be one-way or two-way depending on the model or model setup (some models such as WRF have both options). In the one-way nesting setup the results from higher resolution domains do not interact with results from lower resolution domains. In two-way nesting the results from the higher resolution domains propagate to lower resolution domains. Thus, two-way interaction may be important flow evolution in general, and especially for some of the proposed meteotsunami mechanisms, such as the trapping of IGWs or their interaction with the convection (wave-CISK). On the other hand, if IGWs of wavelengths smaller than 10 dx do exist in the higher resolution domains, they may be aliased in the lower resolution domain (with a typical nesting ratios of 3 or 4). Though two-way nesting most often should lead to more accurate results, most implementations of the operational numerical weather prediction models use one-way nesting. Therefore, the analysis of results using the one-way nesting strategy is important for assessment of potentials for numerical prediction of atmospheric conditions related to meteotsunamis.

3. Verification of model results and sensitivity to initial and lateral boundary conditions

In this part of verification and sensitivity analysis, the mesoscale model simulations were initialized at 12 UTC 28 Oct 2008 for a 12-hr period. To assess the role and sensitivity to initial and lateral boundary conditions (IC and LBC) 6 sensitivity simulations were performed using 3 different sources of global model data. In addition, the analysis included sensitivity to the type of interaction among domains – that is one way or two-way nesting. IC and LBC were provided by the following sources:

1. North-American Regional Reanalysis (NARR, grid spacing ~ 0.333 deg)
2. ERA-Interim (T255, grid spacing ~ 0.75 deg)
3. ECMWF operational analysis, ECMWF_OA (T799, grid spacing ~ 0.22 deg).

The first two are reanalysis data, which use a long cut-off window for data assimilation (meaning more data is used in the process of data assimilation) at the lower grid spacing, while the second is the

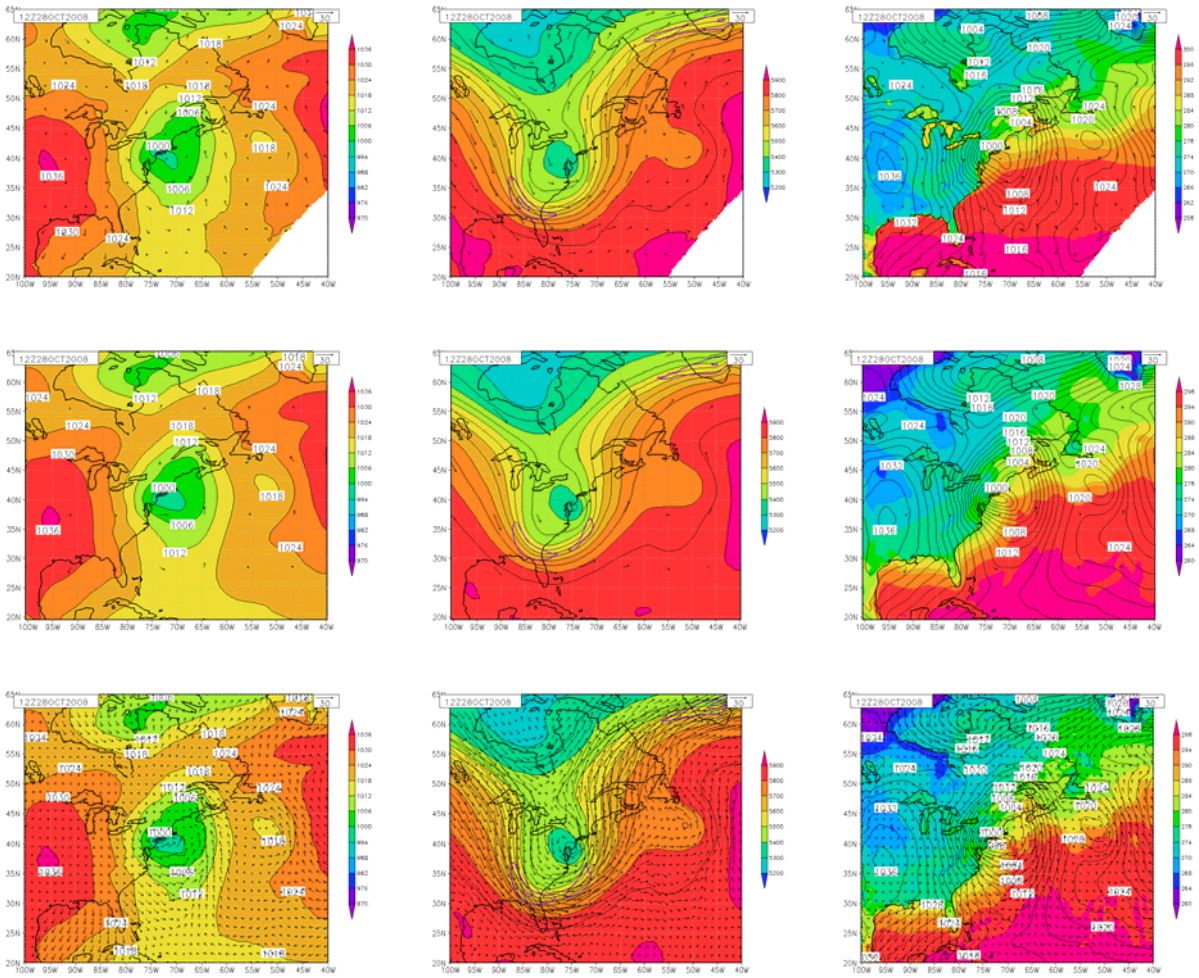

Figure 2: Mean-sea level pressure (both shaded and black contours) and 10 m wind vectors (left), geopotential height (both shaded and black contours), wind vectors and wind speed (purple contours starting at 50 m/s, interval 10 m/s) at 300 hPa (center) and T2 (shaded), MSLP (contours) and 10 m wind vectors from NARR (top), ERA-Interim (middle) and ECMWF_OA (bottom) at 12 UTC 28 Oct 2008. Note the change in color shading scale for temperature.

operational short cut-off analysis (meaning less data is used) at the higher grid spacing. All three datasets are shown in Figs 2, 3, and 4. Larger-scale circulation of all datasets was similar: a deep cyclone with a defined thermal structure (warm and cold cyclone sectors) was at 12 UTC 28 Oct 2008 present southeast of the Boothbay area (Fig. 2), and moved towards the north-east (Figs 3.,4.). The subtle differences between these datasets however did exist. E.g., note the differences in position and shape of warm sector, fronts, location of the jet streak and its intensity, and the depth of the cyclone centre. Indeed, Boothbay seemed to be in the cold sector of the cyclone in NARR, and in the warm

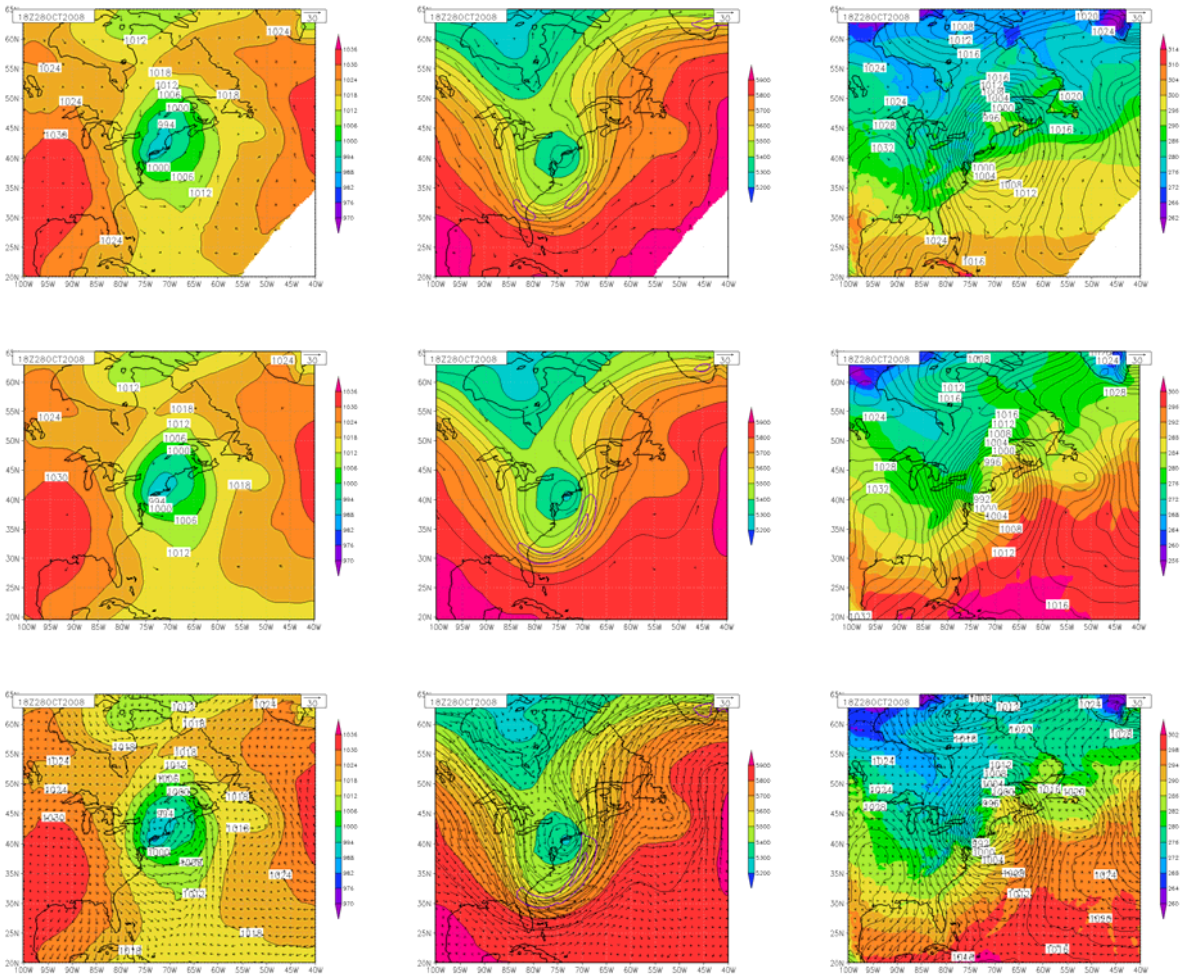

Figure 3: As in Figure 2., but at 18 UTC 28 Oct 2008. Note the change in color shading scale for temperature.

sector in ECMW and ERA-Interim data. These differences were large enough to cause an entirely different mesoscale flow evolution. The complete list of experiments aimed at assessing the sensitivity of mesoscale simulations to the source if ICs and LBCs is listed in Table 1.

Table 1: List of experiments performed to assess the role of IC and LBC.

EXP. NO.	1	2	3	4	5	6
IC&LBC	NARR	NARR	ERA-Interim	ERA-Interim	ECMWF-OA	ECMWF-OA
Nesting type	1-way	2-way	1-way	2-way	1-way	2-way

A comparison of mesoscale model results was performed on measured radio-sounding data, reanalysis fields, measured time-series data from buoys, radar and satellite imagery. A comparison of modeled WRF results (12-hr simulation) and measured radio-sounding data at 00 UTC 29 Oct 2008 is shown in Fig. 5.

Generally, all models performed satisfactorily, but overestimated the moisture content in the upper-troposphere. Some differences were notable: at Gray, which is the closest radio-sounding to Boothbay, the moisture content of the lower and middle layers was underestimated in simulation driven by NARR data – this is in accordance with what the aforementioned notion that in NARR reanalysis data,

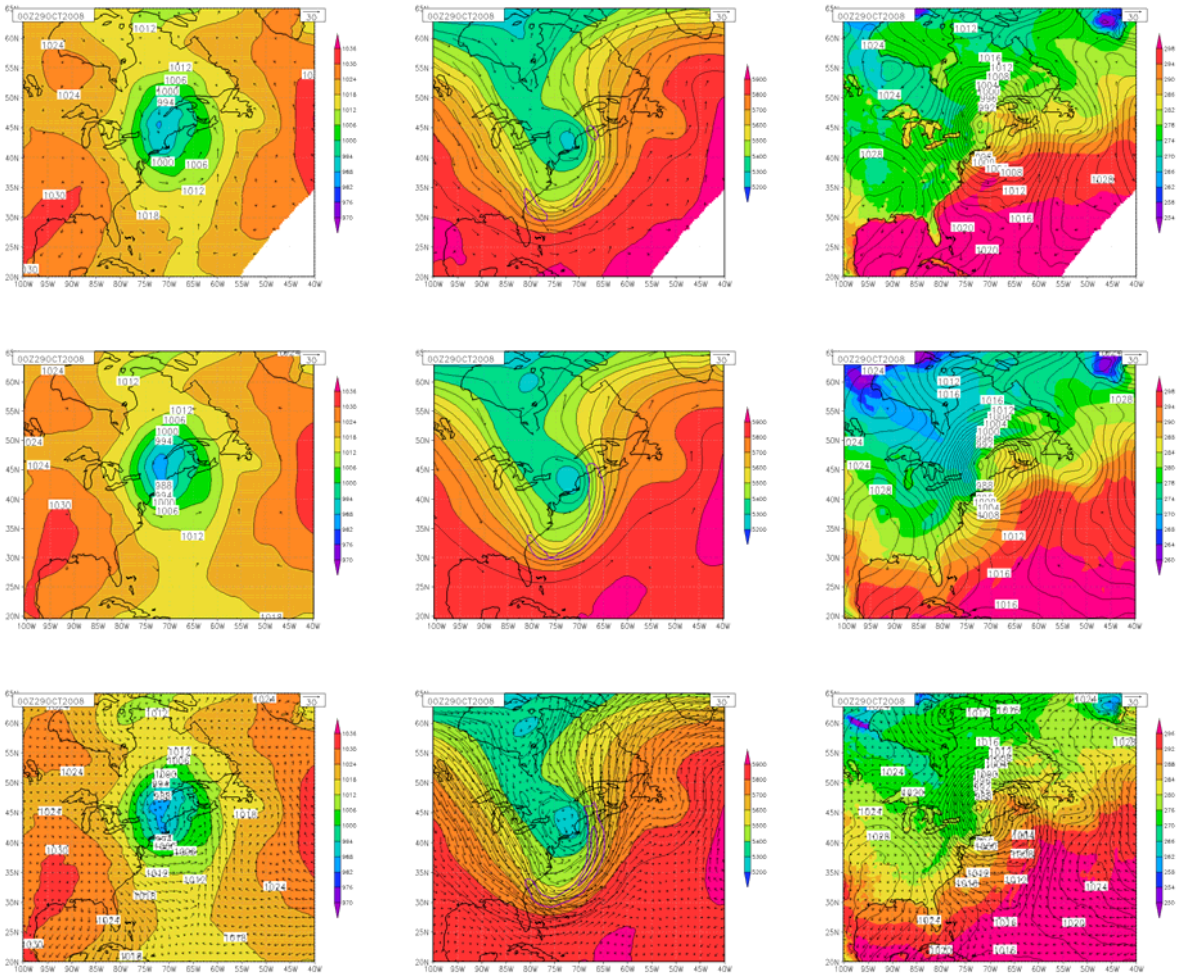

Figure 4: As in Figure 2., but at 00 UTC 29 Oct 2008. Note the change in color shading scale for temperature.

Boothbay was not in the warm cyclone sector. On the other hand, the simulation driven with NARR data performed the best farther north at Yarmouth.

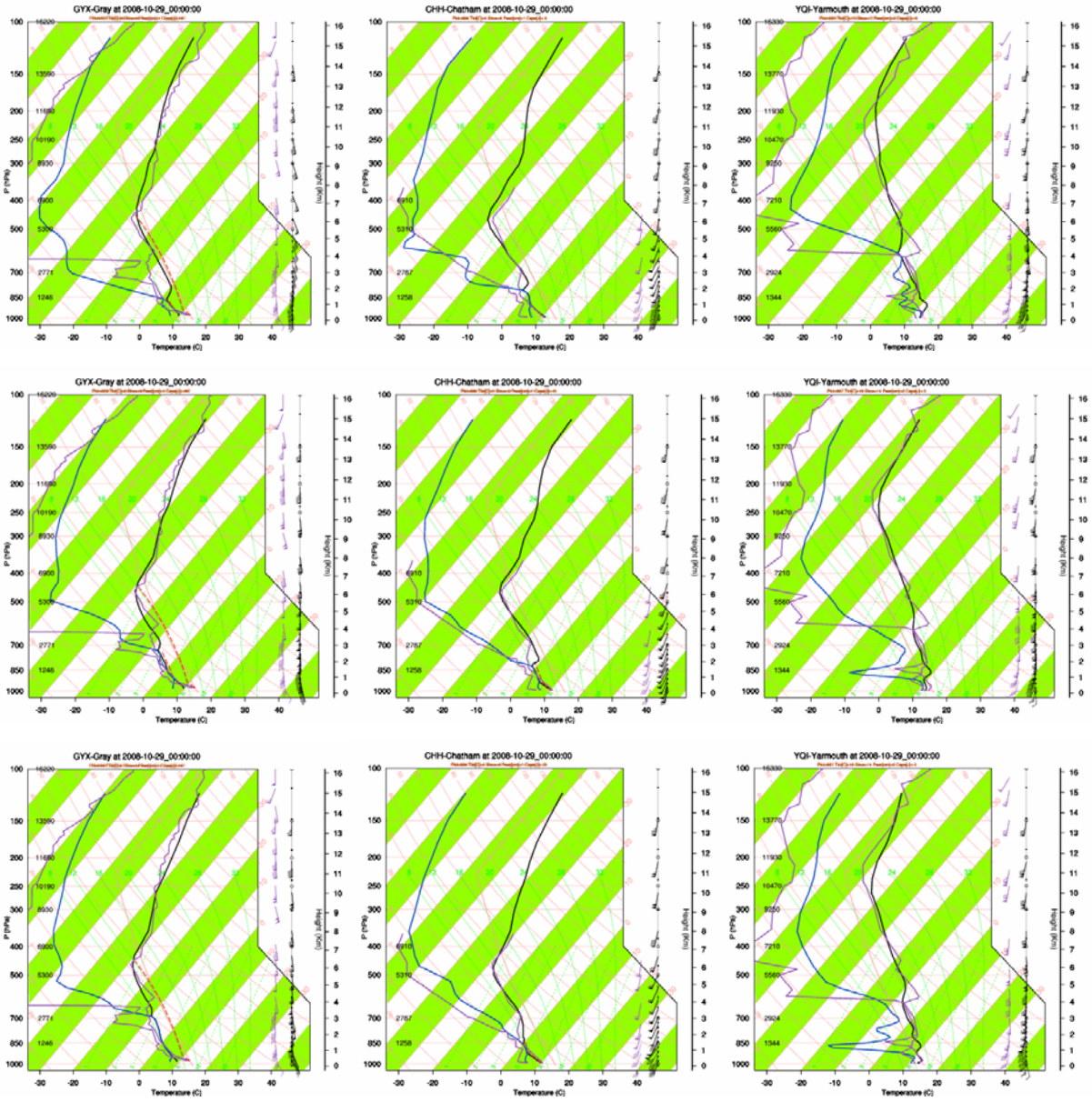

Figure 5: Skew-T diagrams from one-way nesting WRF domains 2 (dx=3 km) for Gray, Chatham and Yarmouth at 00 UTC 29 Oct 2008 for NARR (top), ERA-Interim (middle) and ECMWF_OA (bottom) initial and boundary conditions, with one-way nesting. Measured data is in purple color and modeled in blue (dew point temperature) and black (temperature and winds).

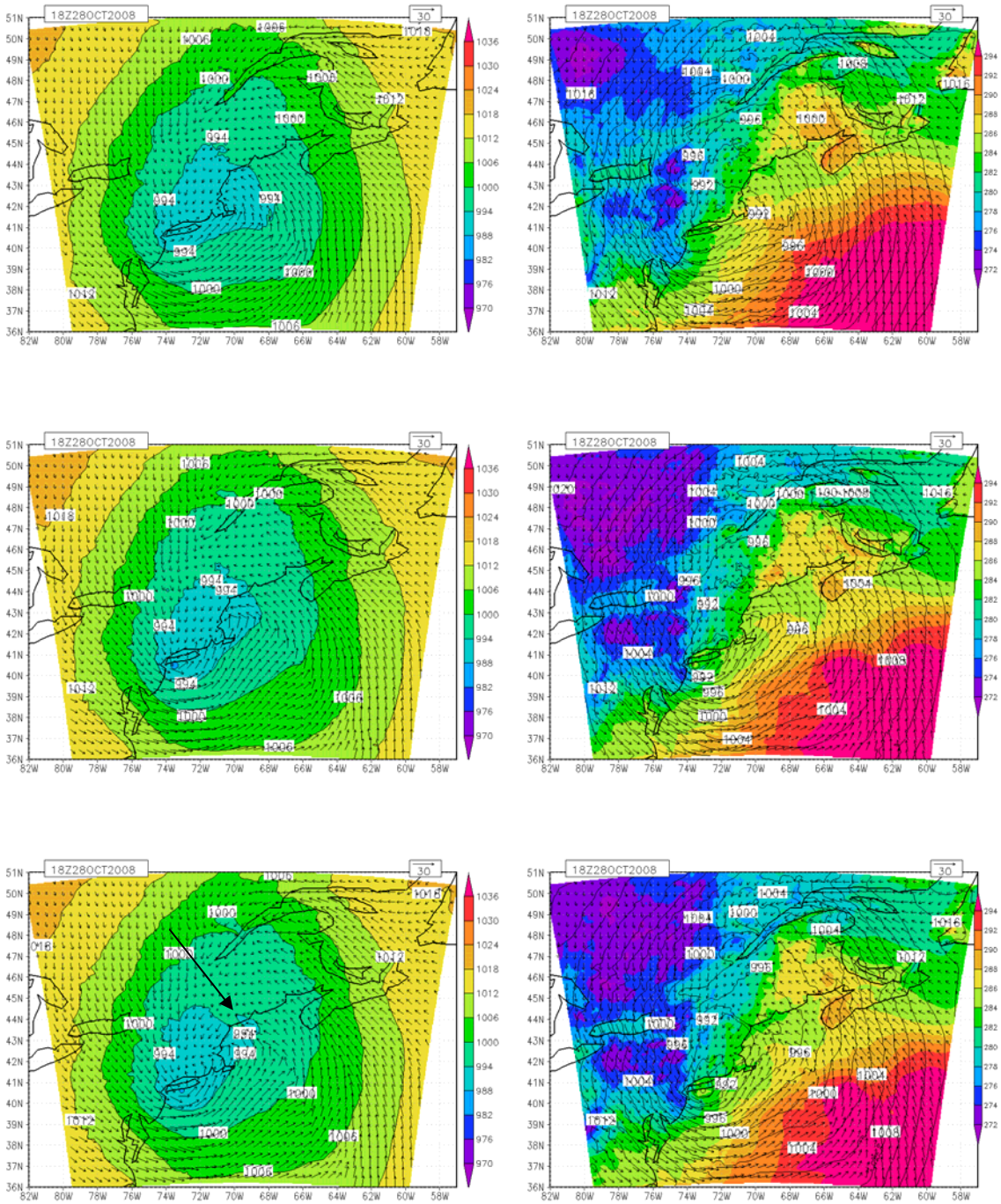

Figure 6: MSLP (shaded, contours) and 10 m wind vectors (left) and T2 (shaded), MSLP (contours) and 10 m wind vectors (right) for one-way nesting WRF simulations (one-way nesting) driven with NARR (top), ERA-Interim (middle) and ECMWF_OA (bottom). The black arrow denotes the pronounced pressure disturbance (lower-left panel).

At 18 UTC, model at grid spacing of 9 km successfully simulated the main synoptic features and the depth of the cyclone southwest of the target area, regardless of the source of the ICs and LBCs (Fig. 6). Also, all models simulated a discontinuity (shear) line close to the Boothbay which extended from northwest to southeast. However, there were evident differences in the intensity and position of the shear line. In addition, only the WRF simulation driven with ECMWF_OA reproduced a distinct mesoscale pressure disturbance near Boothbay (marked by the arrow in Fig. 6).

Time series of measured and modeled buoy data were analyzed for buoy stations 44032 (E01), 44033 (F01), 44034 (I01), 44030 (B01), CO2 and Wells, the buoy stations in the area with data available with a 10-min or higher temporal resolution (Fig. 7). For point verification of model simulations, model output was extracted at runtime for most of the above station locations every time step i.e. every 6 s in

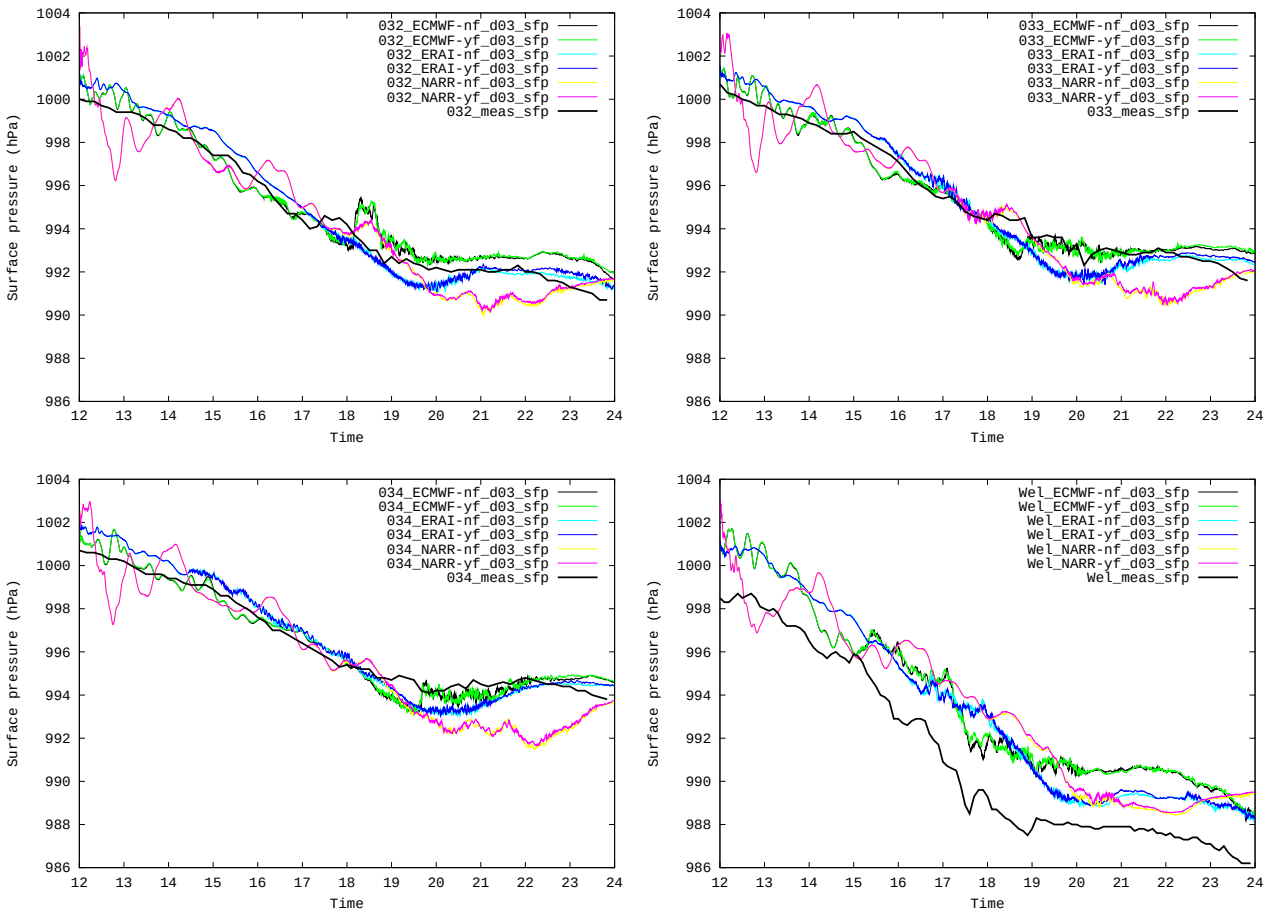

Figure 7: Time-series of measured and modeled data at stations 44032, 44033, 44034 and Wells. "Yf" on the legend denoted two-way nesting, and "nf" denotes one-way nesting model simulations.

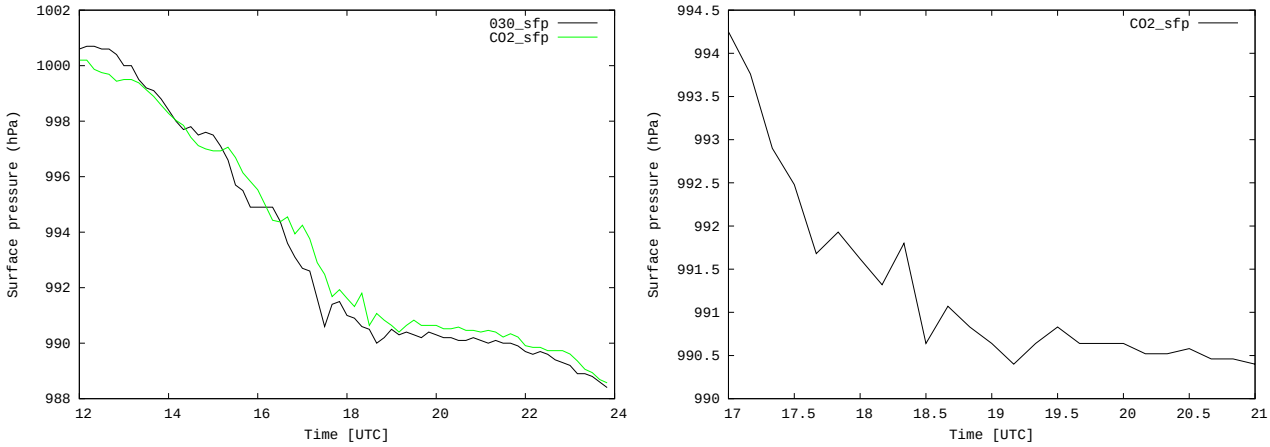

Figure 8: Time-series of measured data at stations CO2 and 44030 (B01) from 12 UTC 28 Oct 2008 - 00 UTC 29 Oct 2008 (left) and from 17 UTC 28 Oct 2008 - 21 UTC 28 Oct 2008 (right). Note the change in color line for station CO2.

domain 3 (grid spacing 1 km). Missing from the on-line database was data for GOMOOS buoy CO2 (43 34.06'N, 070 03.50'W), which was collected later (courtesy of John Jensenius, NOAA). Therefore, this data could not be compared with model results in the same manner. The station closest to Boothbay is 44032, which is ~ 20 km southeast of the Boothbay harbor.

First, it is evident that in all model experiments the large-scale pressure tendency (decrease) was accurately simulated, though apparently at Wells with a delay of 1 hour. Second, measurements at buoy 44032 and model simulations showed much larger pressure oscillations (that is standard deviations) between 17 UTC and 21 UTC than in other periods, suggesting the internal gravity-wave (IGW) activity may had occurred aloft. Data from buoys CO2 and 44030 pointed to pressure changes larger than 1 hPa/10 min (Fig. 8) associated with the passage of one of the initial squalls as well as large pressure variability during the period prior to the meteotsunami. Finally, it appears that larger pressure tendencies (in a 10-min periods) were generally found to the west rather than to the east of Boothbay.

While WRF driven with NARR and ECMWF_OA in hours around and prior to Boothbay meteotsunami (18-19 UTC) showed rapid pressure changes, the simulation driven with ERA-Interim data showed a smooth decrease of pressure without rapid pressure changes on the scales relevant to meteotsunamis. Thus, we conclude that both simulations driven with ERA-Interim data are of limited usability for our analysis. Finally, we note that at buoy station 44032, WRF model driven with both

NARR and ECMWF_OA data showed an isolated peak in mean-sea-level pressure value between 18 UTC and 19 UTC. This peak was, however, not so intensive in the measured data, perhaps due to very localized nature of the event and potential spatial errors of the mesoscale model. This will be further verified later on.

Since a precipitation system (squall line) moved over the Boothbay area around the time of meteotsunami, the analysis of the outgoing long-wave radiation was compared with the GOES IRW imagery. This satellite imagery showed a "wave-like" structure which gave clues of the IGW activity aloft (Fig. 9, for satellite analysis see Natasa's report). The associated wave-lengths estimated from fugures seem to be 60-70 km. The comparison with model simulations suggests that WRF results driven with ERA-Interim and ECMWF_OA data were of reasonable accuracy in simulating the movement of the squall line (Figs. 9, 10). In contrast, neither the shape nor the evolution (animations not shown) of the cloud band were satisfactorily simulated in WRF simulation driven with NARR data. Finally, none of the simulations reproduced the "wave-like" structure evident in the satellite imagery. However, in ECMWF_OA there was evidence of a wave-like structure over the ocean south of the Boothbay area; however, the associated wave-lengths were much smaller than the ones seen on the satellite imagery.

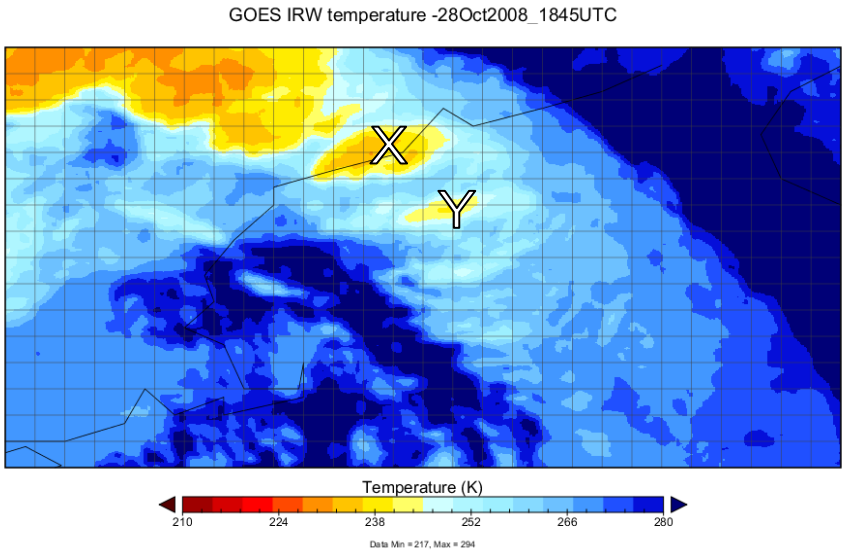

Figure 9: GOES IRW temperature at 18:45 UTC 28 Oct 2008 (taken from Nataša's report). Letters "X" and "Y" denote wave-like structure of lower temperatures.

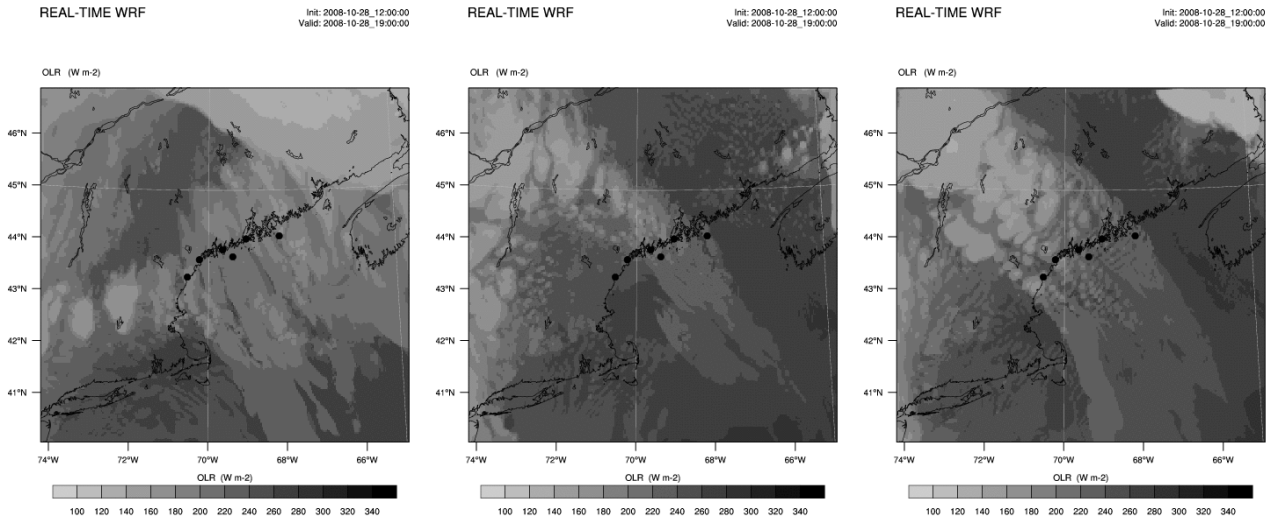

Figure 10: Outgoing long-wave radiation (W/m2) in WRF simulations (one-way nesting) driven by NARR (left), ERA-Interim (middle) and ECWMF_OA (right) data at 19 UTC 28 Oct 2008.

More detailed insight into the evolution of the squall line is illustrated by the radar imagery (Fig. 11, courtesy of John Jensenius, NOAA). The entire system moved approximately from south to north, but internal convective structures had northwestward direction (as indicated by letters A, B and C in Fig. 11) and moved faster than the system itself. It appears that areas denoted B and C may correspond to areas X and Y on the satellite images. Furthermore, near the time of meteotsunami (19 UTC), high reflectivity denoted B had just passed over Boothbay, followed by the area of no reflectivity and the area of high reflectivity denoted C farther offshore. Indeed, the convective area C passed slightly east of Boothbay in next minutes. This suggests that Boothbay meteotsunami took place at the time when the rear edge of the precipitation system was passing over the area. Finally, near the SE end of the precipitation system at 19 UTC 28 Oct 2008, reflectivity lines oriented SW-NE point to the IGW activity in the area. The horizontal wave-length of these reflectivity lines, however, is much shorter than the wave-like structure found in satellite data and seem to correspond better to the outgoing long-wave radiation distribution in the WRF simulations. We will pay attention to this phenomenon also later in the analysis.

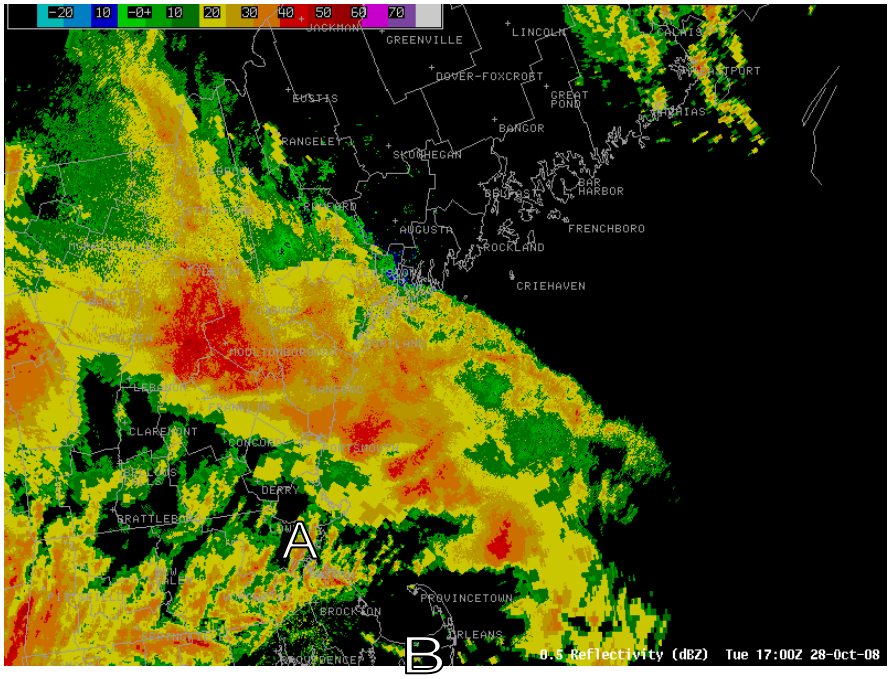
-20 10 -0+ 10 20 30 40 50 60 70
GREENVILLE
LINCOLN
DOVER-FOXCROFT
GREAT POND
BANGOR
RANGELEY
SKOWHEGAN
BAR HARBOR
BRUNSWICK
AUGUSTA
FRENCHBORO
ROCKLAND
CRIEHAVEN
MOULTONBOROUGH
SANFORD
CLAREMONT
CONCORD
DERRY
BRATTLEBORO
A
PROVINCETOWN
BROCKTON
ORLEANS
B
0.5 Reflectivity (dBZ) Tue 17:00Z 28-Oct-08

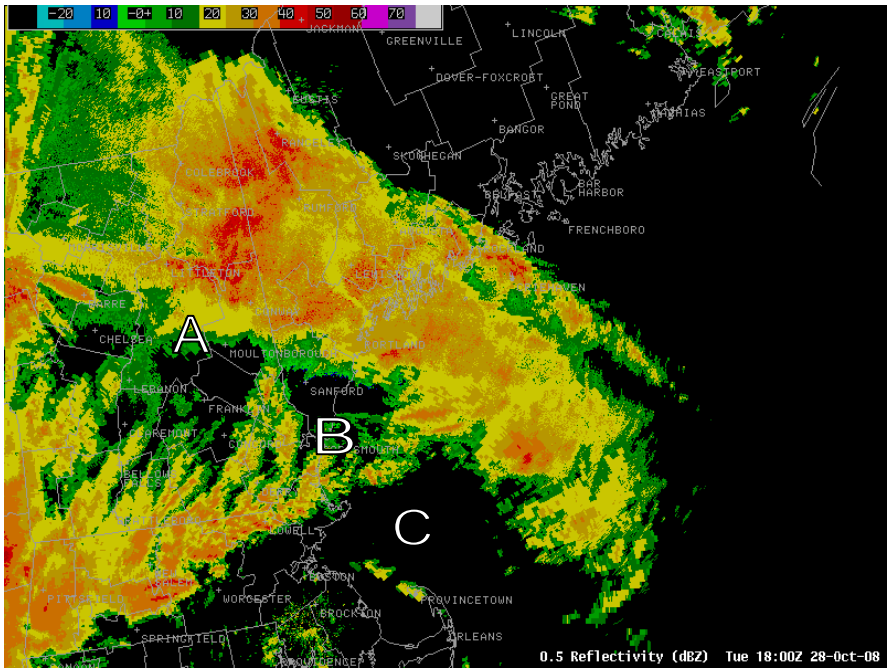
-20 10 -0+ 10 20 30 40 50 60 70
GREENVILLE
LINCOLN
DOVER-FOXCROFT
GREAT POND
BANGOR
SKOWHEGAN
BAR HARBOR
BRUNSWICK
FRENCHBORO
COLEBROOK
CHELSEA
A
MOULTONBOROUGH
SANFORD
B
C
WORCESTER
PROVINCETOWN
BROCKTON
SPRINGFIELD
ORLEANS
0.5 Reflectivity (dBZ) Tue 18:00Z 28-Oct-08

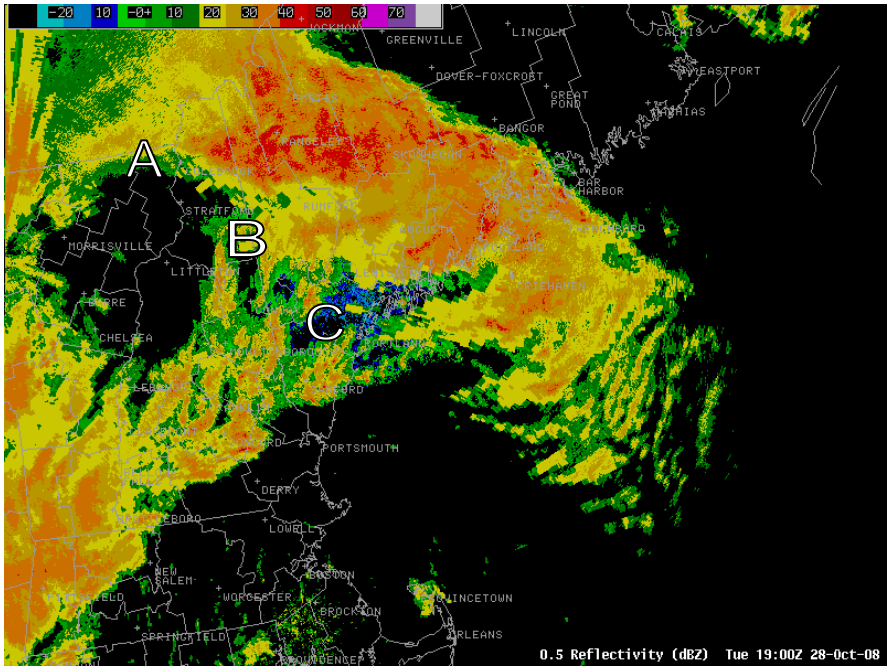

Figure 11: Radar reflectivity of the precipitation system passing over Boothbay on 17 UTC (top), 18 UTC (medium) and 19 UTC (bottom) on 28 Oct 2010. Letters "A", "B" and "C" denote the movement of the individual convective structures within the squall line (inferred from animations, 6-min data frequency).

Model simulated radar reflectivity at 19 UTC 28 Oct 2008 show that simulations driven with ERA_INTERIM and ECMWF_OA were much more accurate than the simulation driven with NARR data (Fig. 12). Simulations driven by ERA_INTERIM and ECMWF_OA were generally similar, however, there were notable differences. The reflectivity structures in simulations driven with ERA-Interim lacked intensity over the ocean south of the Boothbay area. In addition, the width of the squall line crossing Boothbay considerably narrowed towards the SE, in contrast to simulation driven with ECMWF_OA, in there is more convection over the ocean south of Boothbay and the width of the precipitation system remains constant towards the SE, such as in the radar imagery. On the other hand, convective activity farther offshore south of Boothbay in simulation driven with ECMWF_OA seems excessive. Neither of the simulations reproduced reflectivity lines oriented SW-NE near the southeast end of the precipitation system.

The mean sea level pressure and wind vectors for simulations driven with the NARR, ERA-Interim and ECMWF_OA are shown in Figs. 13, 14 and 15. At the approximate time of the Boothbay event (19 UTC 28 Oct 2008), elongated high-pressure band associated with the precipitation system moved over

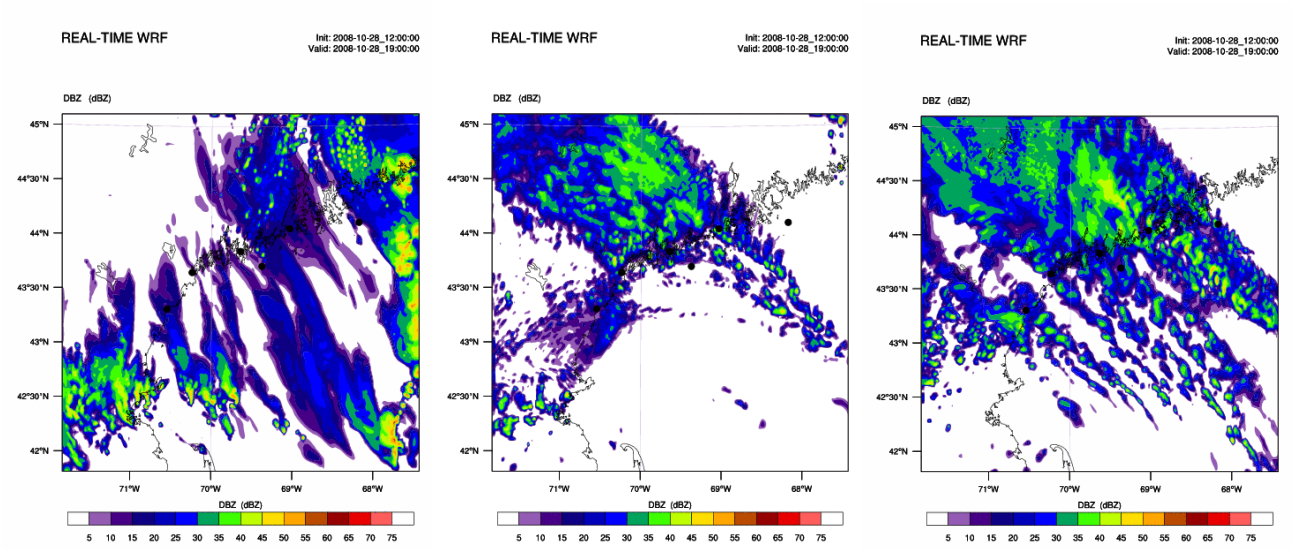

Figure 12: Simulated radar reflectivity of the precipitation system passing over Boothbay at 19 UTC 28 Oct 2010 inferred from one-way nesting WRF simulations driven with NARR (left), ERA-Interim (center) and ECMWF_OA (right). Letter "A" denotes movement of the individual cell system (inferred from animations, 6-min data frequency).

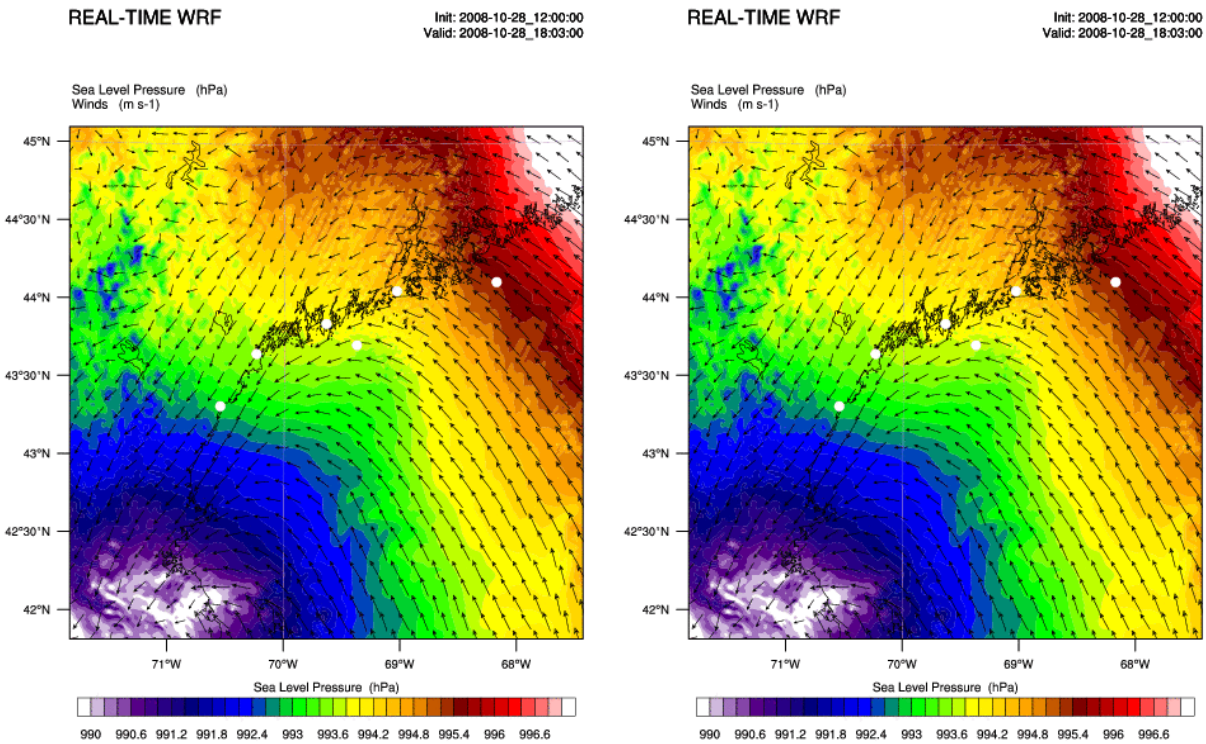

Figure 13: Simulated MSLP and 10 m wind vectors at 18 UTC 28 Oct 2008 (left) and 19 UTC 28 Oct 2008 (right) in the one-way nesting WRF simulation driven with NARR data.

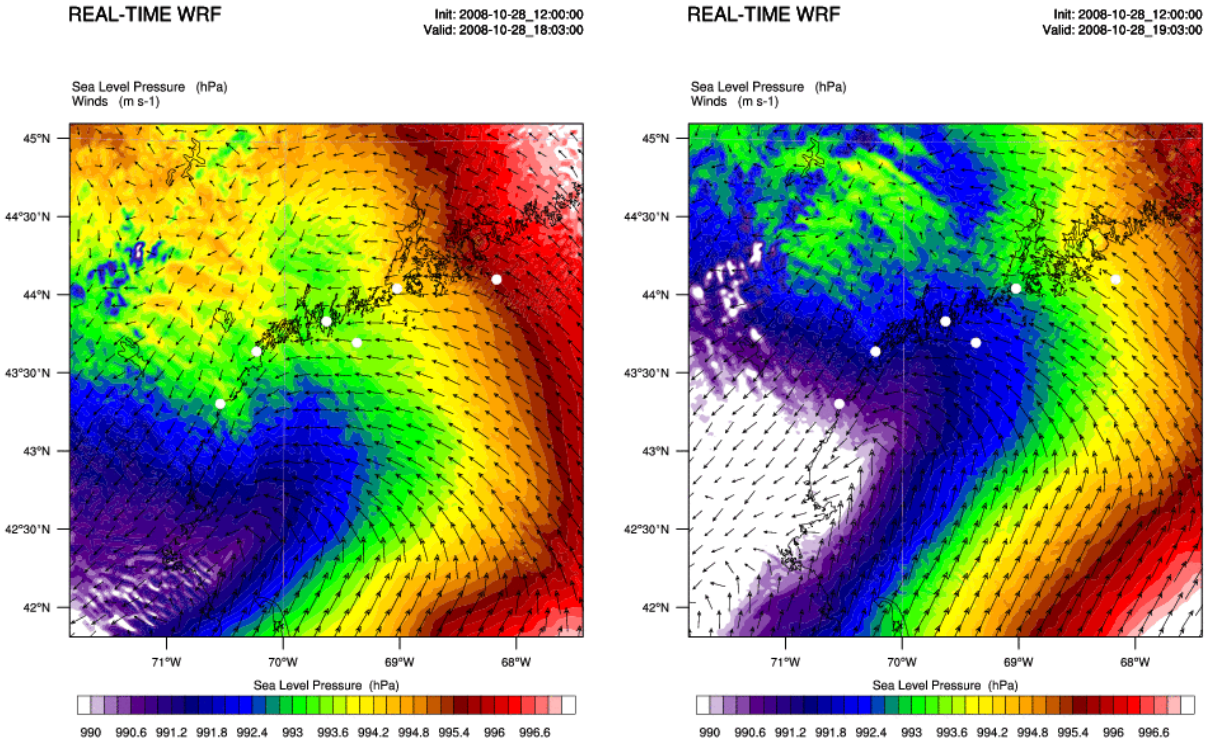

Figure 14: Simulated MSLP and 10 m wind vectors at 18 UTC 28 Oct 2008 (left) and 19 UTC 28 Oct 2008 (right) in the one-way nesting WRF simulation driven with ERA-Interim data.

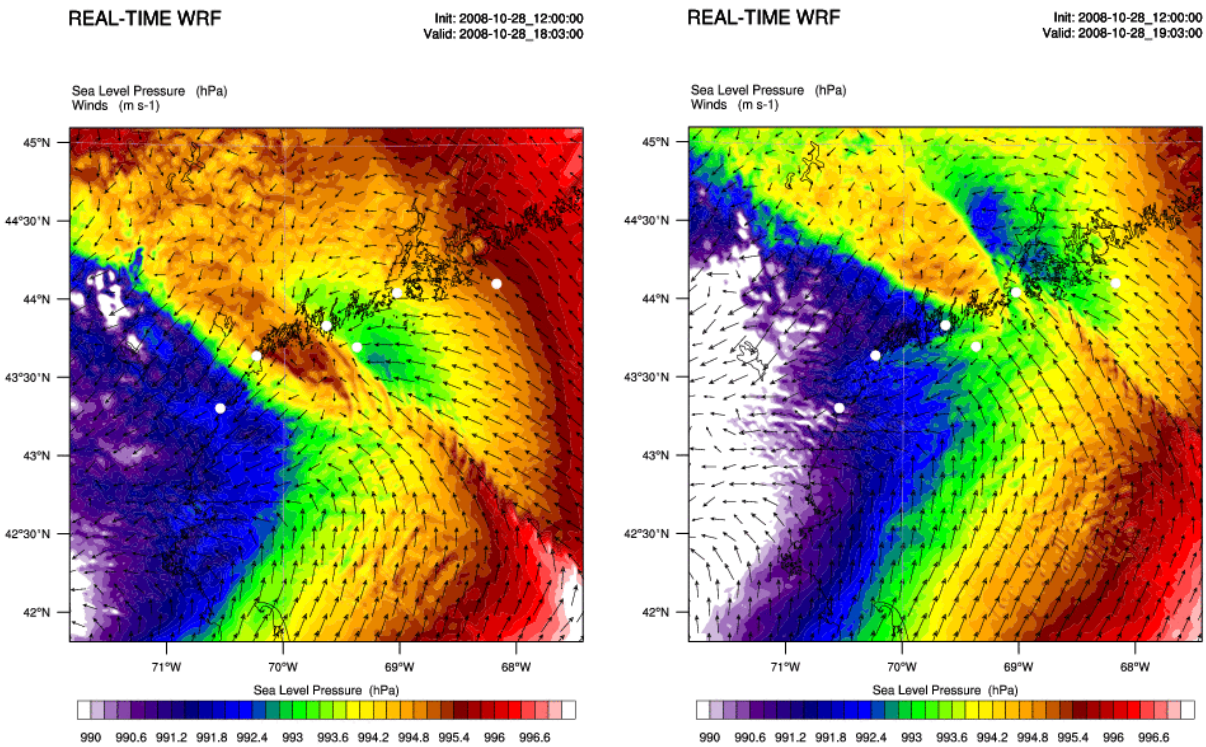

Figure 15: Simulated MSLP and 10 m wind vectors at 18 UTC 28 Oct 2008 (left) and 19 UTC 28 Oct 2008 (right) in the one-way nesting WRF simulation driven with ECMWF_OA data.

the Boothbay area. This high-pressure band moved northward in WRF simulation driven by ECMWF_OA, but not with other input data (Fig. 10). The time-scale of the travelling high-pressure band was ~35 min, and it spatial scale was ~50 km. On the rear end of the high-pressure band, wave-like behavior of the MSLP (i.e. pressure oscillations) was evident with lines of constant phase oriented W-E (WSW-ENE). It is interesting to note that in WRF simulation driven by ERA-Interim, even stronger isolated wave-like pattern of sea-level pressure, which was due to the IGW activity aloft (not shown), were found some 100 km west of Boothbay. However, these pressure oscillations had lines of constant phase NW-SE and the entire system moved from SSW-NNE. Concerning that both buoy and satellite analysis suggested that pressure disturbance that caused the Boothbay meteotsunami moved from SSE (SE) to NNW (NW), we consider that the MSLP field in WRF simulations driven with ERA-Interim is less appropriate for the further analysis than WRF simulations driven with ECMWF_OA.

Thus, several aspects point to the fact that WRF simulations driven with ECMWF_OA data showed the best results. In short, WRF simulations driven with NARR data were inadequate with respect to the shape, position and intensity of the modeled cloud band as well as the low-level conditions (Grey sounding). WRF driven with ERA-Interim produced quite a successful simulation, but did not show any pressure oscillations in the vicinity of Boothbay in the time window of +-2h around 19 UTC 28 Oct 2008 and lacks convective activity over the ocean, which is of direct interest for atmospheric triggering of meteotsunamis. Furthermore, we note that results were not very sensitive to the choice of the one-way or two-way nesting strategy as far as synoptic or gross mesoscale environment is concerned. However, it is expected that for simulations of IGWs such as seen on radar imagery the choice of nesting strategy can make a significant difference if the wavelengths of these waves are smaller than approximately 10 horizontal grid points (also due to potential aliasing). Finally, the important difference between different model simulations was that only the WRF simulation driven with ECMWF_OA data simulated the small scale high-pressure band near Boothbay, which will be analyzed in more depth in the next sections.

4. Sensitivity to the simulation horizon

To assess the sensitivity of model results to the simulation time-horizon (similar to forecast horizon, i.e. horizon is a time period between the initialization of the simulation and the phenomenon simulated), 4 additional experiments were performed. The sensitivity to the time-horizon is important for potential

Table 2: List of experiments performed to assess the role of the simulation time-horizon.

EXP. NO.	1	2	7	8	9	10
Initial time	12 UTC 28 Oct 2008	12 UTC 28 Oct 2008	06 UTC 28 Oct 2008	06 UTC 28 Oct 2008	12 UTC 28 Oct 2008	12 UTC 28 Oct 2008
Nesting type	1-way	2-way	1-way	2-way	1-way	2-way

use of mesoscale models in prediction and warning systems related to meteotsunamis. Two simulations (1-way and 2-way) were initiated at 06 UTC 28 Oct 2008 and two at 00 UTC 28 Oct 2008 using ECMWF_OA reanalysis for ICs and LBCs.

It should be noted that these and subsequent time-series of the sensitivity experiments driven with ECMWF_OA at the locations of buoy observations differed in details, but did not show neither qualitative differences other than presented in Fig. 7 nor allowed for assessment of the "best" simulation in comparison with measurements. Therefore, time-series plots will not be shown hereafter.

Simulated radar reflectivity (Figs. 16, 17) and MSLP (Fig. 18) suggested that with increasing the time between the model initiation and the event, the accuracy of simulation rapidly diminished. Indeed, the simulation initiated just 6 hours prior to the control simulation (which was initiated at 12 UTC, so 9 hours prior to the meteotsunami event), showed quite different results regarding the presence of the high-pressure band moving over Boothbay. Furthermore, in all four simulations initiated at 00 UTC and 06 UTC 28 Oct 2008 radar reflectivity resembles the results from simulation started 12 hours later but show more discrepancies when compared with radar imagery, such as too weak convective activity in the vicinity of Boothbay area and offshore. More importantly, mean sea level pressure distribution in these four simulations was smooth and showed no clues of the pressure oscillations relevant for the onset of the Boothbay meteotsunami.

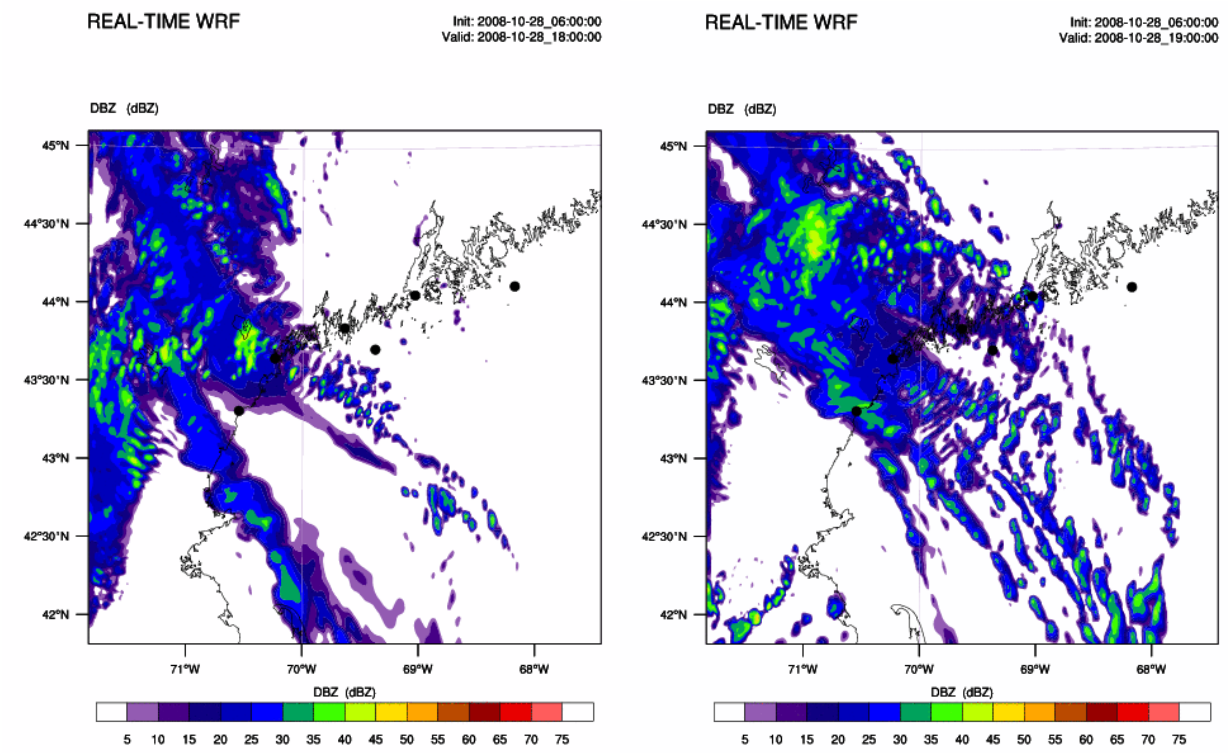

Figure 16: Simulated radar reflectivity at 18 UTC 28 Oct 2008 (left) and 19 UTC 28 Oct 2008 (right) in the simulation initiated at 06 UTC 28 Oct 2008 and driven with ECMWF_OA data.

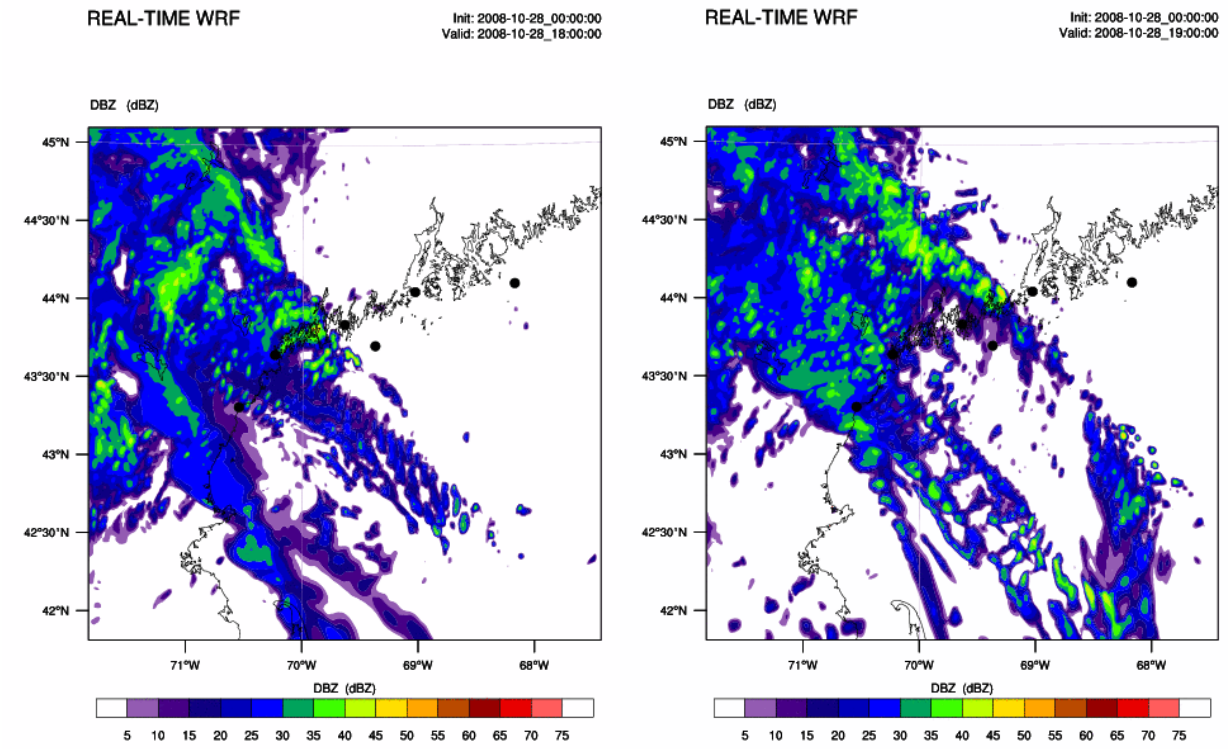

Figure 17: Simulated radar reflectivity at 18 UTC 28 Oct 2008 (left) and 19 UTC 28 Oct 2008 (right) in the simulation initiated at 00 UTC 28 Oct 2008 and driven with ECMWF_OA data.

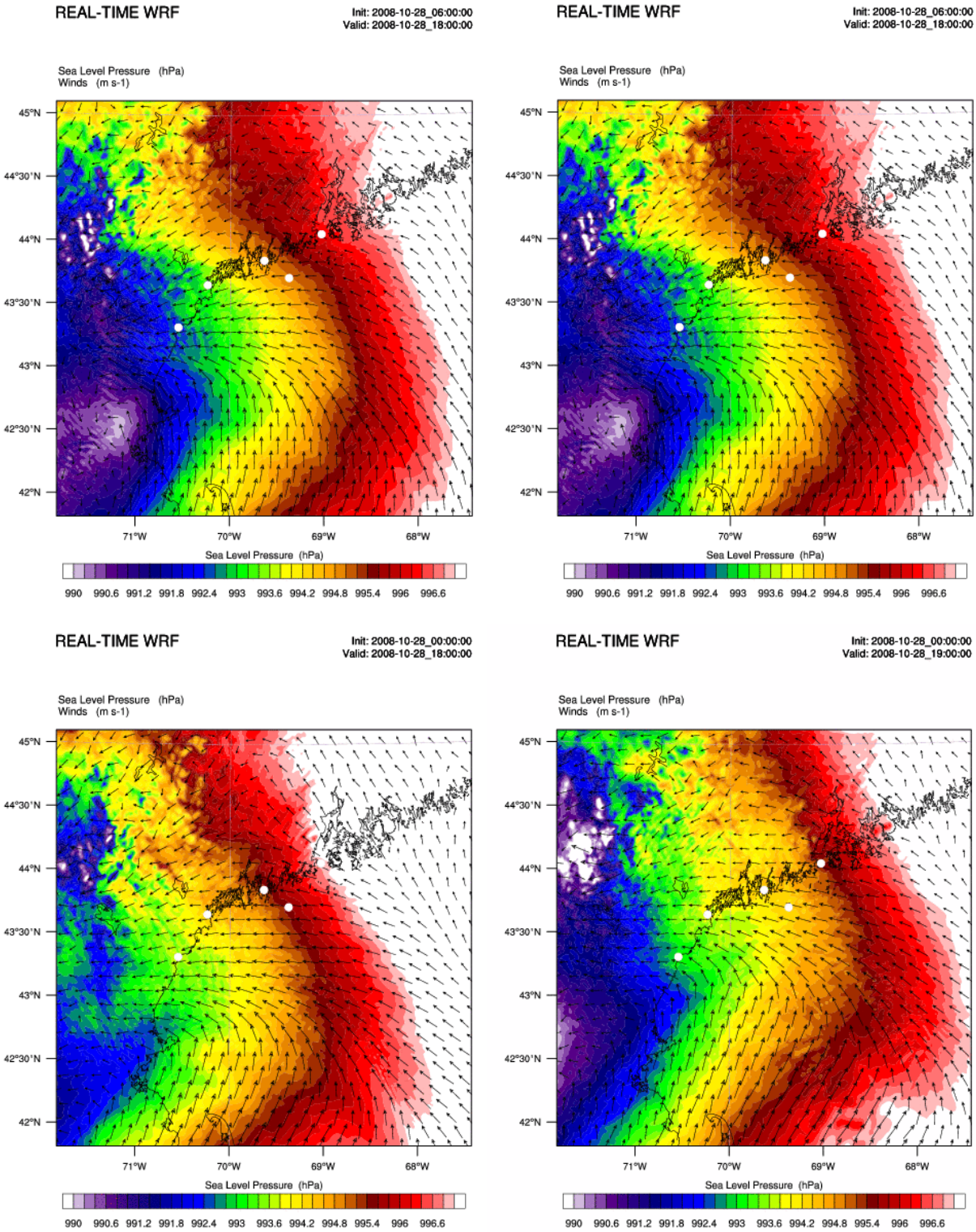

Figure 18: Simulated MSLP and 10 m wind vectors at 18 UTC 28 Oct 2008 (left) and 19 UTC 28 Oct 2008 (right) in the simulation initiated at 06 UTC (top) and 00 UTC (bottom) 28 Oct 2008 and driven with ECMWF_OA data.

5. Sensitivity to microphysics schemes

Microphysical schemes provide atmospheric heat and moisture tendencies and determine surface rainfall. Sensitivity to microphysics was performed by changing the default 2-moment 6-class Morrisson scheme to simpler 1-moment 5-class Lin (Purdue) scheme. Though more simple, Lin scheme is a research scheme often considered too computationally costly to be used in operational NWP. All simulations were performed with ECMWF_OA ICs and LBCs.

Table 3: List of experiments performed to assess the role of the microphysics schemes.

EXP. NO.	1	2	11	12
Microphysics type	Morrison	Morrison	Lin (Purdue)	Lin (Purdue)
Nesting type	1-way	2-way	1-way	2-way

The simulated radar reflectivity is shown in Fig. 19. Comparison of 1-way nesting at 19 UTC 28 Oct 2008 showed that WRF results with Lin scheme were similar to the results with the Morrison scheme. Lin scheme produced slightly stronger reflectivity especially in the southern part of the domain. However, comparison with radar data showed that in this area the control simulation with Morrison sheme provided excessive reflectivity. Thus, results of sensitivity simulation with the Lin scheme appeared slightly worse than results with the Morrison microphysics scheme. Comparison of 1-way and 2-way nesting strategy at both 18 UTC and 19 UTC 28 Oct 2008 showed slight differences in simulated radar reflectivity. These differences were perhaps more evident in the mean sea level pressure field (Fig. 20). While the pressure distribution was similar, differences are evident e.g. in structure of the high-pressure band moving over Boothbay (denoted by the ellipse on the figure), where individual troughs and ridges were organized differently, likely due to different organization of the convection or IGWs aloft. Thus, difference in the nesting strategy may influence the representation of the pressure disturbance and individual pressure oscillations associated with the Boothbay meteotsunami.

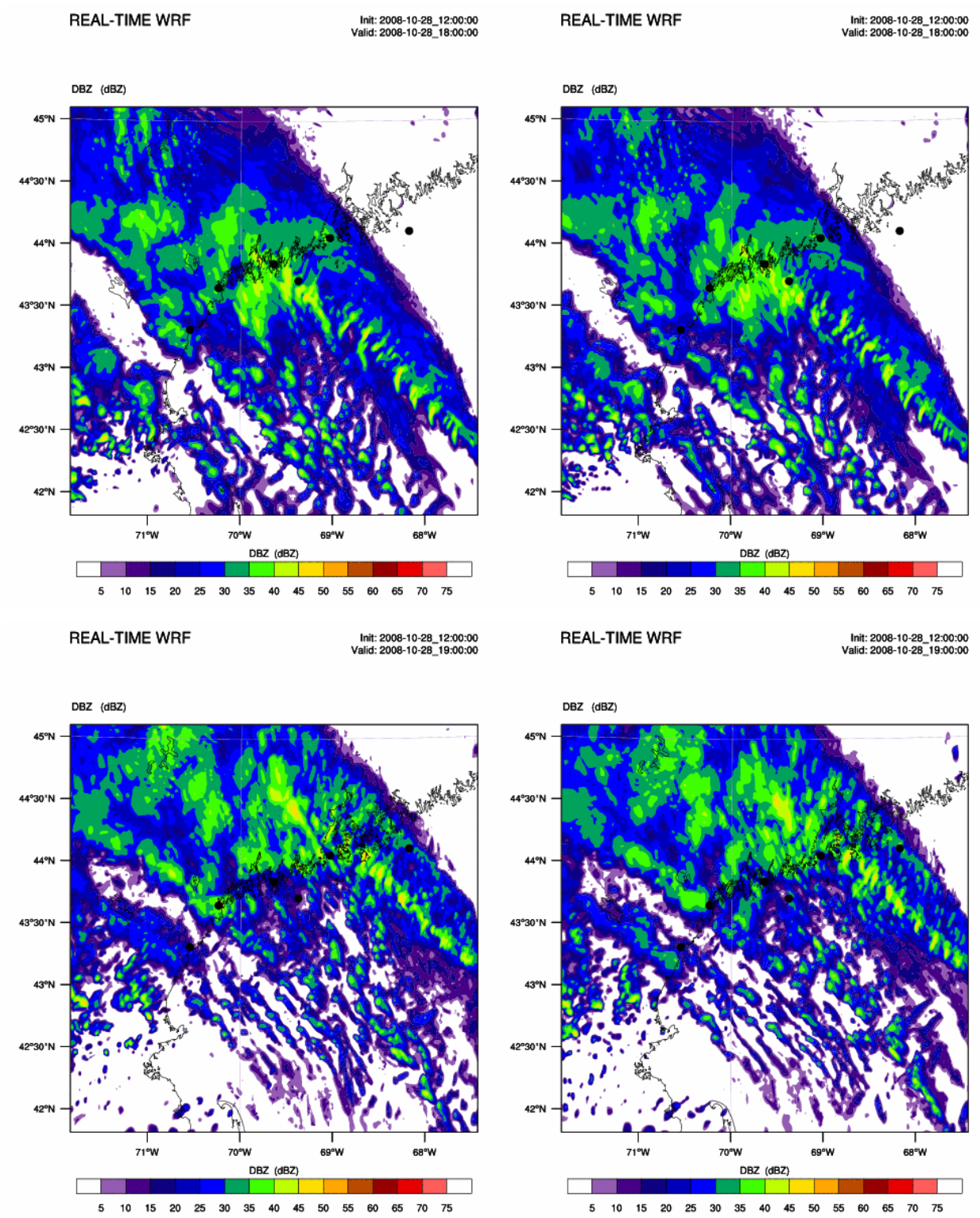

Figure 19: Simulated radar reflectivity at 18 UTC 28 Oct 2008 for 1-way (top left) and 2-way (top right) nesting strategy and at 19 UTC 28 Oct 2008 for 1-way (bottom left) and 2-way (bottom right) nesting strategy with Lin microphysics scheme. The lower left panel is to be compared with Fig. 12 (bottom left).

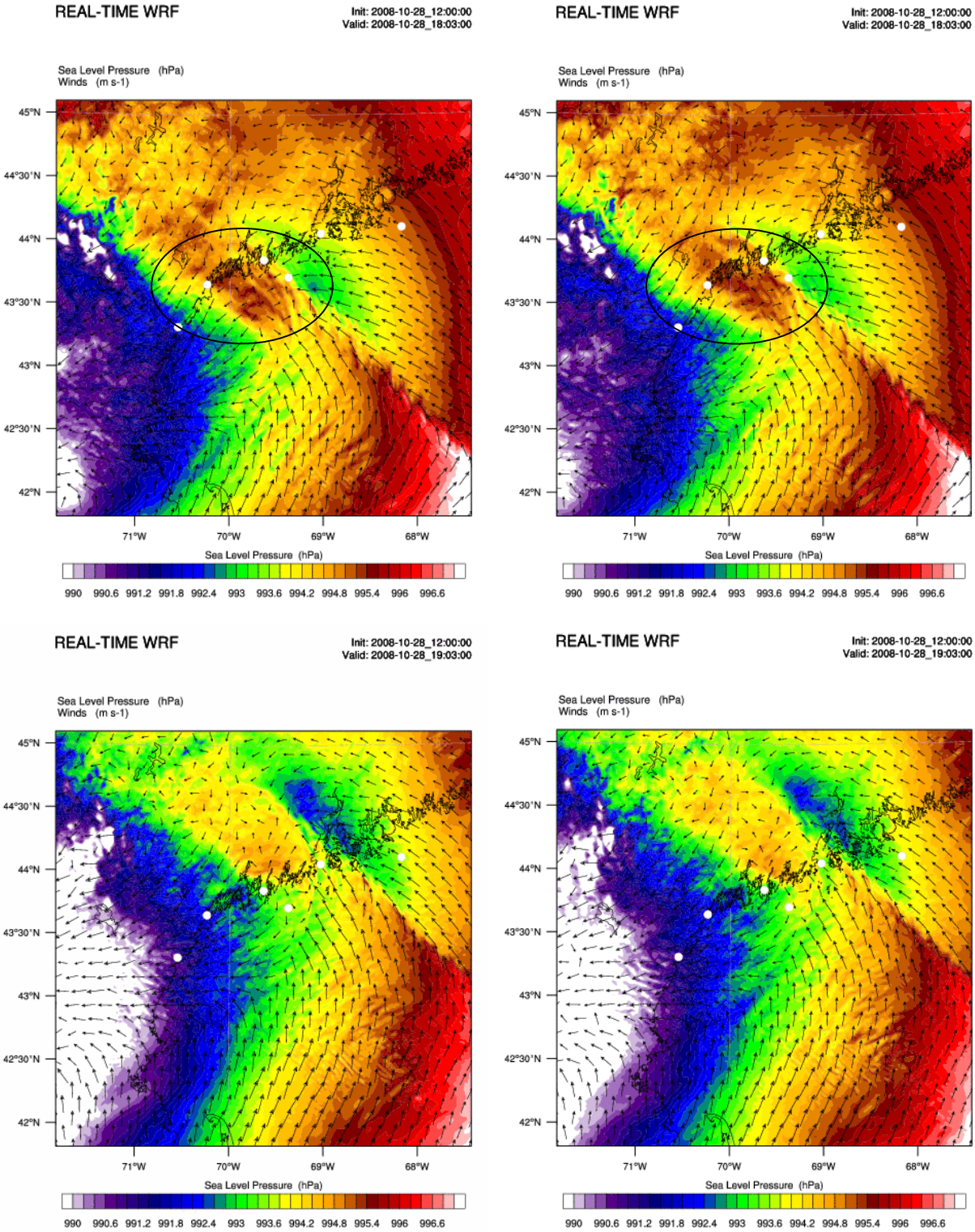

Figure 20: Simulated MSLP and 10 m wind vectors at 18 UTC for 1-way (top left) and 2-way (top right) nesting strategy and at 19 UTC 28 Oct 2008 for 1-way (bottom left) and 2-way (bottom right) nesting strategy with Lin microphysics scheme. Two plots on the left are to be compared with Figs. 14 and 15. Ellipses denote areas where different organization of individual pressure oscillations is evident.

6. Sensitivity to convection schemes

Additional numerical experiments were performed to assess the sensivitiy of the mesoscale simulations to the choice of the convection scheme. Three different types of convection schemes were tested: Grell-Devenyi (GD) ensemble convection scheme, which was used in the control simulation, Betts-Miller-Janjic (BMJ) and Kain-Fritch (KF) convection schemes, all in 1-way and 2-way nesting setups (Table 4). Convection scheme was used only in the outermost domain (dx=9 km), and was withheld in intermediate domain (dx=3 km) and innermost domain (dx=1 km). This is a standard approach in mesoscale modeling studies, since the convective cells at grid spacings of 3 km and smaller start to be explicitly resolved.

Comparison of simulated (Figs. 21, 22, 23) and measured (Fig. 11) radar reflectivities suggests all the convection schemes simulated the overall shape of reflectivity distribution well with main convection band oriented southeast-northwest, and secondary convection area farther southwest of the precipitation band. However, a detailed look reveals some inaccuracies. For example, the areas of high reflectivity A, B and C (cf Fig. 11) were accurately represented in neither of the simulations. Furthermore, at 18 UTC 28 Oct 2008 all schemes produced too intense radar reflectivity offshore south of the observed precipitation system over the ocean (northeast of Provincetown that is area mid-way to Boothbay). This issue was somewhat reduced with the use of BMJ scheme. At 19 UTC, however, the shape of the area with convective activity seemed to be slightly less accurate in simulations with BMJ scheme than in other two simulations. In particular, while the radar images show that the width of the convective zone was wider towards the southeast, BMJ simulated convective band narrowed towards the southeast. Furthermore, neither of the simulations represented well the area without convective activity north of Provincetown. This was also the case with narrow reflectivity bands on the southeast edge of the precipitation system.

Table 4: List of experiments performed to assess the role of the convection schemes.

EXP. NO.	1	2	13	14	15	16
Convection scheme	Grell-Devenyi	Grell-Devenyi	Betts-Miller-Janjic	Betts-Miller-Janjic	Kain-Fritch	Kain-Fritch
Nesting type	1-way	2-way	1-way	2-way	1-way	2-way

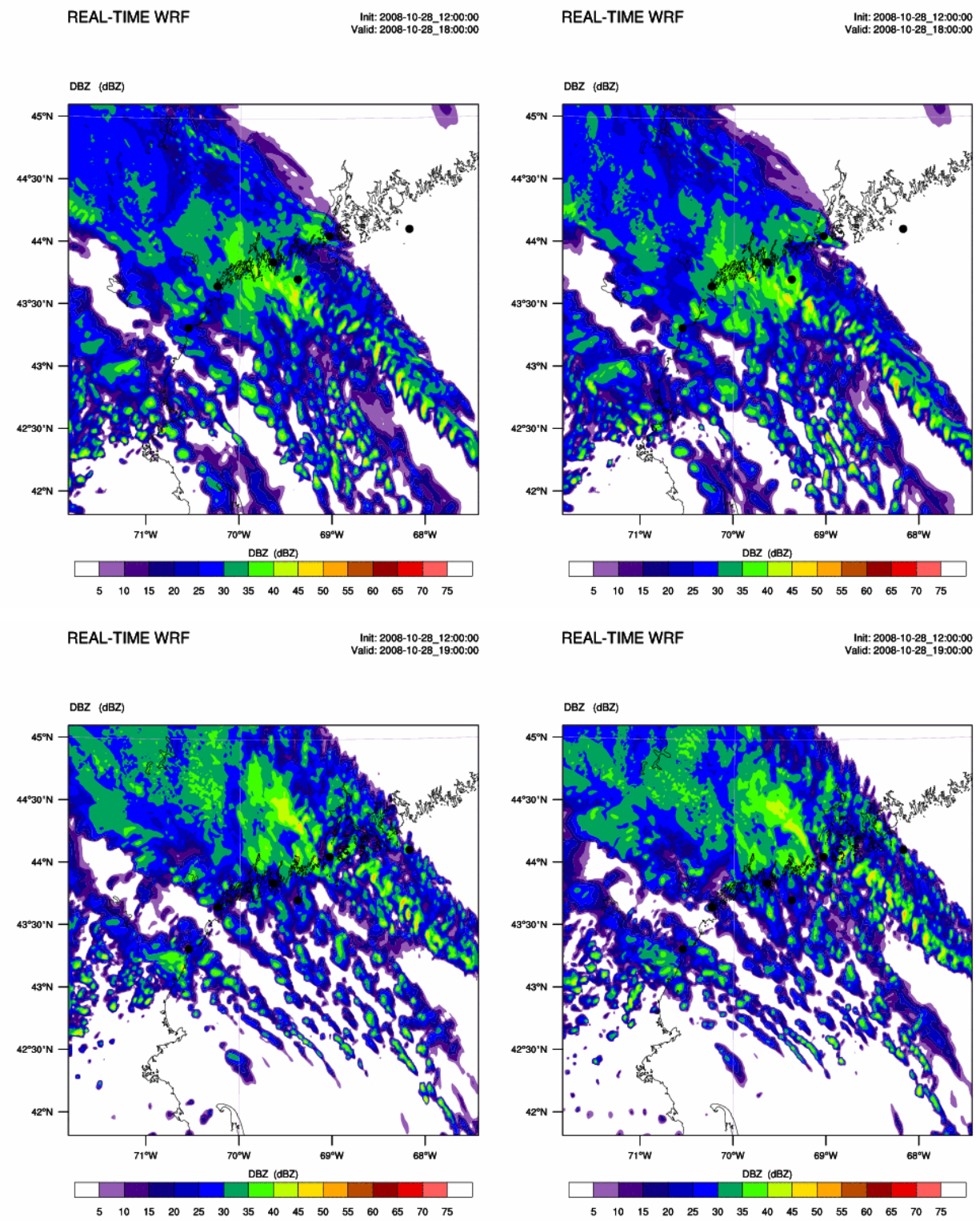

Figure 21: Simulated radar reflectivity for WRF simulation with Grell-Devenyi convection scheme and 1-way (left) and 2-way (right) nesting strategies at 18 UTC (top) and 19 UTC (bottom) 28 Oct 2008.

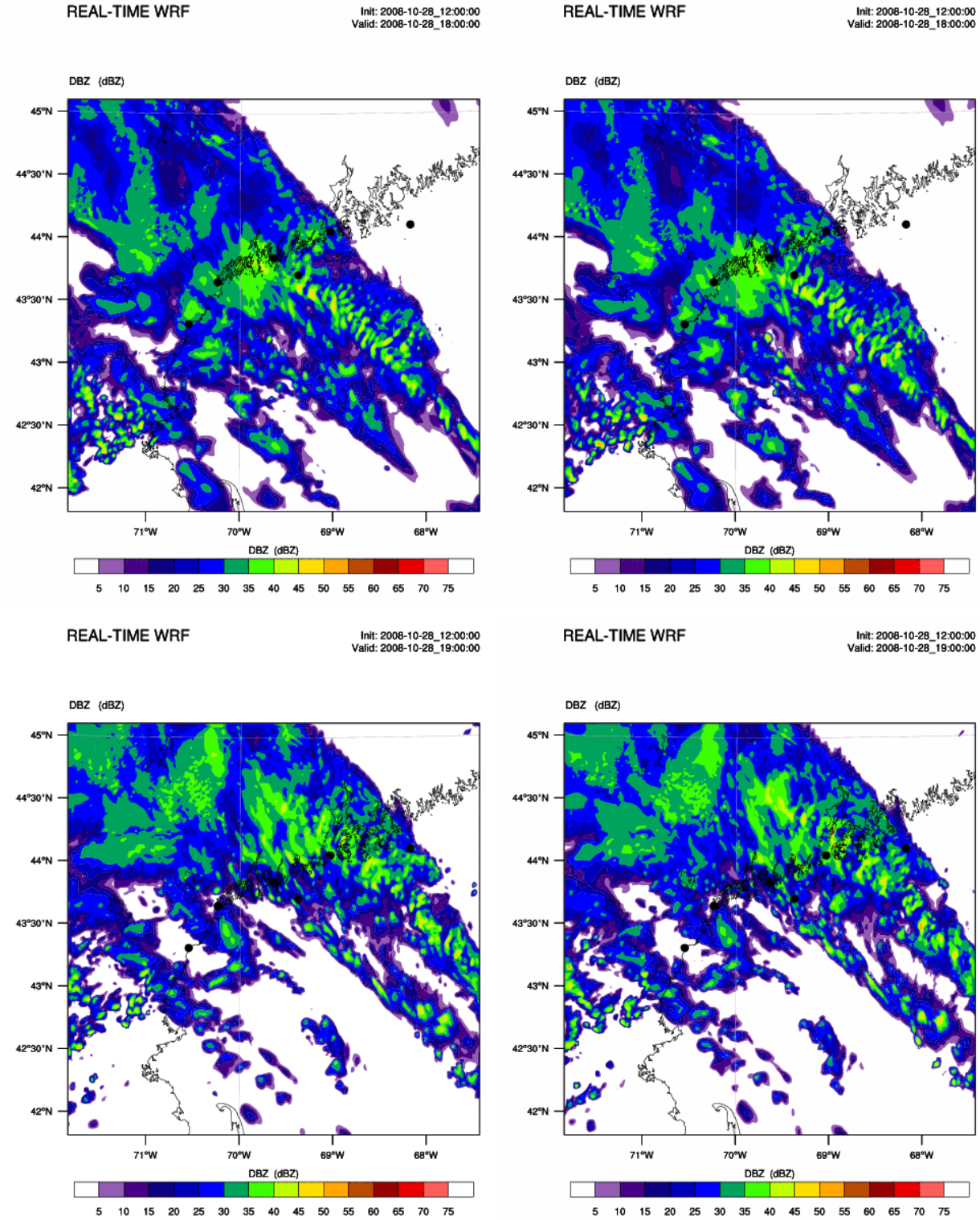

Figure 22: Simulated radar reflectivity for WRF simulation with Betts-Miller-Janjic convection scheme and 1-way (left) and 2-way (right) nesting strategies at 18 UTC (top) and 19 UTC (bottom) 28 Oct 2008.

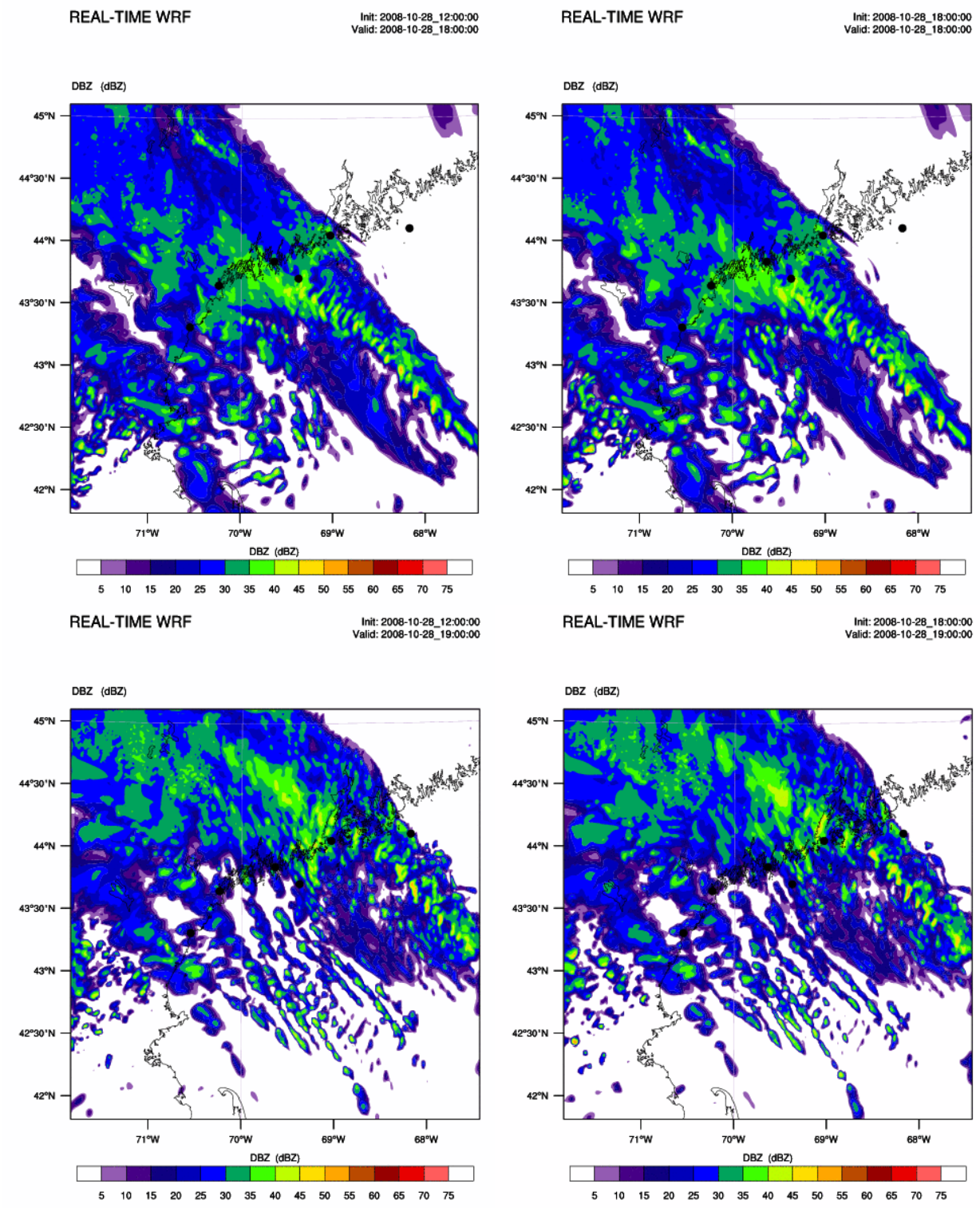

Figure 23: Simulated radar reflectivity for WRF simulation with Kain-Fritch convection scheme and 1-way (left) and 2-way (right) nesting strategy at 18 UTC (top) and 19 UTC (bottom) 28 Oct 2008.

Thus, around 19 UTC the rear side of the precipitation system was simulated with the limited accuracy. In contrast to 18 UTC, the least accurate results were found with BMJ simulation (in contrast to 18 UTC). However, it was the rear side of the precipitation system that was over Boothbay at the time of meteotsunami. Therefore, though all simulations were of quite similar results, Kain-Fritch simulation appears to be the most appropriate for further analysis. Finally, the role of nesting strategy influenced the details of the precipitation system, but its gross features were similar regardless of the choice. Concerning the very localized nature of meteotsunamis, as we mentioned above, the choice of the nesting strategy may make a difference for simulating details of very phenomenon, as we will see later.

Main features of the mean sea level pressure distributions at 18 UTC and 19 UTC 28 Oct 2008 were similar in all six simulations (Figs. 24, 25, 26). However, the details of the high-pressure band distribution (within ellipse on top left panel of Fig. 24) crossing Boothbay differed in both structure and intensity among all four simulations, thus with respect to both convection scheme and the type of nesting strategy. This was especially evident for wave-like pressure oscillations near the rear end of the precipitation system and close to Boothbay. Namely, near the rear end of the high-pressure band, simulations with GD convective scheme showed the least intensive wave-like pattern, followed by BMJ simulations, while simulations with KF scheme showed the strongest mean sea level pressure oscillations.

In summary, gross features of mesoscale simulations of the precipitation system (radar reflectivity) and MSLP were similar regardless of the tested convection schemes. However, the details in the precipitation system and pressure oscillations within the high-pressure band did differ and WRF simulations with Kain-Fritch convection scheme appear somewhat more appropriate for further analysis of atmospheric conditions related to the Boothbay event. Thus, the choice of the convection scheme may play an important role in simulating or predicting the details of atmospheric conditions during meteotsunami events.

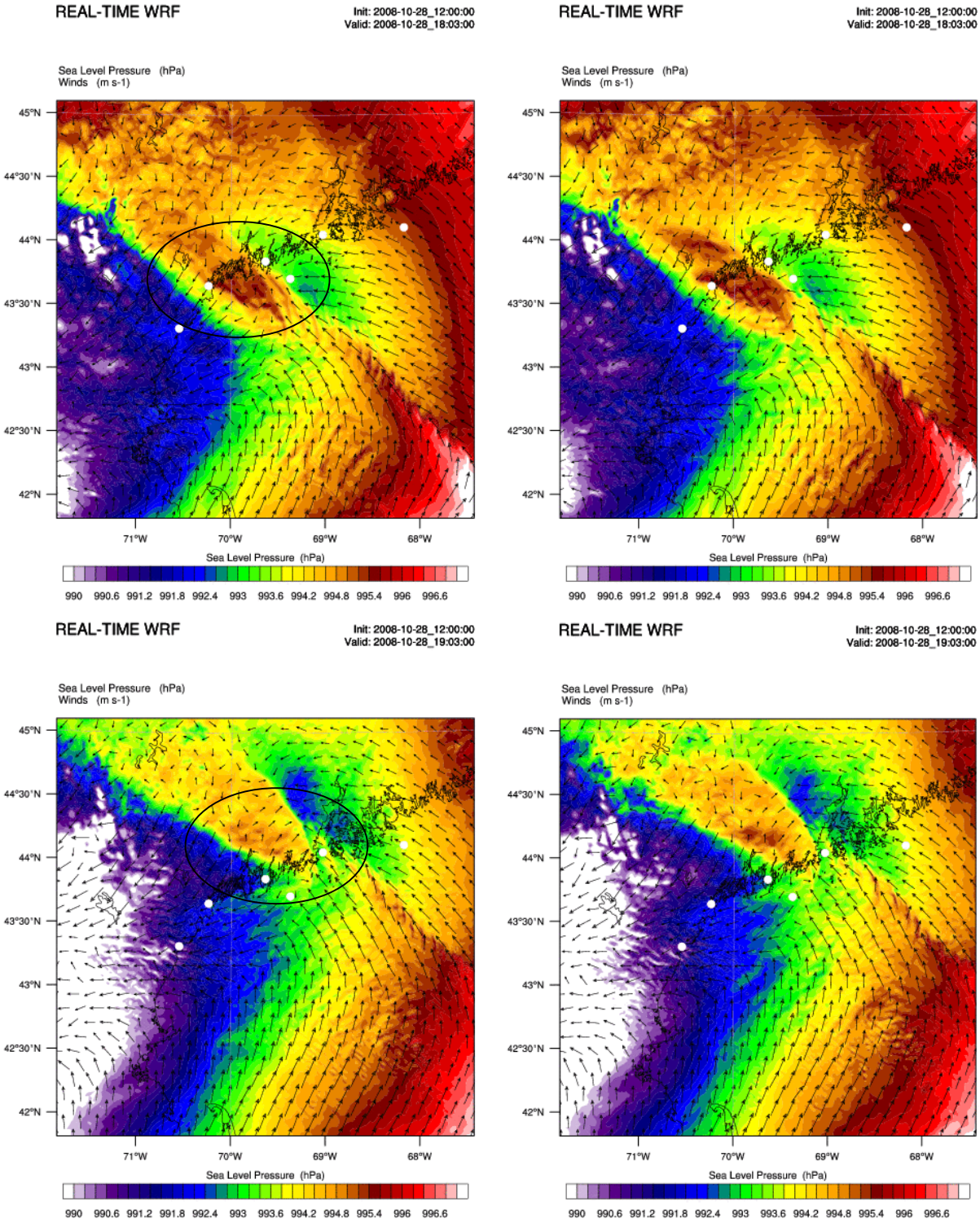

Figure 24: Simulated MSLP and 10m wind vectors for Grell-Devenyi convection scheme and 1-way (left) and 2-way (right) nesting strategy at 18 UTC (top) and 19 UTC (bottom) 28 Oct 2008.

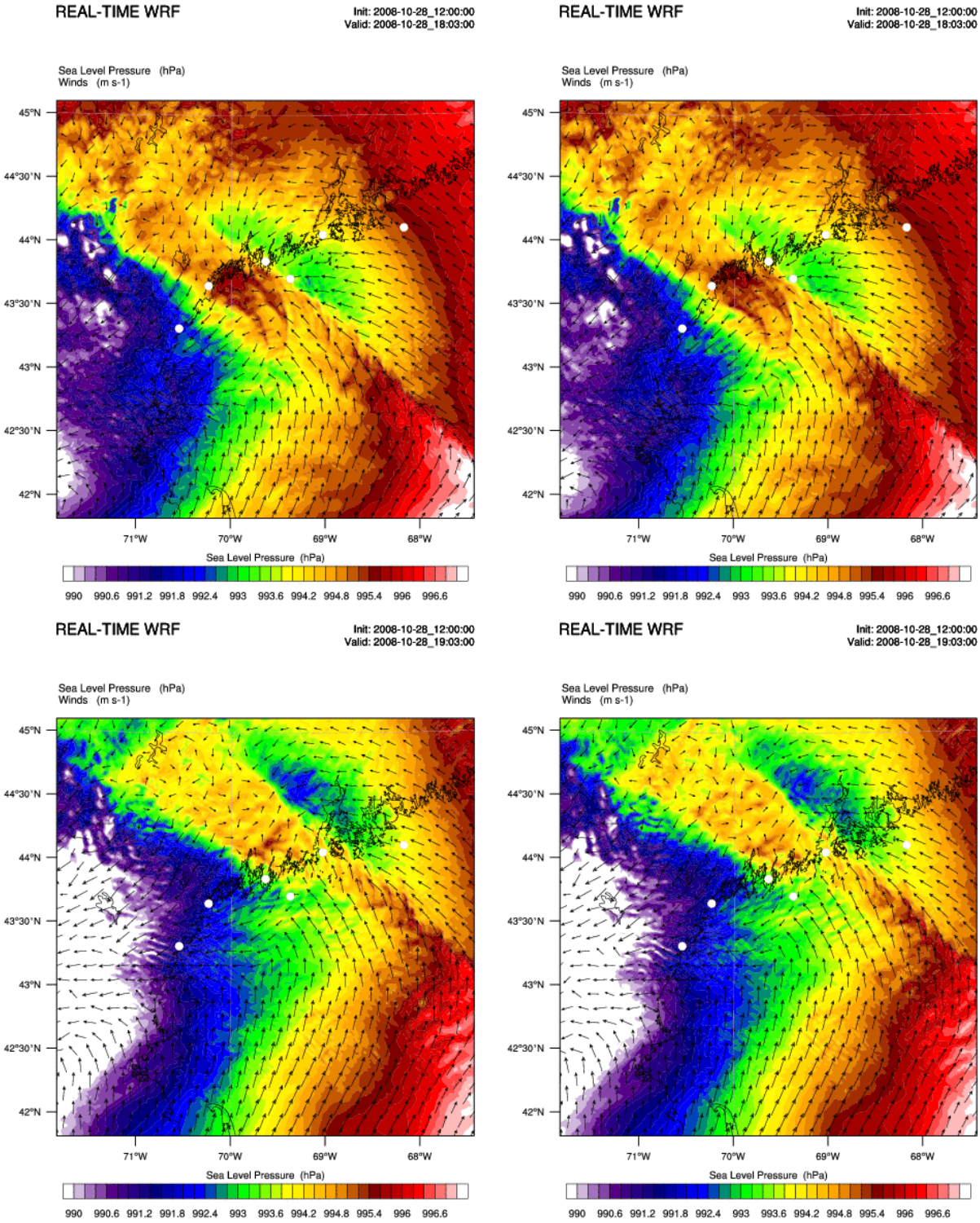

Figure 25: Simulated MSLP and 10m wind vectors for Betts-Miller-Janjic convection scheme and 1-way (left) and 2-way (right) nesting strategy at 18 UTC (top) and 19 UTC (bottom) 28 Oct 2008.

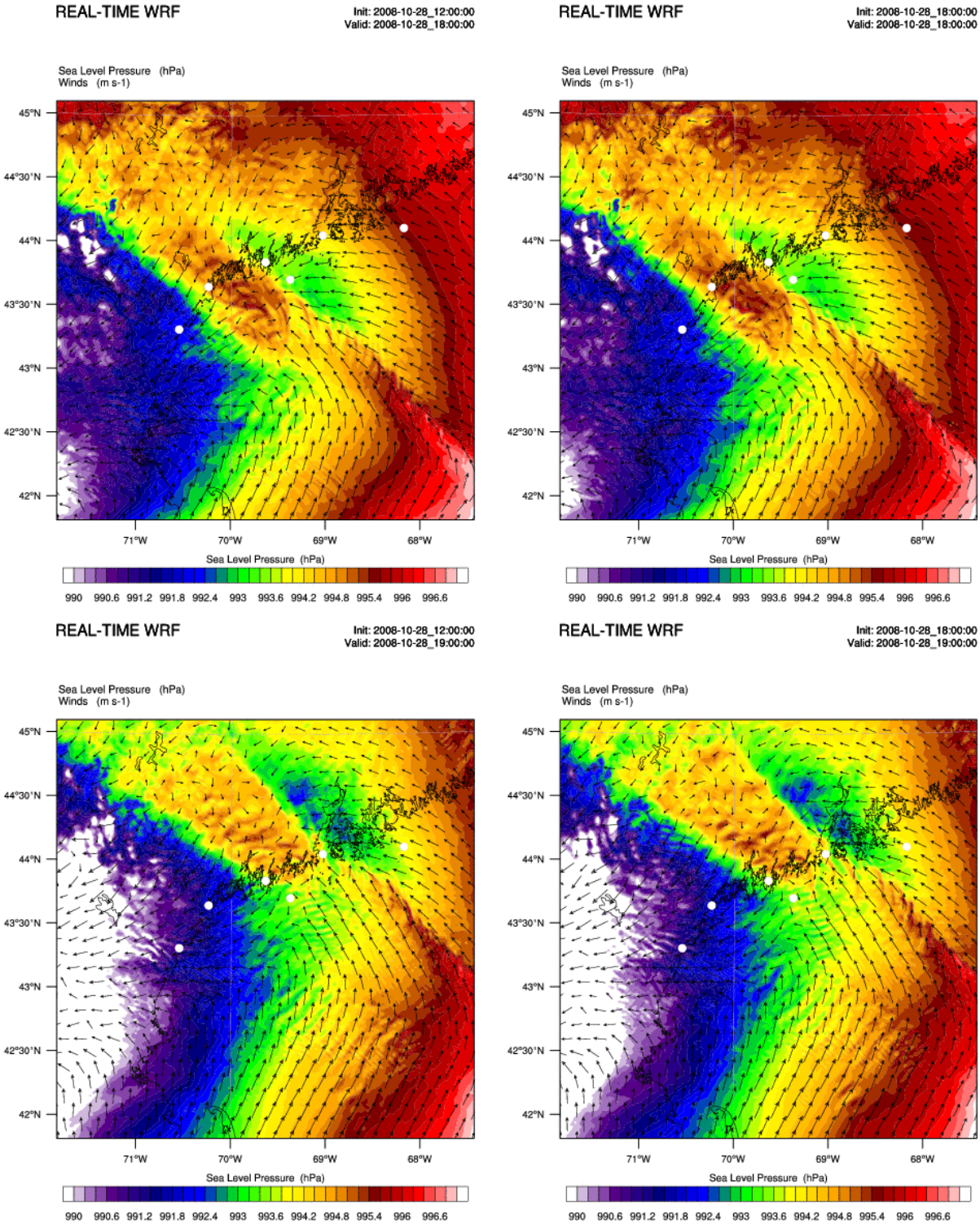

Figure 26: Simulated MSLP and 10m wind vectors for Betts-Miller-Janjic convection scheme and 1-way (left) and 2-way (right) nesting strategy at 18 UTC (top) and 19 UTC (bottom) 28 Oct 2008.

7. Additional analysis and discussion

As mentioned earlier, a centre of the deep cyclone was located just southeast of the Boothbay area. At the approximate time of the Boothbay event (19 UTC 28 Oct 2008), relatively small-scale elongated high-pressure band crossed the Boothbay area moving northward in WRF simulations driven by ECMWF_OA, but not with other input data (cf. Fig. 10). Here we analyze the properties of the surface pressure distribution in more detail, including pressure gradients and tendencies. Concerning the somewhat better performance of the Kain-Fritch convection scheme regarding the simulation of the observed radar reflectivity we proceed with the analysis of simulations EXP 15 and EXP 16 (Table 5.). Concerning the potential application of mesoscale models in the warning system, both 1-way and 2-way nesting simulations are analyzed to assess the robustness of the WRF model results and give clues about the predictability of the meteotsunami-related atmospheric conditions.

Table 5. The setup of WRF simulations used for additional analysis.

EXP. NO.	Convection scheme	Nesting type	ICs and LBCs	Microphysics scheme
15	Kain-Fritch	1-way	ECMWF_OA	Morrison 2-moment
16	Kain-Fritch	2-way	ECMWF_OA	Morrison 2-moment

7.1 The surface pressure conditions

Mean sea level pressure and 10 m wind vectors in the vicinity of Boothbay showed that the high-pressure band was associated with the passage of the squall line (Figs. 27, 28). The time-scale of the pressure disturbance when it reached Boothbay was ~35 min, and its spatial scale was ~50 km. This passage of the squall line (and pressure disturbance) was associated with precipitation, which was also simulated in the model (not shown). The front end of the disturbance reached Boothbay around 18 UTC according to the model simulations (Fig. 27). The "pressure jump" associated with the passage of the mesohigh at 18 UTC was ~2 hPa, and was similar in the both simulations.

At 18:30 at the rear end of the disturbance, a well defined wave-like pressure distribution (wave-train of pressure oscillations) was evident with lines of constant phase oriented WSW-ENE, and traveling from SSE to NNW (Fig. 28). This pressure oscillations were some extent found in radar imagery as

well (cf. Fig. 11) and suggested the IGW activity aloft. It is interesting to note that this type of wave-like structure was not that evident in radar imagery. This suggests that that IGWs and convection were not uniquely coupled and that wave-CISK might not be the dominant mechanism of the IGWs maintenance. The pressure differences between the ridges and troughs in the pressure distribution reached several hPa over several kilometers in both simulations (quantitative analysis will be presented below). At this time, these pressure differences were found in the Boothbay area, especially just west of Boothbay, both over the land and over the ocean. This wave-like pattern of pressure distribution was found at 19 UTC as well. At that time, the individual ridges and troughs in the pressure distribution moved northward and were more intense over the land, and less intense over the ocean. After the main part of the wave-train moved over Boothbay, small amplitude wave-like pressure pattern extended far offshore.

A more detailed analysis shows mean sea level pressure and 10 m wind vectors every 6 minutes during time when the pressure jump reached Boothbay for 1-way (Fig. 29) and 2-way nesting (Fig. 30). The propagation speed of the pressure jump perpendicular to the main axis of the system is approximately ~20-22 m/s (from 17:54 to 18:06 the pressure jump traveled approximately ~15 km). Pressure jump of ~2 hPa, which was traveling towards the north, was sustained over the analyzed period of time (and later on).

On the rear side of the precipitation system, amplitudes of the pressure oscillations at 18 UTC reached approximately 2 hPa in 1-way nesting simulations and close to 3.0 hPa in 2-way nesting simulations. These amplitudes were as intensive and as localized such as the pressure oscillations found at 18:30 UTC (cf. Fig. 28) and later on, but did not fully resemble well-defined series of pressure oscillations (wave-train) in the pressure field found later on.

The magnitude of the pressure gradient near the pressure jump is shown in Figs. 31 and 32. In both 1-way nesting and 2-way nesting simulations, the magnitude of the pressure gradient associated with the pressure jump consistently reached close to 0.3 hPa/km in the very vicinity of Boothbay and up to 0.8 hPa/km at locations along the pressure jump. Near the rear edge of the precipitation system, farther to the south, the magnitude of the pressure gradient reached around 0.5 hPa/km in the 1-way nesting simulation and close to 0.8 hPa/km in the 2-way nesting simulation. These pressure gradients near the rear edge of the high-pressure band corresponded to large pressure oscillations (with amplitudes reaching 3 hPa) mentioned earlier (cf. Fig. 30) which will approach Boothbay within the next hour.

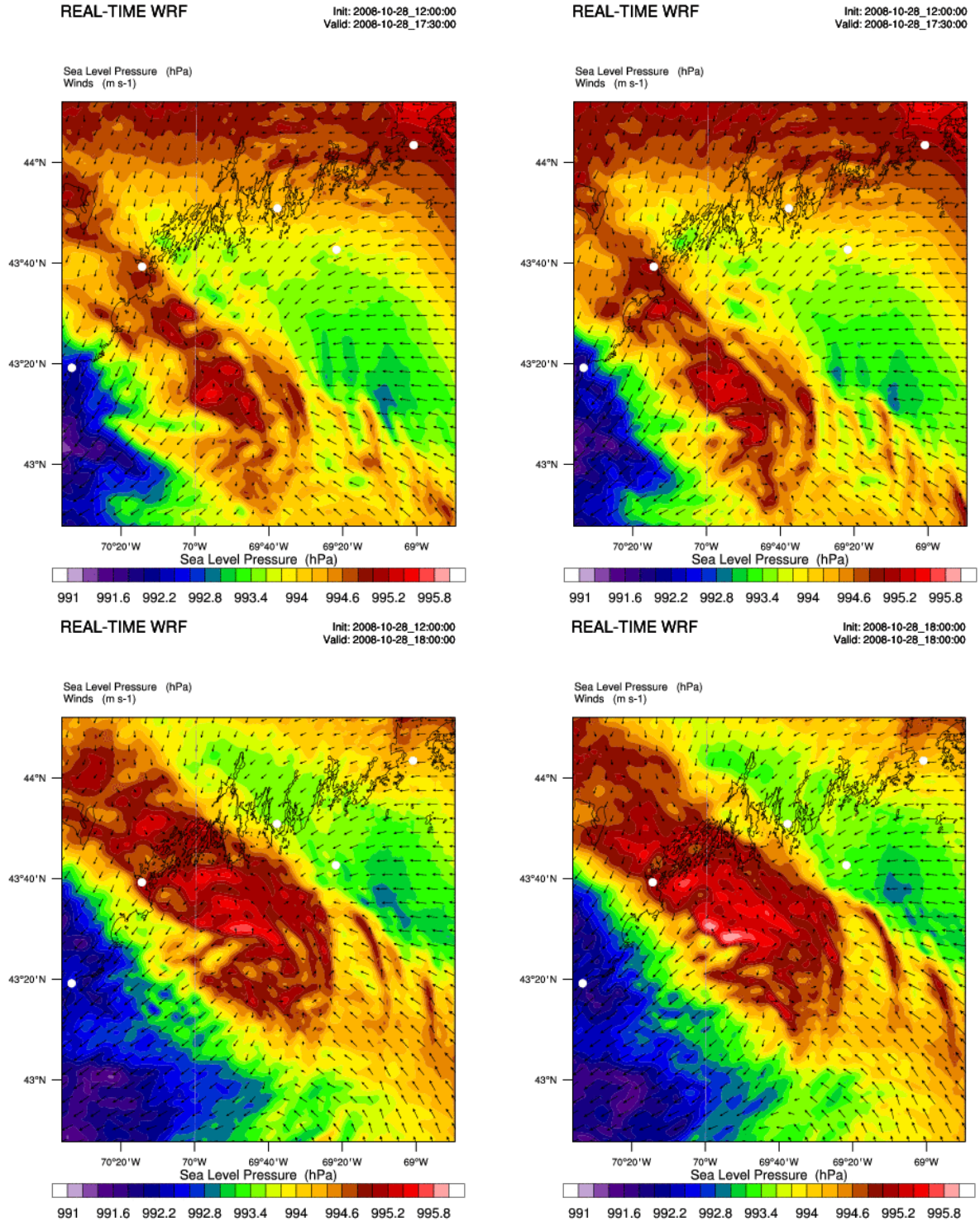

Figure 27: Simulated MSLP and 10m wind vectors on 17:30 UTC (top) and 18:00 UTC (bottom) 28 Oct 2008 for simulations with KF convection scheme and 1-way (left) and 2-way (right) nesting strategy. White dots (west-east) denote Wells, Portland, Boothbay, and locations of 44032 and 44033 buoys.

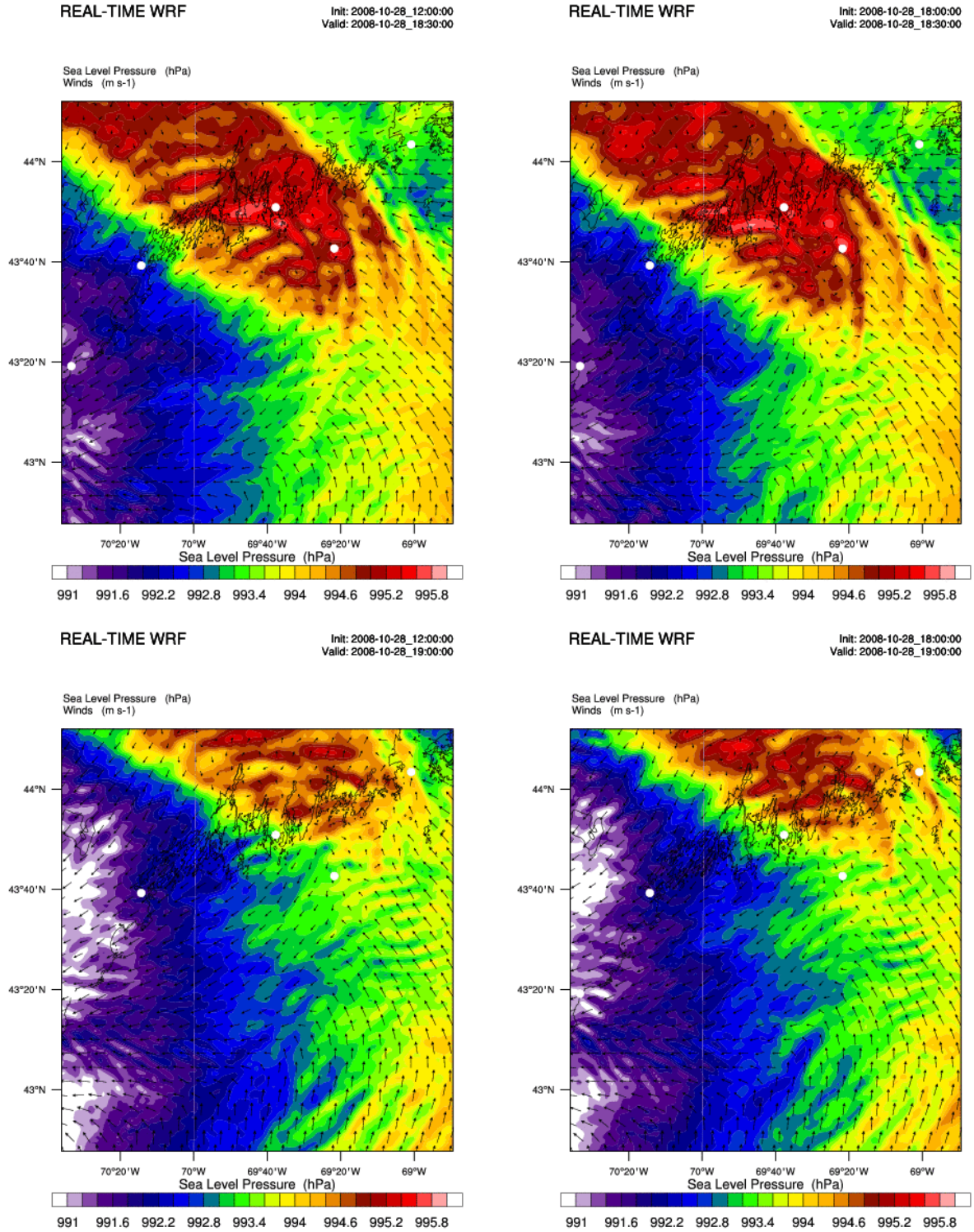

Figure 28: Simulated MSLP and 10m wind vectors at 18:30 UTC (top) and 19:00 UTC (bottom) 28 Oct 2008 for simulations with KF convection scheme and 1-way (left) and 2-way (right) nesting strategy. White dots (west-east) denote Wells, Portland, Boothbay, and locations of 44032 and 44033 buoys.

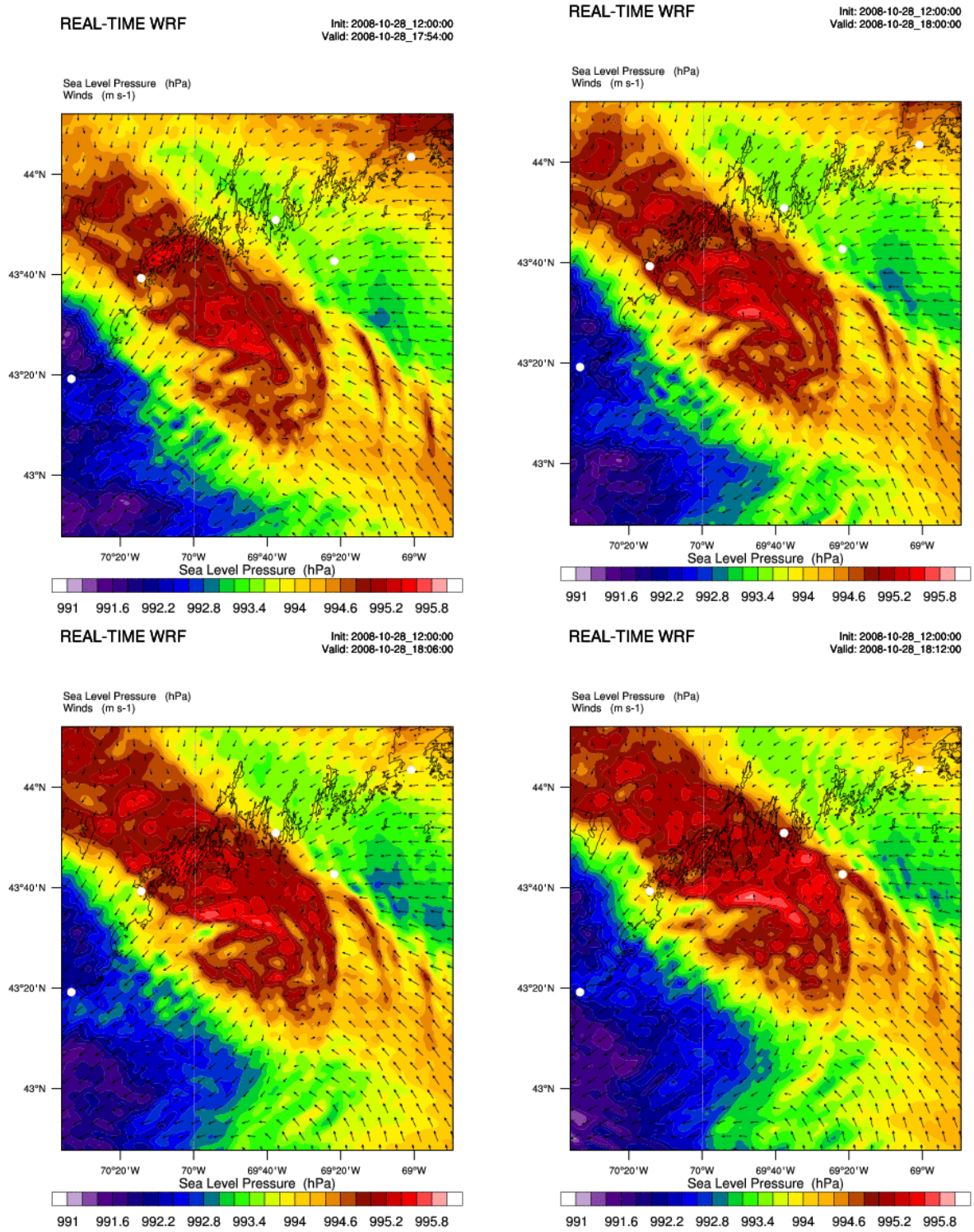

Figure 29: Simulated MSLP and 10m wind vectors on 17:54 UTC (top left), 18:00 UTC (top right), 18:06 UTC (bottom left) and 18:12 UTC (bottom right) 28 Oct 2008 for simulations with Kain-Fritch convection scheme and 1-way nesting strategy. White dots (west-east) denote Wells, Portland, Boothbay, and locations of 44032 and 44033 buoys.

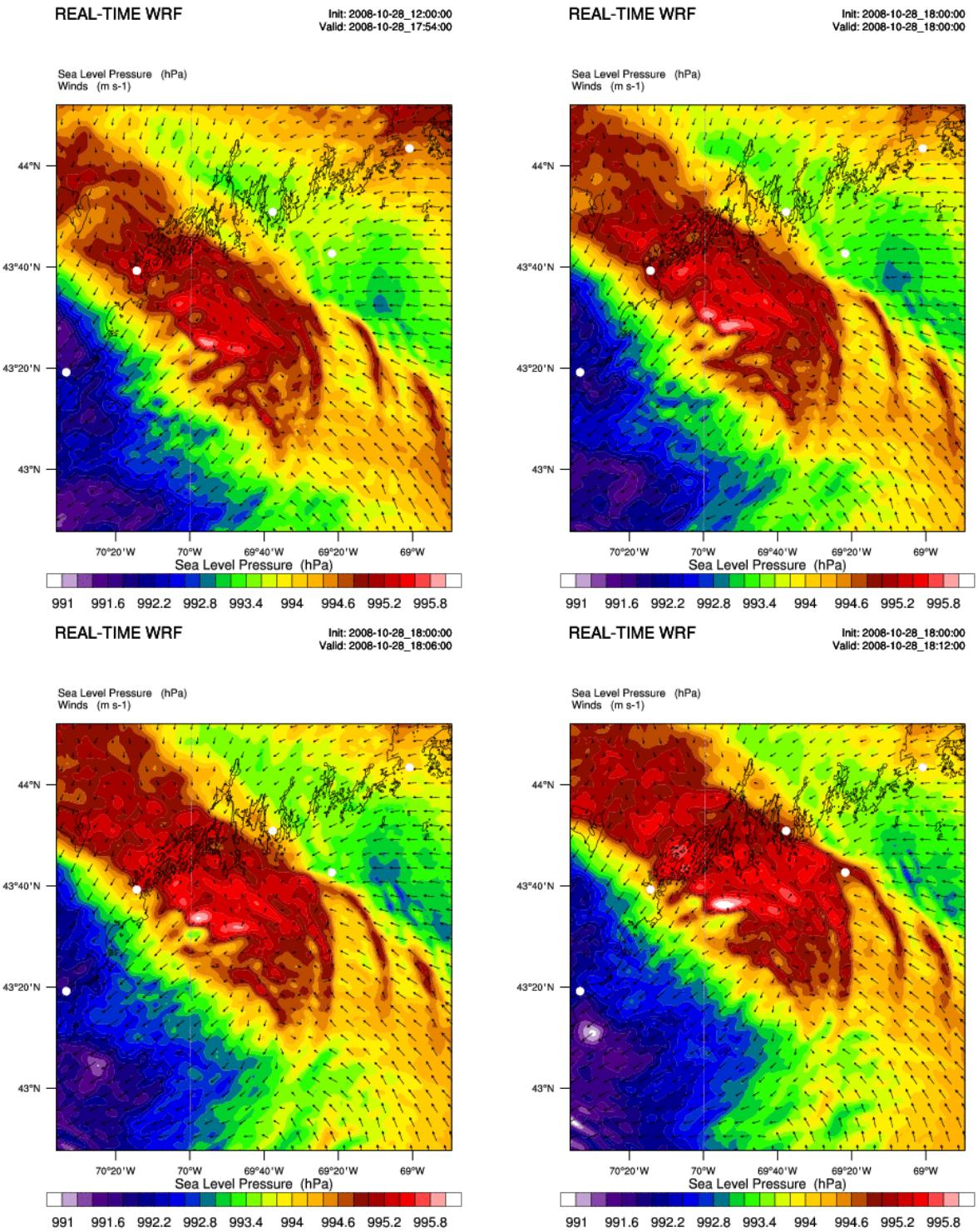

Figure 30: Simulated MSLP and 10m wind vectors on 17:54 UTC (top left), 18:00 UTC (top right), 18:06 UTC (bottom left) and 18:12 UTC (bottom right) 28 Oct 2008 for simulations with Kain-Fritch convection scheme and 2-way nesting strategy. White dots (west-east) denote Wells, Portland, Boothbay, and locations of 44032 and 44033 buoys.

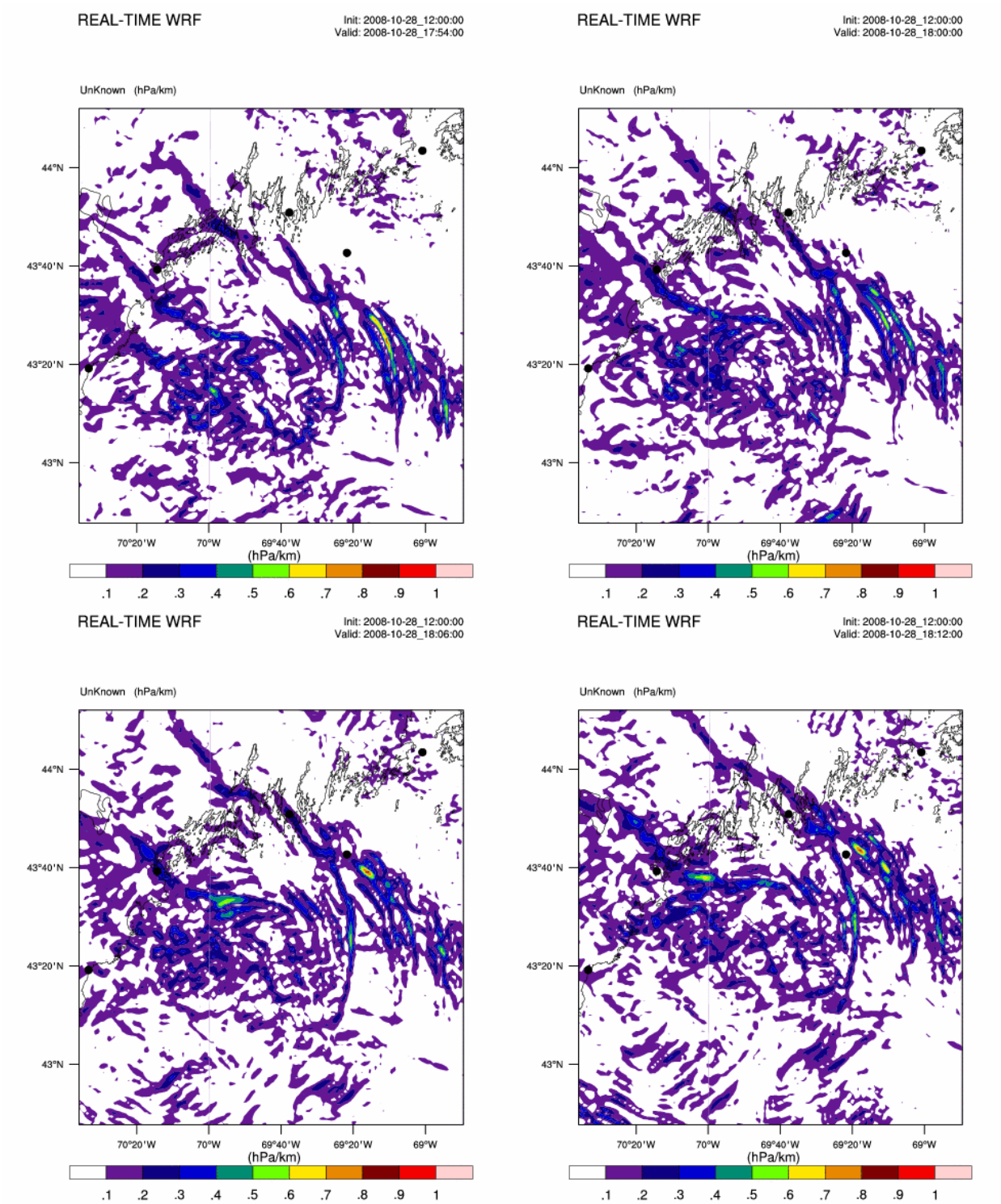

Figure 31: Simulated MSLP gradient (hPa/km) on 17:54 UTC (top left), 18:00 UTC (top right), 18:06 UTC (bottom left) and 18:12 UTC (bottom right) 28 Oct 2008 for simulations with Kain-Fritch convection scheme and 1-way nesting strategy. White dots (west-east) denote Wells, Portland, Boothbay, and locations of 44032 and 44033 buoys.

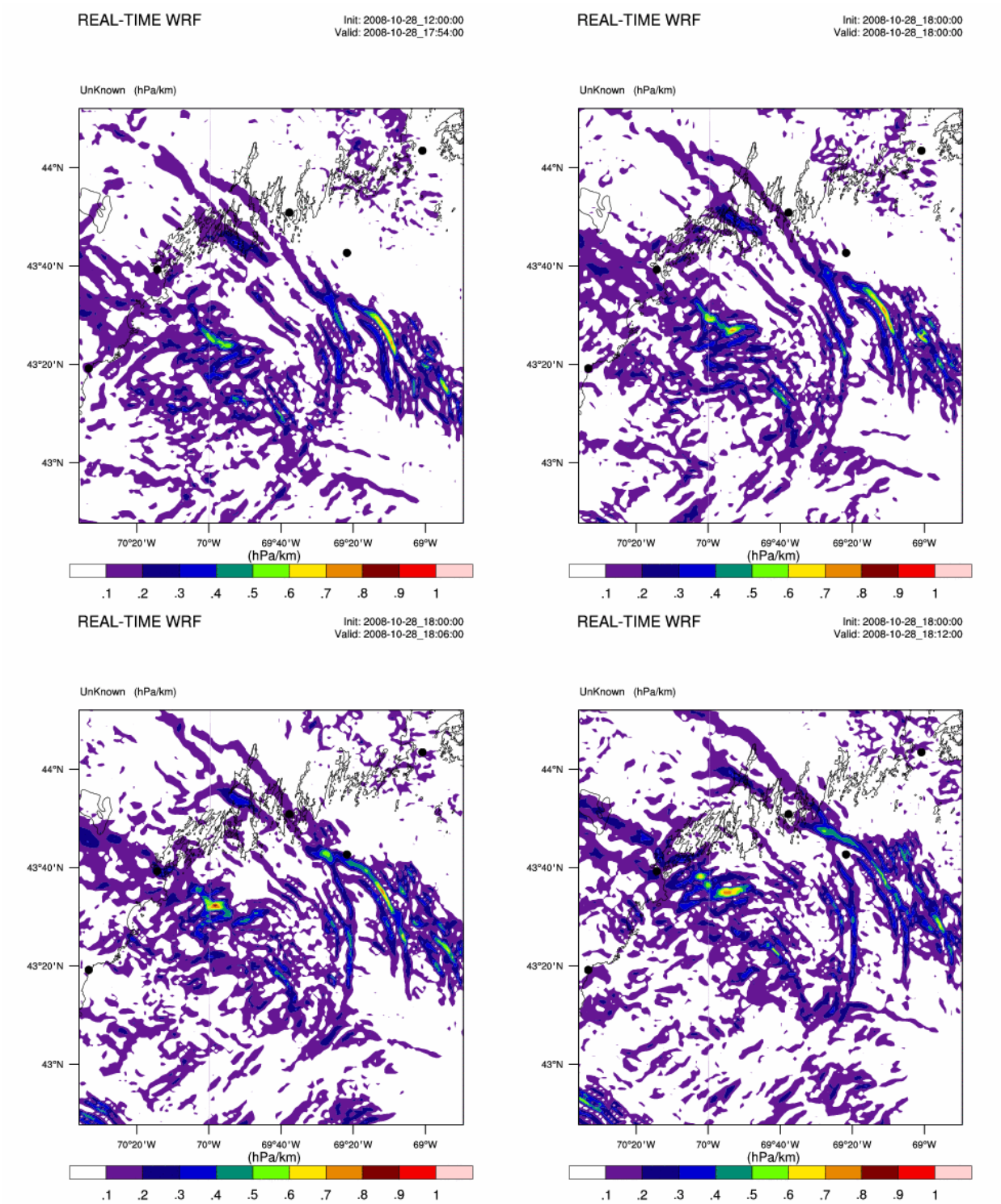

Figure 32: Simulated MSLP gradient (hPa/km) on 17:54 UTC (top left), 18:00 UTC (top right), 18:06 UTC (bottom left) and 18:12 UTC (bottom right) 28 Oct 2008 for simulations with Kain-Fritch convection scheme and 2-way nesting strategy. White dots (west-east) denote Wells, Portland, Boothbay, and locations of 44032 and 44033 buoys.

Pressure tendencies are further studied since the change if pressure with time is the main driving source of meteotsunamis. Pressure tendency is calculated as:

Pressure tendency (t) = MSLP(t)-MSLP(t-3min)

The pressure tendency values are representative of the pressure tendencies in 3 minutes, which was the output data frequency for 3-dimensional fields (only point values at several buoy locations shown earlier are saved with 6-second time step). Thus, these values are not representative neither for instantaneous pressure tendencies, nor maximal pressure tendencies. These values are also not representative to the absolute pressure drop that occurred in the area, which may had been larger than values presented here.

Pressure tendencies revealed a similar pattern of the most intensive amplitudes (Figs. 33. and 34.). The 3-min pressure tendency values associated with the pressure jump on the front edge of the precipitation system reached 1.5 hPa/3min near Boothbay and over 2.0 hPa/3min along the pressure jump somewhat southeast in both 1-way and 2-way nesting simulations. These pressure tendencies were quite consistent with time, as the pressure jump area approached Boothbay. Near the rear end of the precipitation system, pressure tendencies reached close to +1.2 hPa/3 min and -2.0 hPa/3 min in 1-way simulation and +1.2 hPa and -2.5 hPa/3 min in 2-way simulation. The areas associated with these extreme values were oriented WSW-ENE and moved towards NNW, forming a wave-train (a series o ridges and troughs) in pressure distribution. These pressure oscillations were consistent in time for almost an hour, similar to pressure tendencies associated with the pressure jump near the front edge of the precipitation system. It will be studied later on whether this wave-train in pressure distribution maintained its structure and intensity further towards the time of Boothbay meteotsunami that is when approaching the Boothbay area.

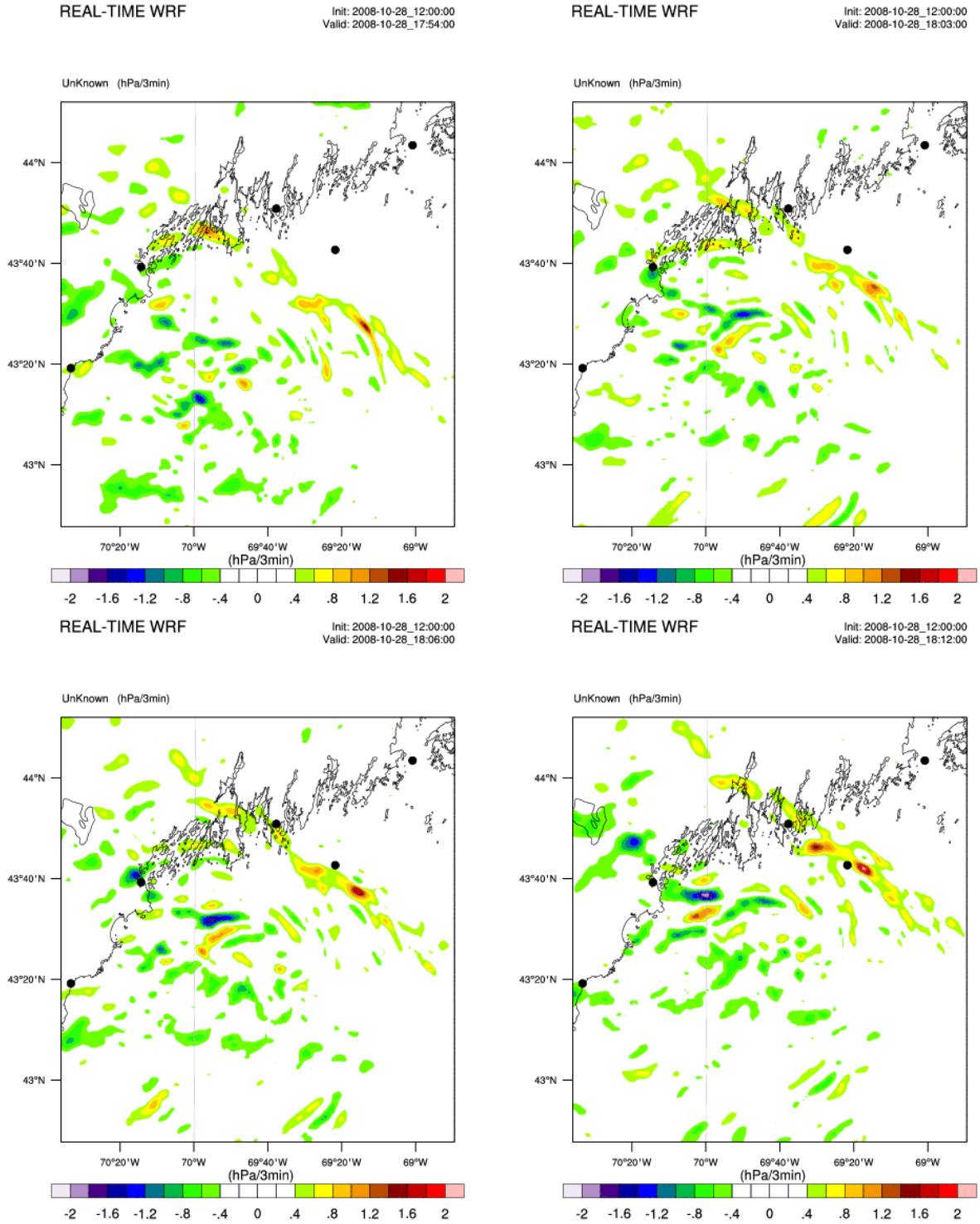

Figure 33: Simulated MSLP tendency (hPa/3min) on 17:54 UTC (top left), 18:03 UTC (top right), 18:06 UTC (bottom left) and 18:12 UTC (bottom right) 28 Oct 2008 for simulations with Kain-Fritch convection scheme and 1-way nesting strategy. Black dots (west-east) denote Wells, Portland, Boothbay, and locations of 44032 and 44033 buoys.

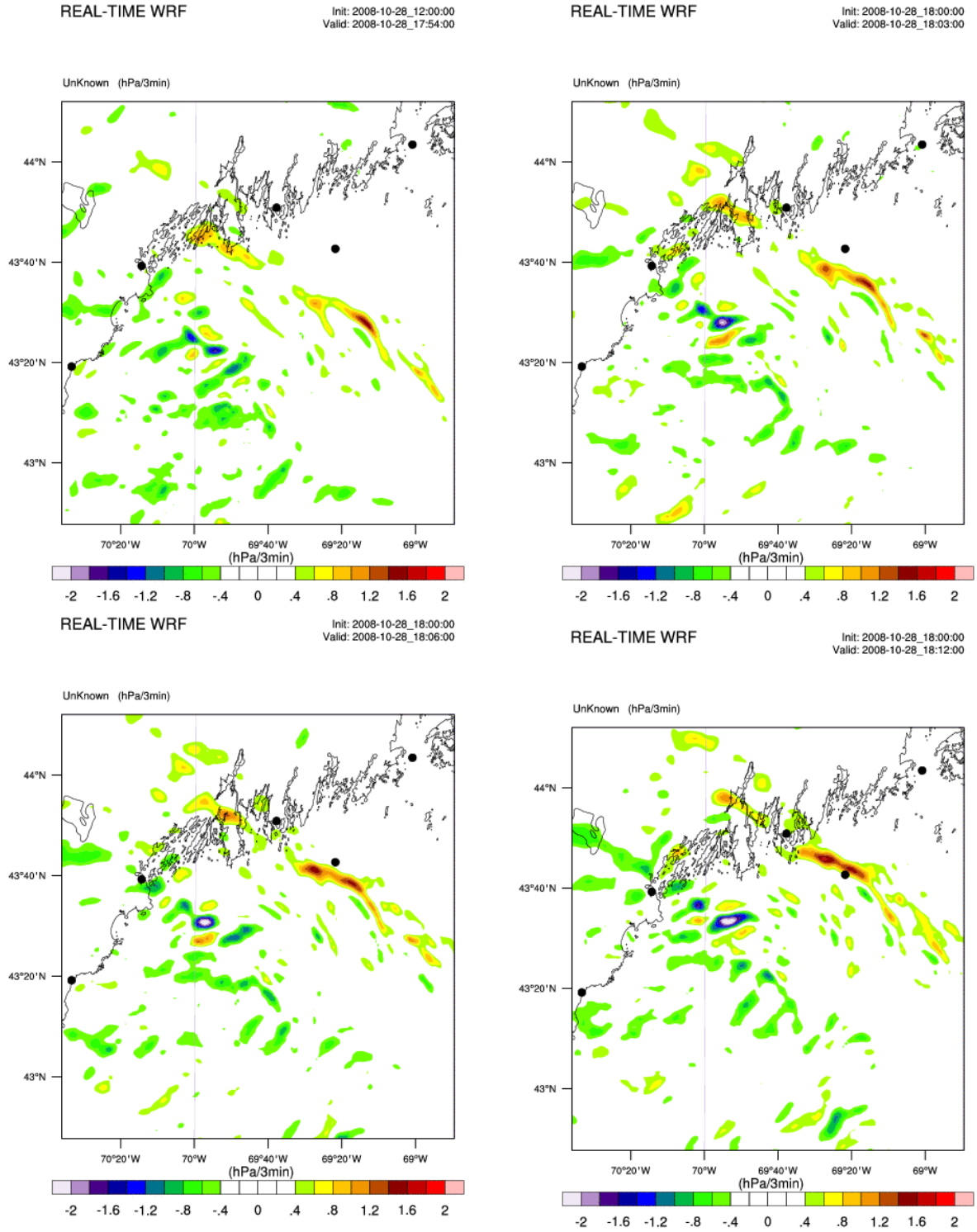

Figure 34: Simulated MSLP tendency (hPa/3min) on 17:54 UTC (top left), 18:03 UTC (top right), 18:06 UTC (bottom left) and 18:12 UTC (bottom right) 28 Oct 2008 for simulations with Kain-Fritch convection scheme and 2-way nesting strategy. Black dots (west-east) denote Wells, Portland, Boothbay, and locations of 44032 and 44033 buoys.

The wave-train approached the shoreline soon after. According to the simulations, the western part of the wave-train, with pressure amplitudes as intensive as 3 hPa, reached the coast some 25 km west of Boothbay shortly after 18 UTC (Figs. 35 and 36). In the next 30 min, as the high-pressure band moved northward, the eastern part of the wave-train was characterized by amplitudes that reached 2 hPa and impinged on the shore closer and closer to Boothbay. Boothbay itself was on the very eastern edge of the simulated wave-train where the pressure oscillations reached 1-1.5 hPa. It appears that a more coherent wave-train in the pressure distribution was found in the 1-way simulation. This is again in contrast to the analysis at 18 UTC, where more organized wave-like pressure pattern near the rear edge of the precipitation system was found in the 2-way nested simulation.

Pressure gradient at times when the western part of the wave-train in pressure distribution reached the area west of Boothbay (shortly after 18 UTC) reached 0.9 hPa/km in the 1-way nested simulation and 0.6 hPa/km in the 2-way nested simulation. Later on, when the eastern part of the wave-train approached Boothbay, maximal pressure gradients reached 0.8 hPa/km in the 1-way nesting simulation and 0.5 hPa/km in the 2-way nesting simulation. The main axis of the pressure gradient lines was WSW-ENE, in accordance with the individual pressure oscillations presented in Figs. 36. and 37.

Pressure tendencies in the western part of the wave-train reached more than +1.2 hPa/3 min and -2.2 hPa/3min in 1-way nesting simulation and slightly less in the 2-way nested simulation. Along the eastern part of the wave-train similar values were found which were again slightly stronger in the 1-way nesting simulation. Again, the wave-train structure was more coherent in the 1-way nesting simulation.

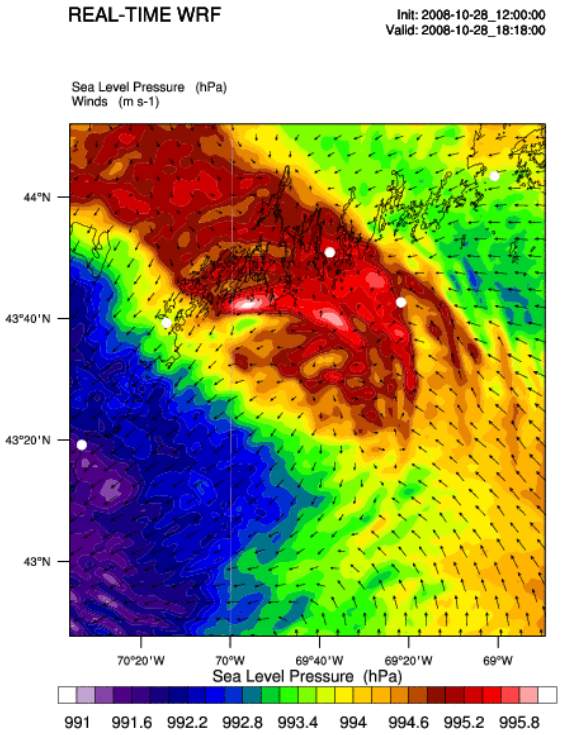
REAL-TIME WRF
Init: 2008-10-28_12:00:00
Valid: 2008-10-28_18:18:00
Sea Level Pressure (hPa)
Winds (m s-1)
44°N
43°40'N
43°20'N
43°N
70°20'W
70°W
69°40'W
69°20'W
69°W
Sea Level Pressure (hPa)
991 991.6 992.2 992.8 993.4 994 994.6 995.2 995.8

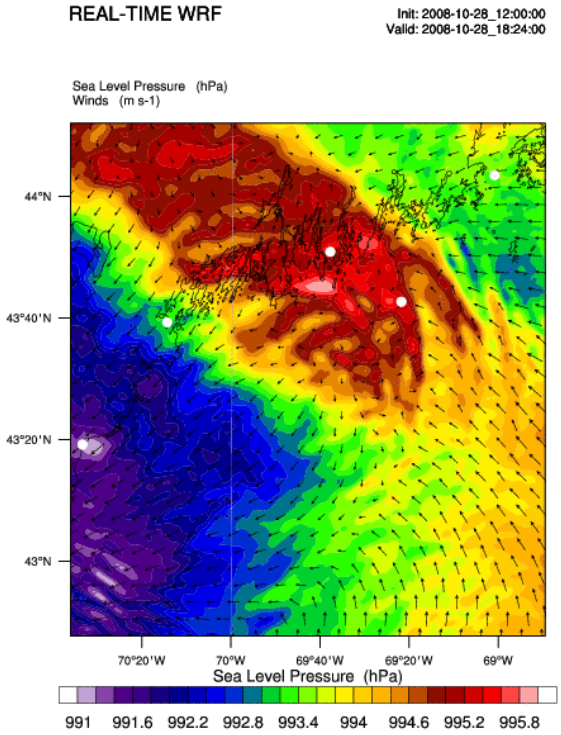
REAL-TIME WRF
Init: 2008-10-28_12:00:00
Valid: 2008-10-28_18:24:00
Sea Level Pressure (hPa)
Winds (m s-1)
44°N
43°40'N
43°20'N
43°N
70°20'W
70°W
69°40'W
69°20'W
69°W
Sea Level Pressure (hPa)
991 991.6 992.2 992.8 993.4 994 994.6 995.2 995.8

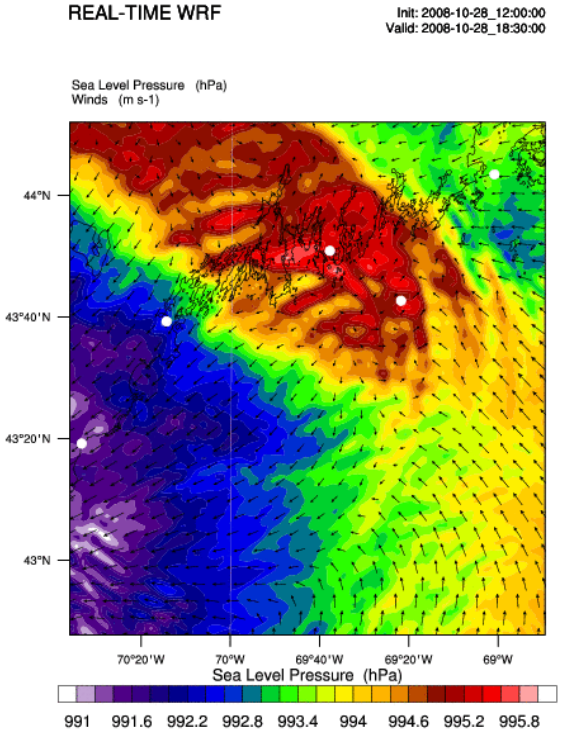
REAL-TIME WRF
Init: 2008-10-28_12:00:00
Valid: 2008-10-28_18:30:00
Sea Level Pressure (hPa)
Winds (m s-1)
44°N
43°40'N
43°20'N
43°N
70°20'W
70°W
69°40'W
69°20'W
69°W
Sea Level Pressure (hPa)
991 991.6 992.2 992.8 993.4 994 994.6 995.2 995.8

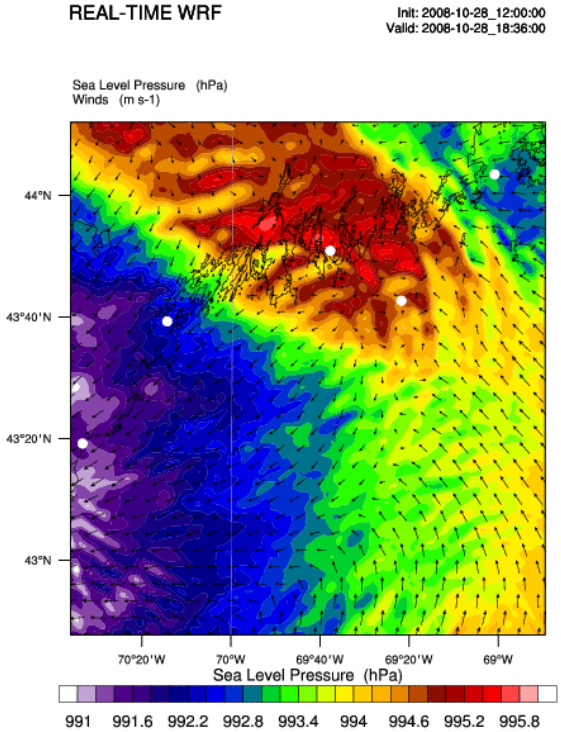
REAL-TIME WRF
Init: 2008-10-28_12:00:00
Valid: 2008-10-28_18:36:00
Sea Level Pressure (hPa)
Winds (m s-1)
44°N
43°40'N
43°20'N
43°N
70°20'W
70°W
69°40'W
69°20'W
69°W
Sea Level Pressure (hPa)
991 991.6 992.2 992.8 993.4 994 994.6 995.2 995.8

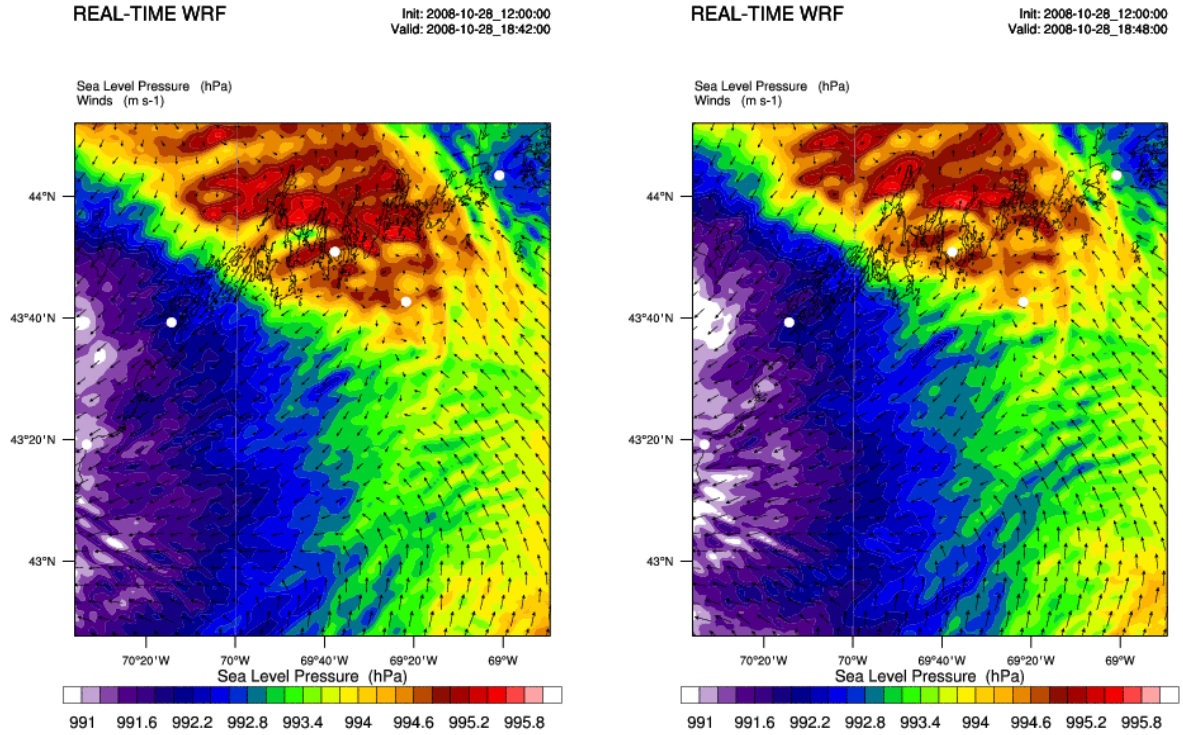

Figure 35: As in Fig. 29., but at 18:18, 18:24 (top), 18:30, 18:36 (middle) and 18:42, 18:48 UTC (bottom) 28 Oct 2008.

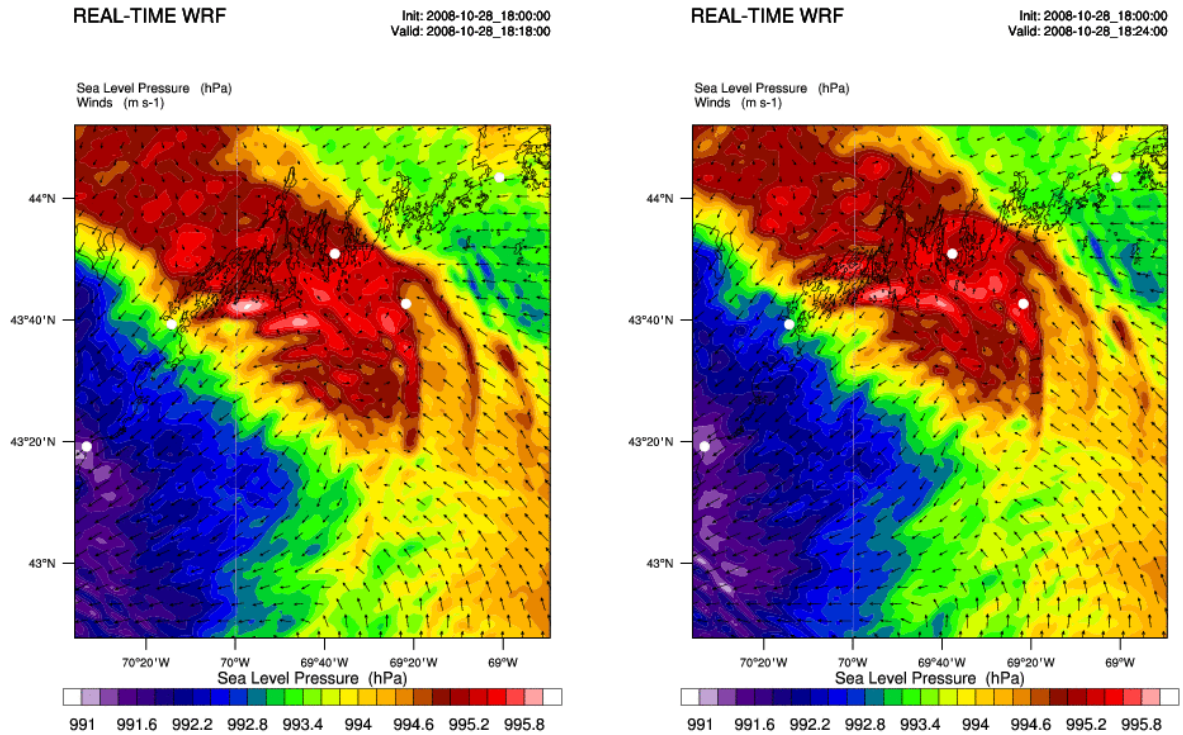

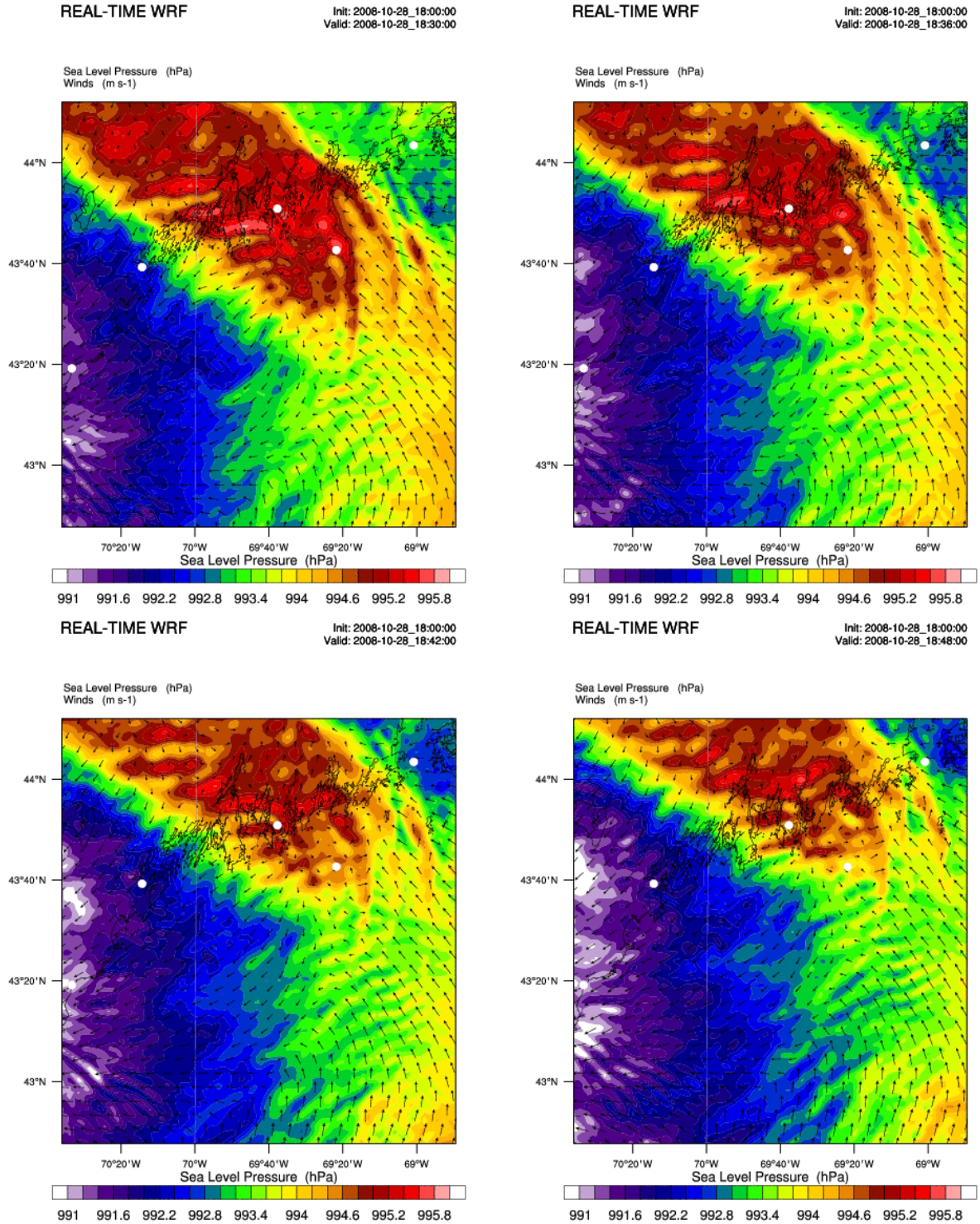

Figure 36: As in Fig. 30., but at 18:18, 18:24 (top), 18:30, 18:36 (middle) and 18:42, 18:48 UTC (bottom) 28 Oct 2008.

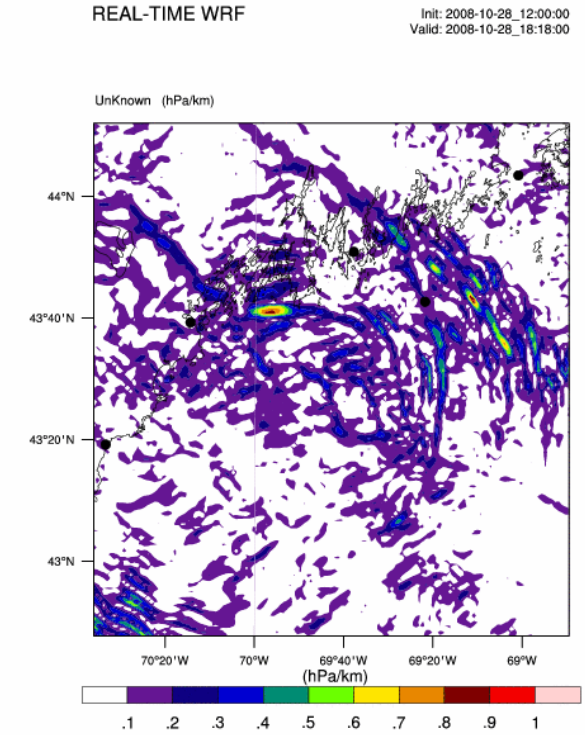
REAL-TIME WRF
Init: 2008-10-28_12:00:00
Valid: 2008-10-28_18:18:00
UnKnown (hPa/km)
44°N
43°40'N
43°20'N
43°N
70°20'W
70°W
69°40'W
69°20'W
69°W
(hPa/km)
.1 .2 .3 .4 .5 .6 .7 .8 .9 1

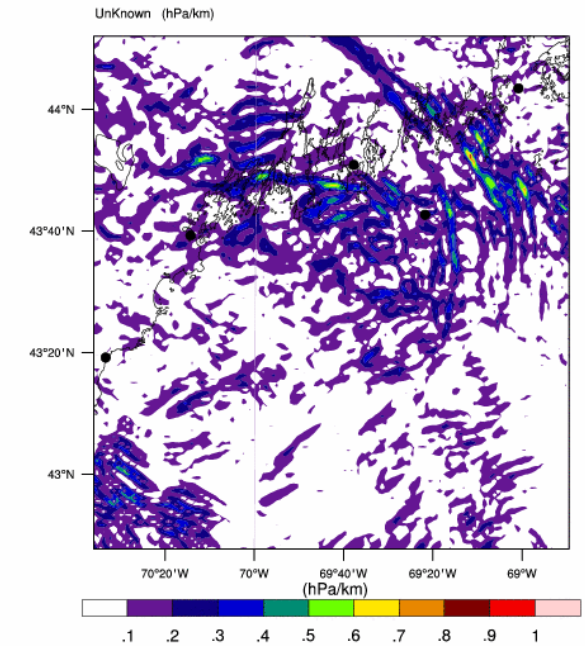
REAL-TIME WRF
Init: 2008-10-28_12:00:00
Valid: 2008-10-28_18:30:00
UnKnown (hPa/km)
44°N
43°40'N
43°20'N
43°N
70°20'W
70°W
69°40'W
69°20'W
69°W
(hPa/km)
.1 .2 .3 .4 .5 .6 .7 .8 .9 1

REAL-TIME WRF
Init: 2008-10-28_12:00:00
Valid: 2008-10-28_18:24:00
UnKnown (hPa/km)
44°N
43°40'N
43°20'N
43°N
70°20'W
70°W
69°40'W
69°20'W
69°W
(hPa/km)
.1 .2 .3 .4 .5 .6 .7 .8 .9 1

REAL-TIME WRF
Init: 2008-10-28_12:00:00
Valid: 2008-10-28_18:36:00
UnKnown (hPa/km)
44°N
43°40'N
43°20'N
43°N
70°20'W
70°W
69°40'W
69°20'W
69°W
(hPa/km)
.1 .2 .3 .4 .5 .6 .7 .8 .9 1

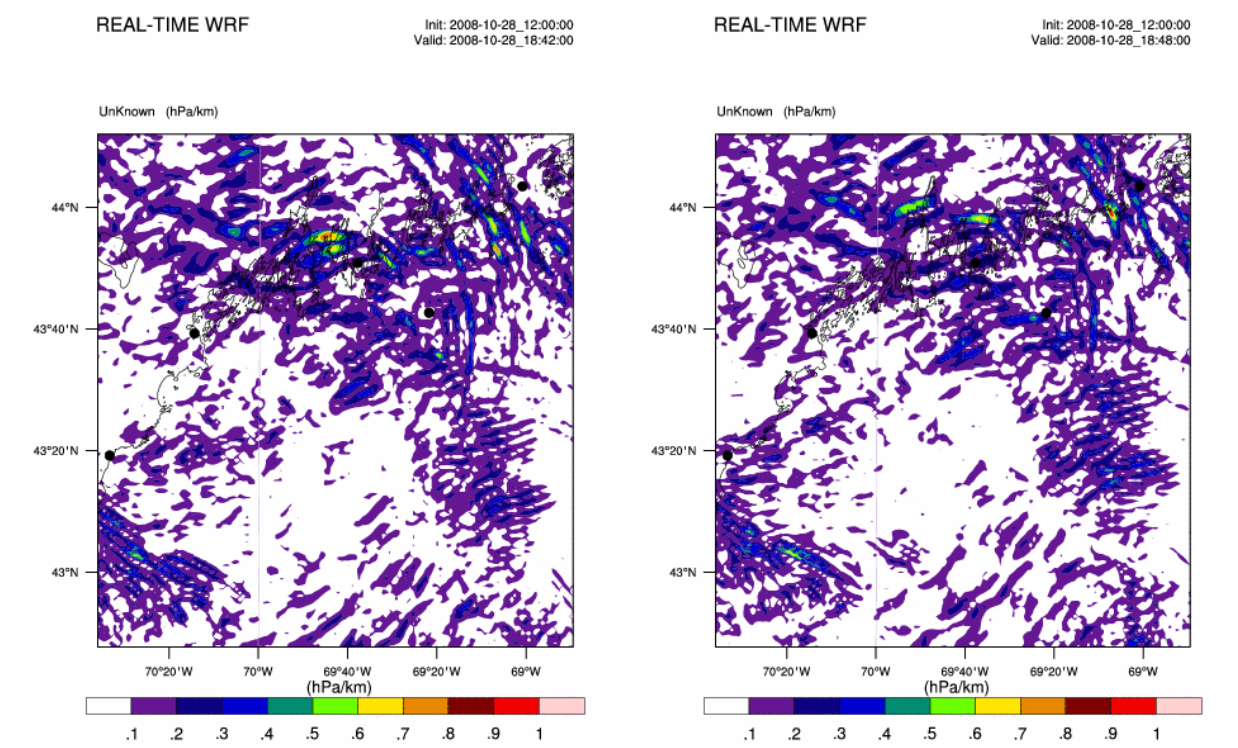

Figure 37: As in Fig. 31., but at 18:18, 18:24 (top), 18:30, 18:36 (middle) and 18:42, 18:48 UTC (bottom) 28 Oct 2008.

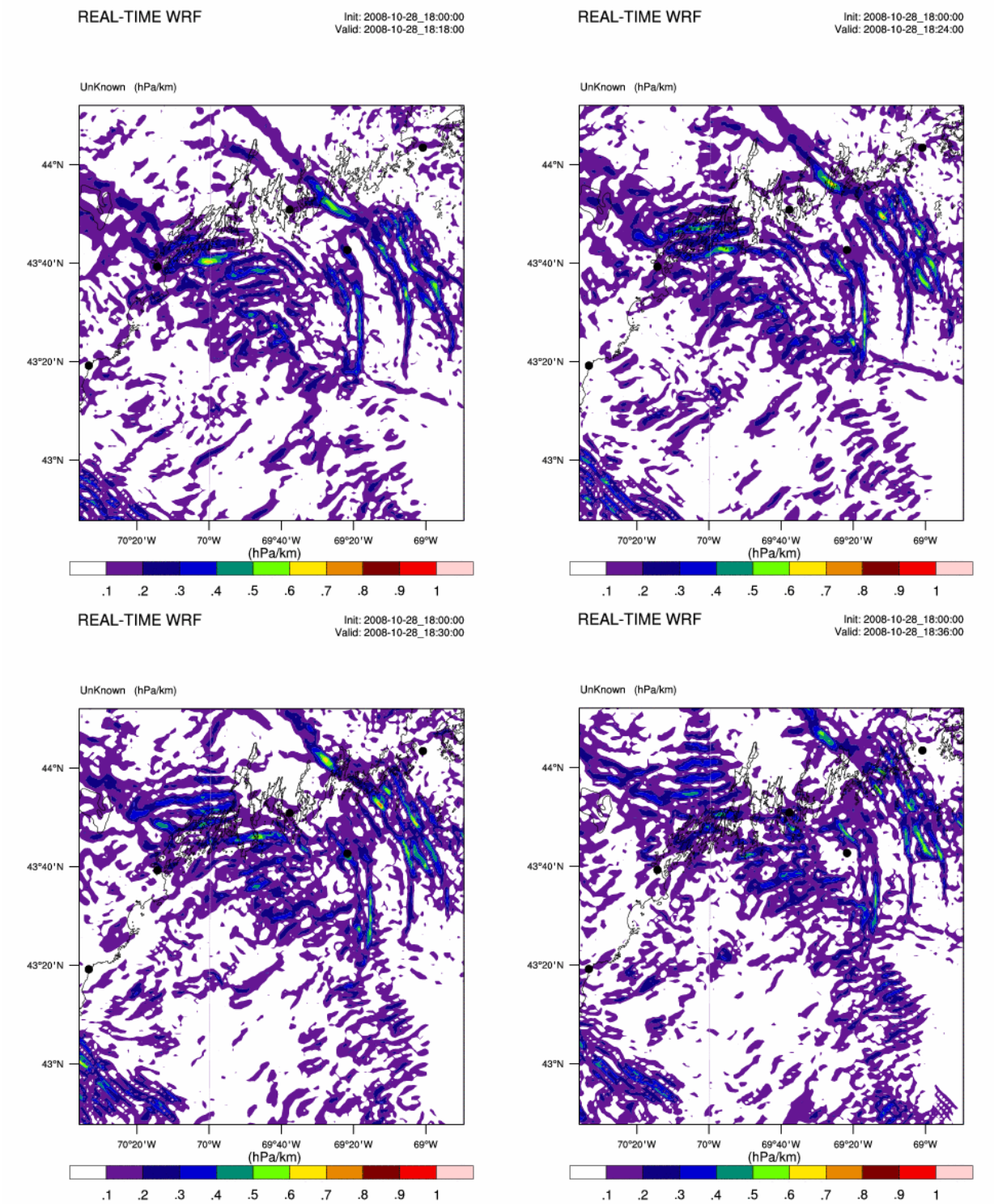
REAL-TIME WRF
Init: 2008-10-28_18:00:00
Valid: 2008-10-28_18:18:00
UnKnown (hPa/km)
44°N
43°40'N
43°20'N
43°N
70°20'W
70°W
69°40'W
69°20'W
69°W
(hPa/km)
.1 .2 .3 .4 .5 .6 .7 .8 .9 1
REAL-TIME WRF
Init: 2008-10-28_18:00:00
Valid: 2008-10-28_18:24:00
UnKnown (hPa/km)
44°N
43°40'N
43°20'N
43°N
70°20'W
70°W
69°40'W
69°20'W
69°W
(hPa/km)
.1 .2 .3 .4 .5 .6 .7 .8 .9 1
REAL-TIME WRF
Init: 2008-10-28_18:00:00
Valid: 2008-10-28_18:30:00
UnKnown (hPa/km)
44°N
43°40'N
43°20'N
43°N
70°20'W
70°W
69°40'W
69°20'W
69°W
(hPa/km)
.1 .2 .3 .4 .5 .6 .7 .8 .9 1
REAL-TIME WRF
Init: 2008-10-28_18:00:00
Valid: 2008-10-28_18:36:00
UnKnown (hPa/km)
44°N
43°40'N
43°20'N
43°N
70°20'W
70°W
69°40'W
69°20'W
69°W
(hPa/km)
.1 .2 .3 .4 .5 .6 .7 .8 .9 1

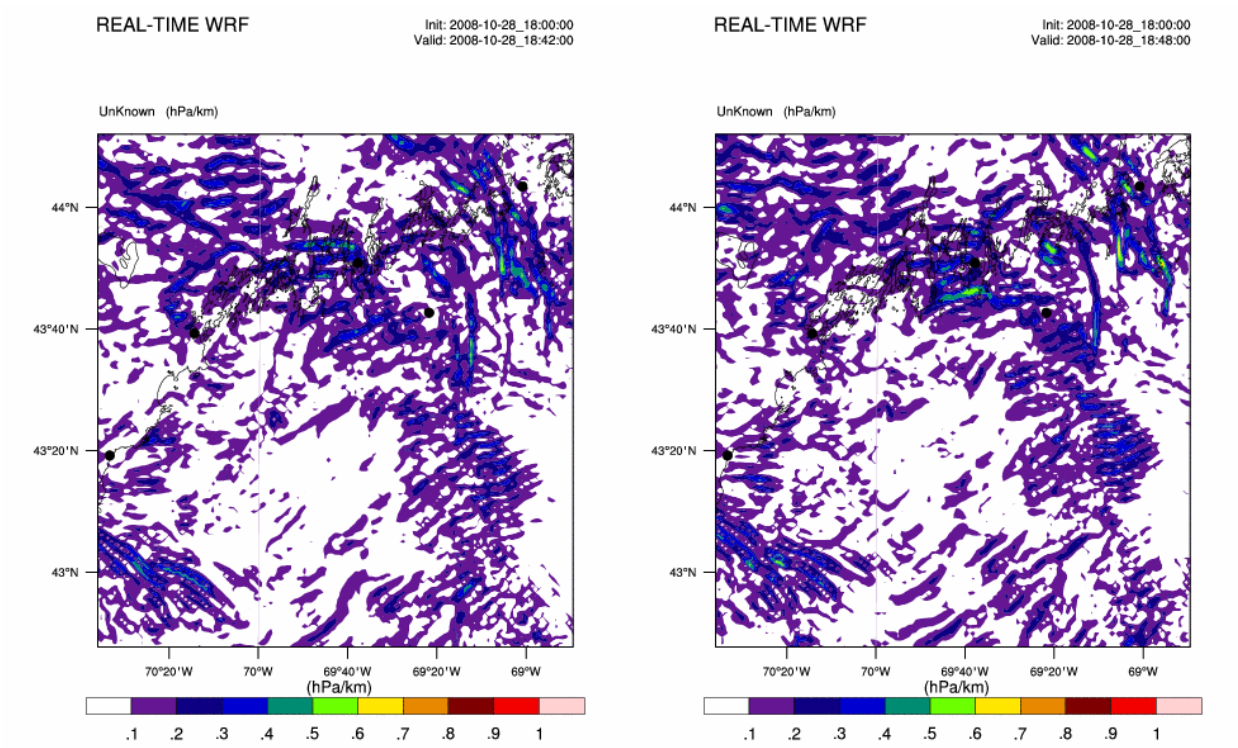

Figure 38: As in Fig. 32., but at 18:18, 18:24 (top), 18:30, 18:36 (middle) and 18:42, 18:48 UTC (bottom) 28 Oct 2008.

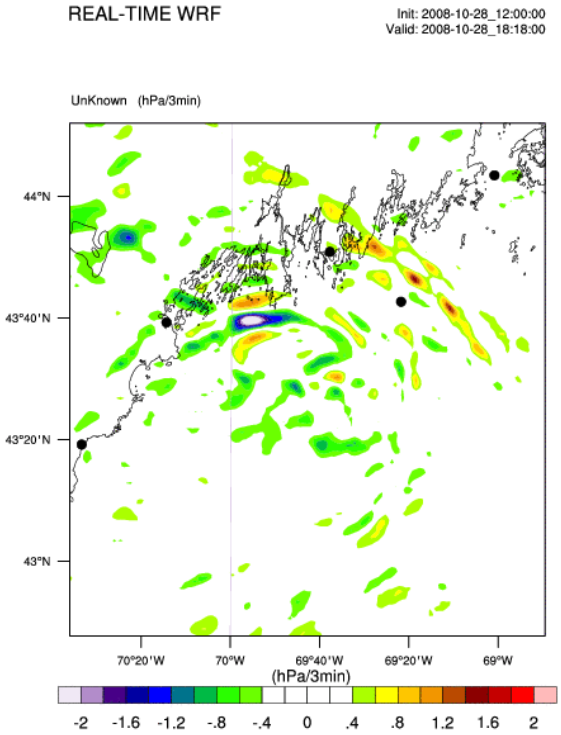
REAL-TIME WRF
Init: 2008-10-28_12:00:00
Valid: 2008-10-28_18:18:00
UnKnown (hPa/3min)
44°N
43°40'N
43°20'N
43°N
70°20'W
70°W
69°40'W
69°20'W
69°W
(hPa/3min)
-2 -1.6 -1.2 -.8 -.4 0 .4 .8 1.2 1.6 2

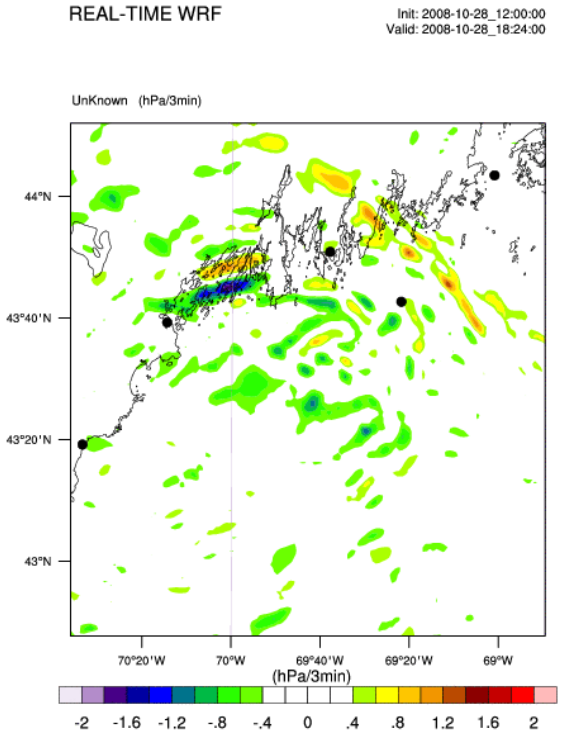
REAL-TIME WRF
Init: 2008-10-28_12:00:00
Valid: 2008-10-28_18:24:00
UnKnown (hPa/3min)
44°N
43°40'N
43°20'N
43°N
70°20'W
70°W
69°40'W
69°20'W
69°W
(hPa/3min)
-2 -1.6 -1.2 -.8 -.4 0 .4 .8 1.2 1.6 2

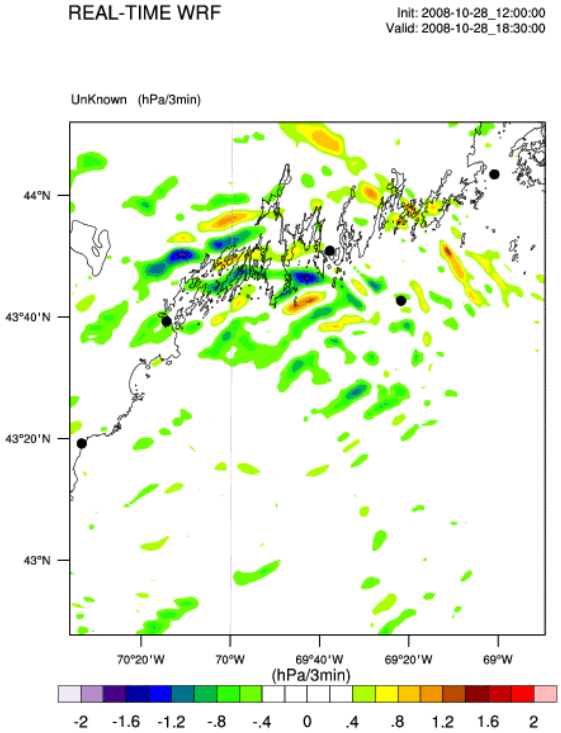
REAL-TIME WRF
Init: 2008-10-28_12:00:00
Valid: 2008-10-28_18:30:00
UnKnown (hPa/3min)
44°N
43°40'N
43°20'N
43°N
70°20'W
70°W
69°40'W
69°20'W
69°W
(hPa/3min)
-2 -1.6 -1.2 -.8 -.4 0 .4 .8 1.2 1.6 2

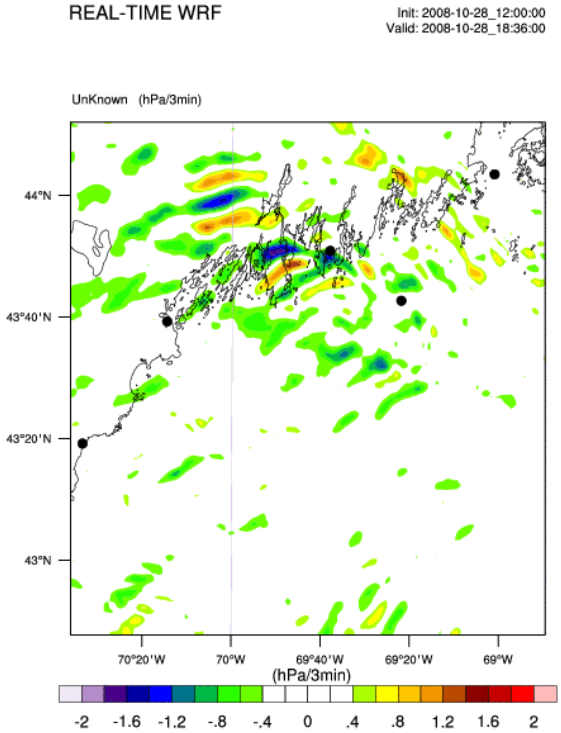
REAL-TIME WRF
Init: 2008-10-28_12:00:00
Valid: 2008-10-28_18:36:00
UnKnown (hPa/3min)
44°N
43°40'N
43°20'N
43°N
70°20'W
70°W
69°40'W
69°20'W
69°W
(hPa/3min)
-2 -1.6 -1.2 -.8 -.4 0 .4 .8 1.2 1.6 2

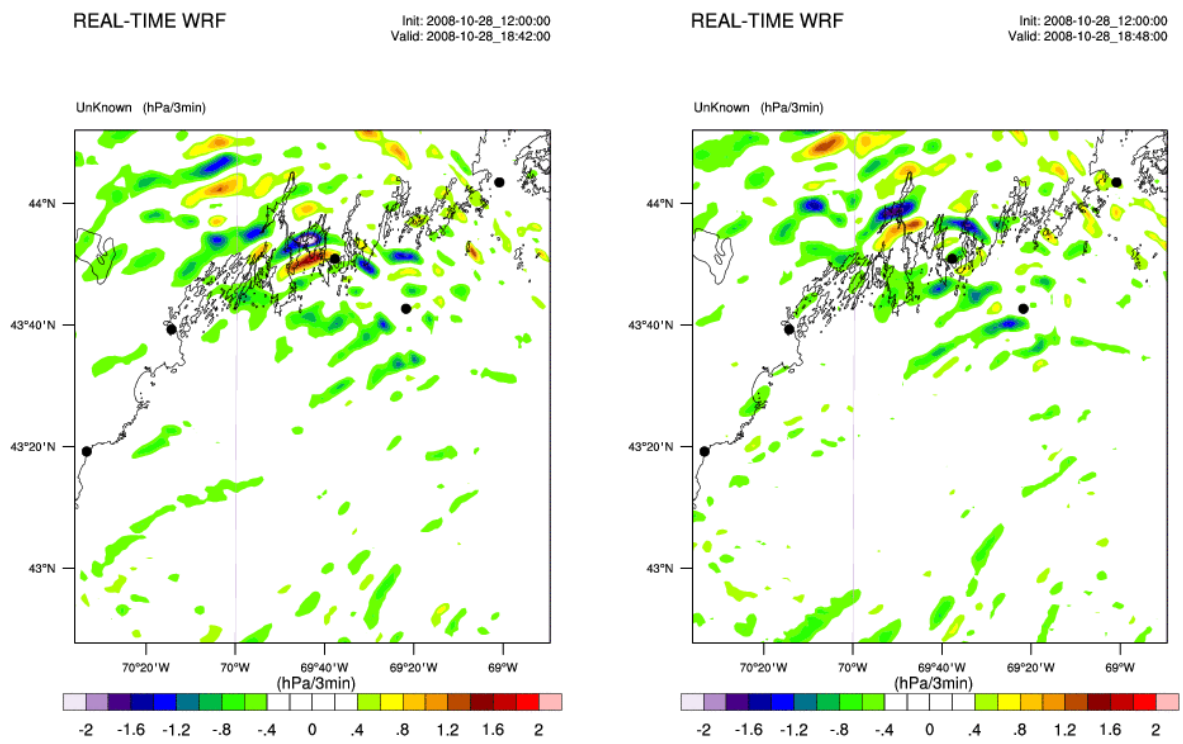

Figure 39: As in Fig. 33., but at 18:18, 18:24 (top), 18:30, 18:36 (middle) and 18:42, 18:48 UTC (bottom) 28 Oct 2008.

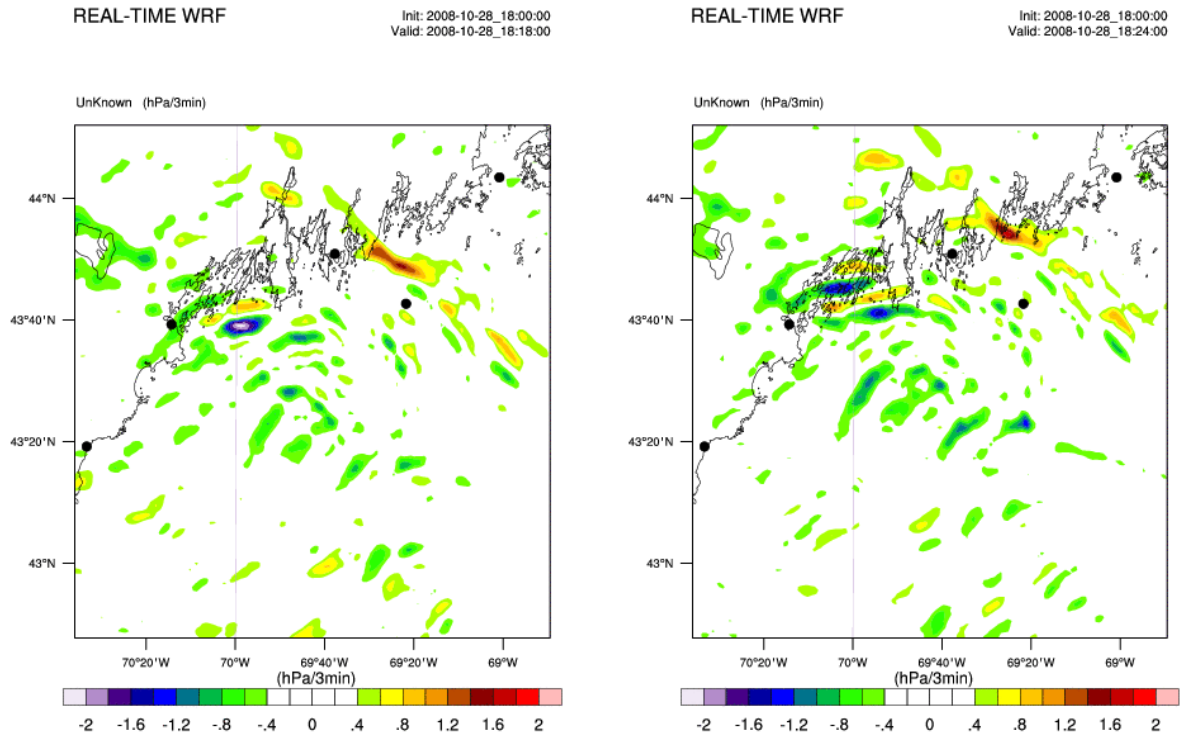

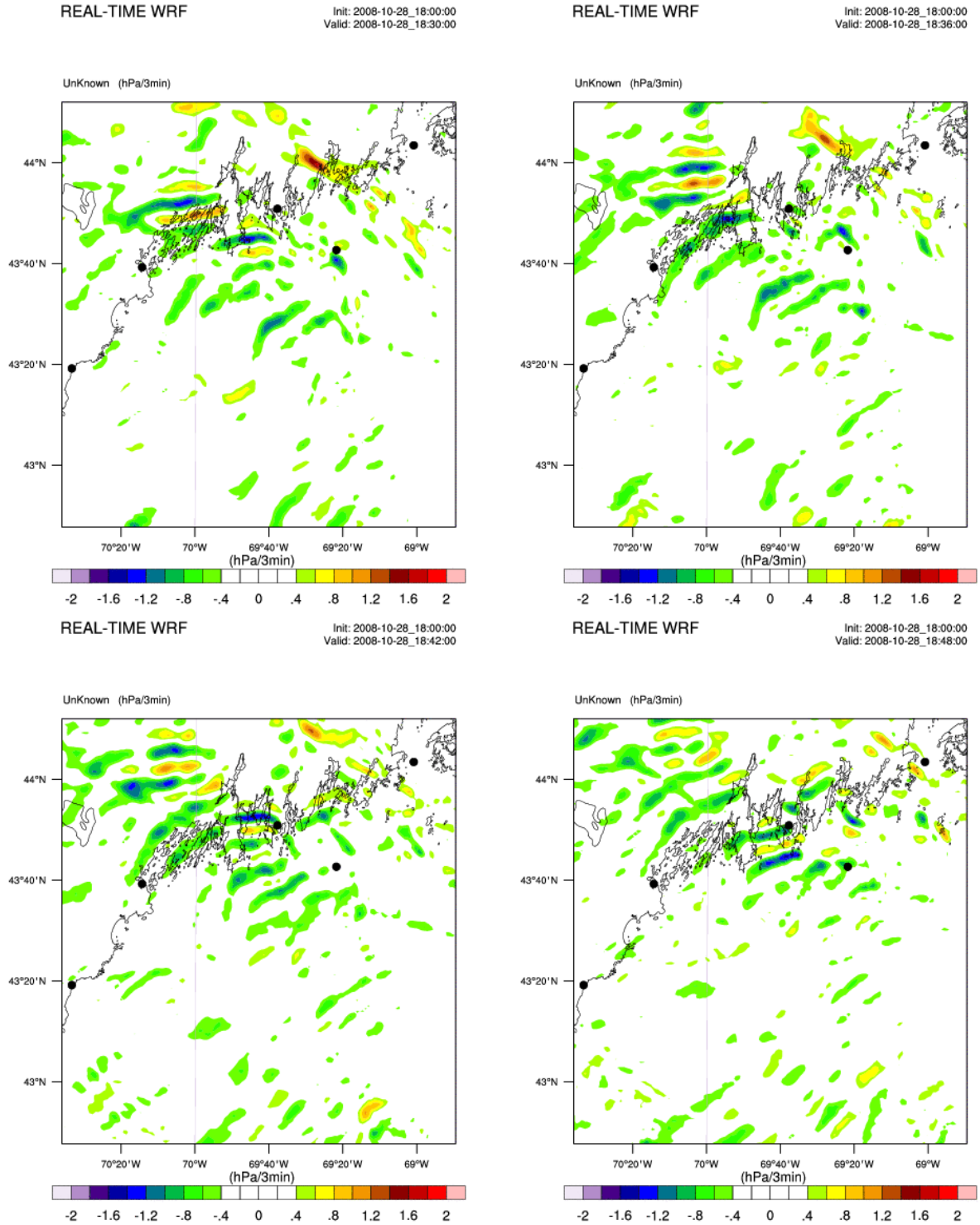

Figure 40: As in Fig. 34., but at 18:18, 18:24 (top), 18:30, 18:36 (middle) and 18:42, 18:48 UTC (bottom) 28 Oct 2008.

7.2 The role of internal gravity waves

The analysis of mean sea level pressure distribution showed that prior to the meteotsunami a wave-train of pressure oscillations formed over the ocean. The wave-train moved towards NNW and crossed the Boothbay area just prior to 19 UTC. This type of wave-train is suggestive of trapped internal gravity waves (IGWs) aloft. Therefore, we 1) investigate whether IGWs were indeed found in the troposphere during the event; and 2) analyze the potential maintenance mechanism, since IGWs which were not maintained would disperse very quickly in the troposphere.

In the low-mid troposphere, simultaneously with the surface pressure oscillations, the isolated wave-train of IGWs approached and moved over the Boothbay area from 18 UTC – 19 UTC (Fig. 41), just prior to the meteotsunami. The wave-length of these IGWs was close to 10-11 km at 2.6 km above sea level (roughly the height were IGWs were most intensive), which is in agreement with the wave-length of pressure oscillations at the surface. Their phase speed, estimated from animations, was close to ~28-30 m/s at 18:30 UTC 28 Oct 2008 and vertical velocities reached over +- 5m/s. Since these IGWs were present (at least) during the entire hour prior to the Boothbay meteotsunami, the issue of the maintenance mechanism needs to be studied further.

The three main IGWs maintenance mechanisms are i) wave-duct, ii) wave-CISK and iii) solitary wave mechanism. As discussed earlier, wave-CISK is not the likely maintenance mechanism, since deep convection was not present during the event, and convective activity was not organized in the same manner as the surface pressure oscillations. Furthermore, the horizontal length-scales and phase speeds of the pressure oscillations (and IGWs aloft) do not fit neither the KdV nor the BDO solitary wave categories. Therefore, we pay special attention to the wave-duct maintenance mechanism.

The vertical cross-section in the direction of propagation of the wave-train (SSE-NNW) showed that both linear and nonlinear IGWs were indeed found just prior to the Boothbay event (Fig. 42). Near the front end of the precipitation system, strong IGWs propagated as high as 9 km, but also quickly dispersed. Near the rear end of the precipitation system, however, IGWs were confined to the mid-troposphere and they were the most intensive at heights somewhat below 3 km. The fact that IGWs propagated in the low- to mid-troposphere but were evanescent in the upper-troposphere was the first indication that the wave trapping might have occurred. The most intensive IGWs within the wave-train

appeared coupled to the rear end of the high-pressure band. It is certain that these IGWs were responsible for the surface pressure oscillations, since they traveled coupled to each other, moved with the same speed and had nearly the same horizontal wave-lengths.

Moist Brunt-Vaisala frequency showed that generally stable layer in low-mid troposphere was topped by weakly stable and statically unstable air aloft (Fig 43.). The bottom base of the statically unstable layer (green shading in Fig. 43) lowered from above ~5km in front of the precipitation zone and high-pressure band, to ~3 km near and behind its rear end. Near the unstable air aloft, the area where moist Richardson number was less than 0.25 was evident (Fig. 44). The layer of Ri<0.25 decreased in the same manner as the bottom of the unstable layer aloft – thus area Ri<0.25 was above ~5 km in front of the pressure disturbance, and lowered to slightly above ~3 km near and behind the rear end of the precipitation system. Farther behind the rear end of the precipitation system, the layer of Ri<0.25 disintegrated, which was not favorable for wave trapping. Indeed, this area is clearly seen on cross-sections as the area where no IGWs were present/maintained.

The critical level for IGWs is studied by means of cross-section-parallel winds and is the level where component of wind speed in the direction of the cross-section reached the phase speed of IGWs. The estimated phase speed of mid-level IGWs and surface pressure oscillations near the rear end of the precipitation system was ~28-30 m/s. These values are therefore also the critical levels for IGWs according to the internal-gravity wave theory described by the Taylor-Goldstein equation.

In front of the mesoscale precipitation system the lower bound of the area where Ri<0.25 was associated with section-parallel component of wind speeds over 30 m/s. In other words, the critical level was in the stable layer below and not in the unstable layer above. Therefore, critical level for IGWs appeared to be in the area where Ri>0.25, showing no potential for wave-trapping. This is consistent with the lack of trapped IGWs in the stable layer in the low- to mid-troposphere in front of the precipitation system and near the front end of the high-pressure band (cf. Fig. 42). Near the rear end of the precipitation system and behind it, however, the wind speeds between ~25 m/s – 30 m/s are found at 3 km ASL fully embedded into the 500 m to 1 km deep layer where Ri<0.25. Therefore, since the estimated phase speed of IGWs is ~28-30 m/s, their critical layer was in the area of Ri<0.25, which therefore might have acted as a reflector for IGWs just below it.

Therefore, according to the linear theory for hydrostatic IGWs (e.g. see Lindzen and Tung, 1976), the

following three necessary for a wave trapping or a wave duct are found in this case: 1) a stable layer within the wave can propagate adjacent to the ground; 2) the stable layer is capped by the unstable layer with Richardson number Ri<0.25; 3) there is a critical layer embedded in the unstable layer. The fourth condition for a duct to occur is that following needs to hold:

$$D/ l_z = 1/4 + n/2; \quad n=0,1,2,...,$$

where D is the depth of the duct layer, and l_z is the vertical wavelength. We can estimate l_z by calculating $l_z = 2\pi(c_p\text{-}U)/N$, where c_p is the phase speed, U is mean wind speed and N is the Brunt-Vaisala frequency. Inferring from above figures, the calculation yields $l_z = 2\pi$(28m/s-20m/s)/sqrt(0.0002/s*s) ~ 3.5 km, which roughly corresponds to the modeled depth of the duct layer (somewhat over 3 km).

Therefore, common atmospheric properties required for a wave duct (Lindzen and Tung, 1976) seem to be fully found near the rear end of the precipitation system.

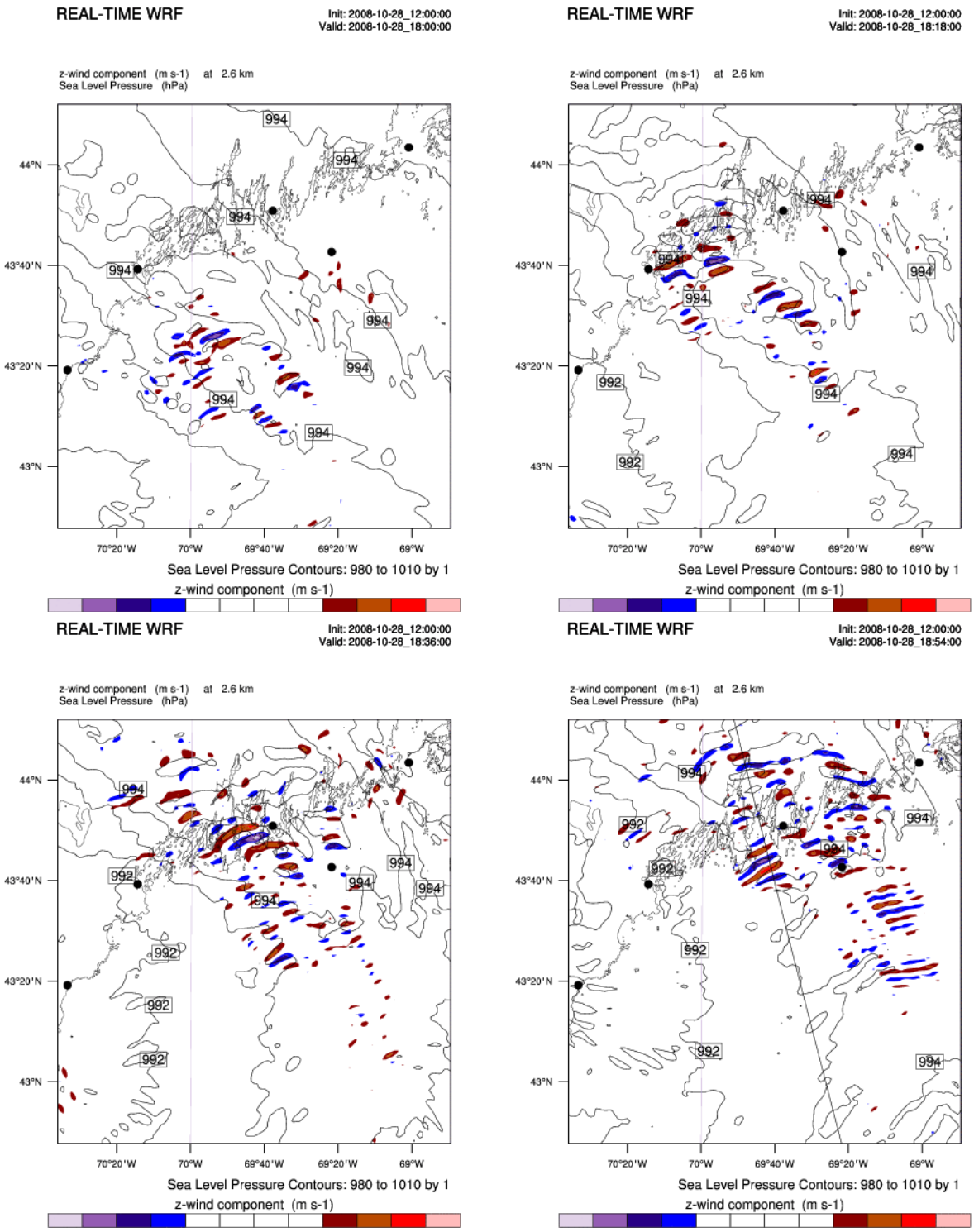

Figure 41: Vertical velocity at 2.6 km ASL (shaded) and MSLP (contours) in WRF simulations with 1-way nesting at 18:00, 18:18, 18:36 and 18:54 UTC. Black strait line denotes cross-sections on Figs. 42-44.

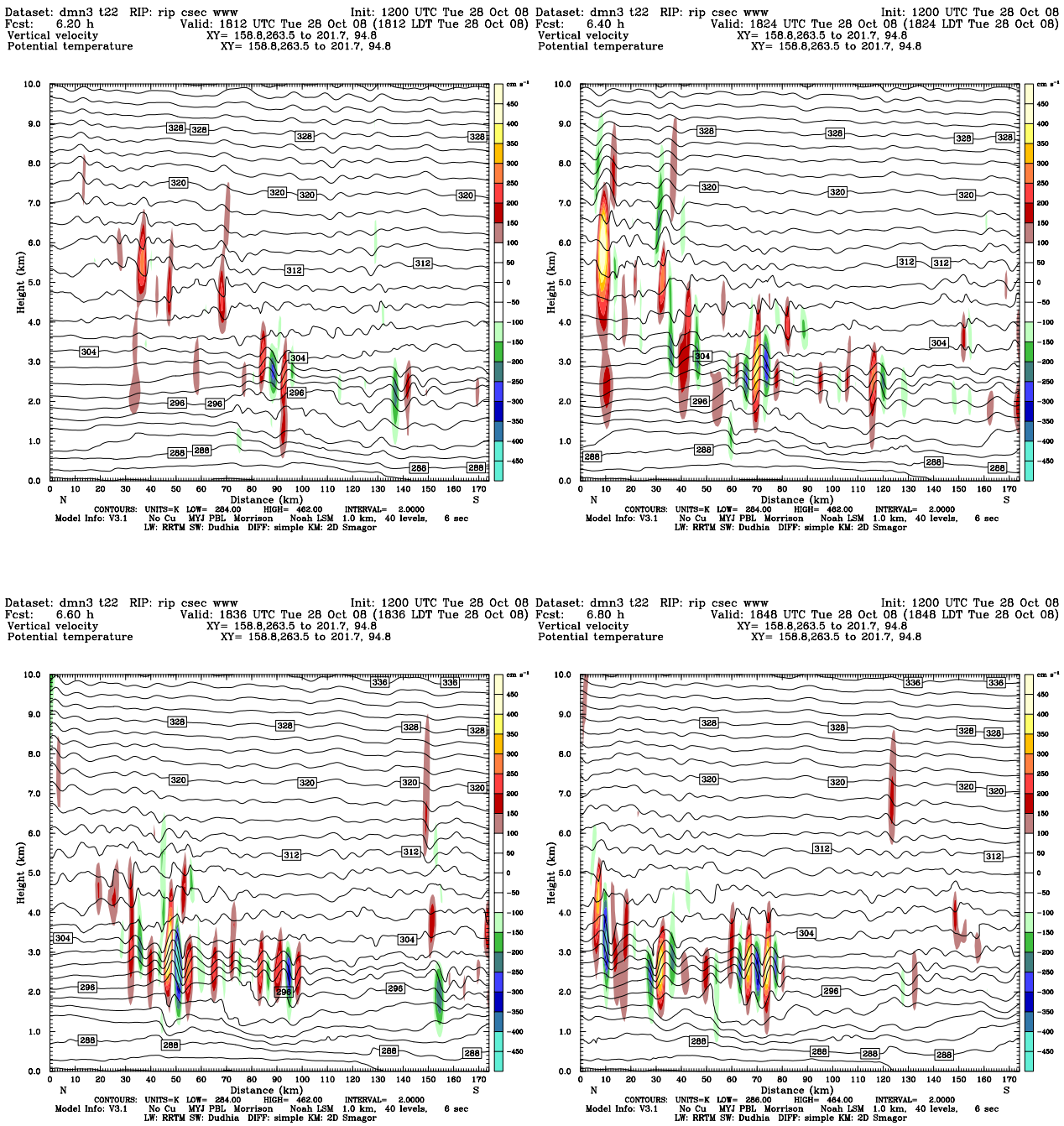

Figure 42: Potential temperature and vertical velocity (shaded) at 18:12, 18:24 (top) and 18:36, 18:48 UTC (bottom) in 1-way nesting simulation. Boothbay harbor is on ~40 km of the x-axis. Cross-section is denoted on Fig. 41.

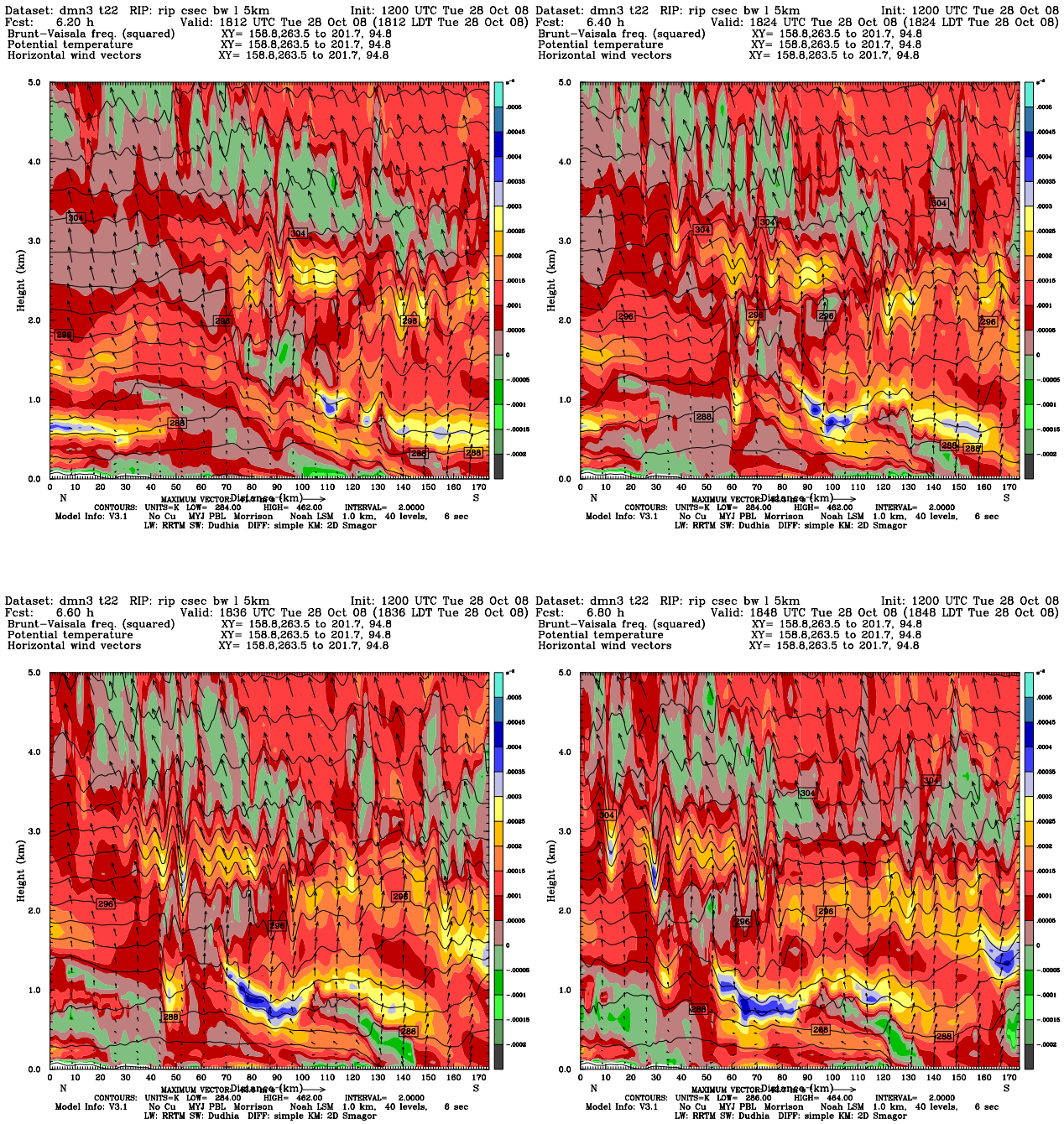

Figure 43: Potential temperature (black contours), moist Brunt-Vaisalla frequency (squared, shaded) and horizontal wind vectors at 18:12, 18:24 (top) and 18:36, 18:48 UTC (bottom) in 1-way nesting simulation. Boothbay harbor is on ~40 km of the x-axis. Cross-section is denoted on Fig. 41.

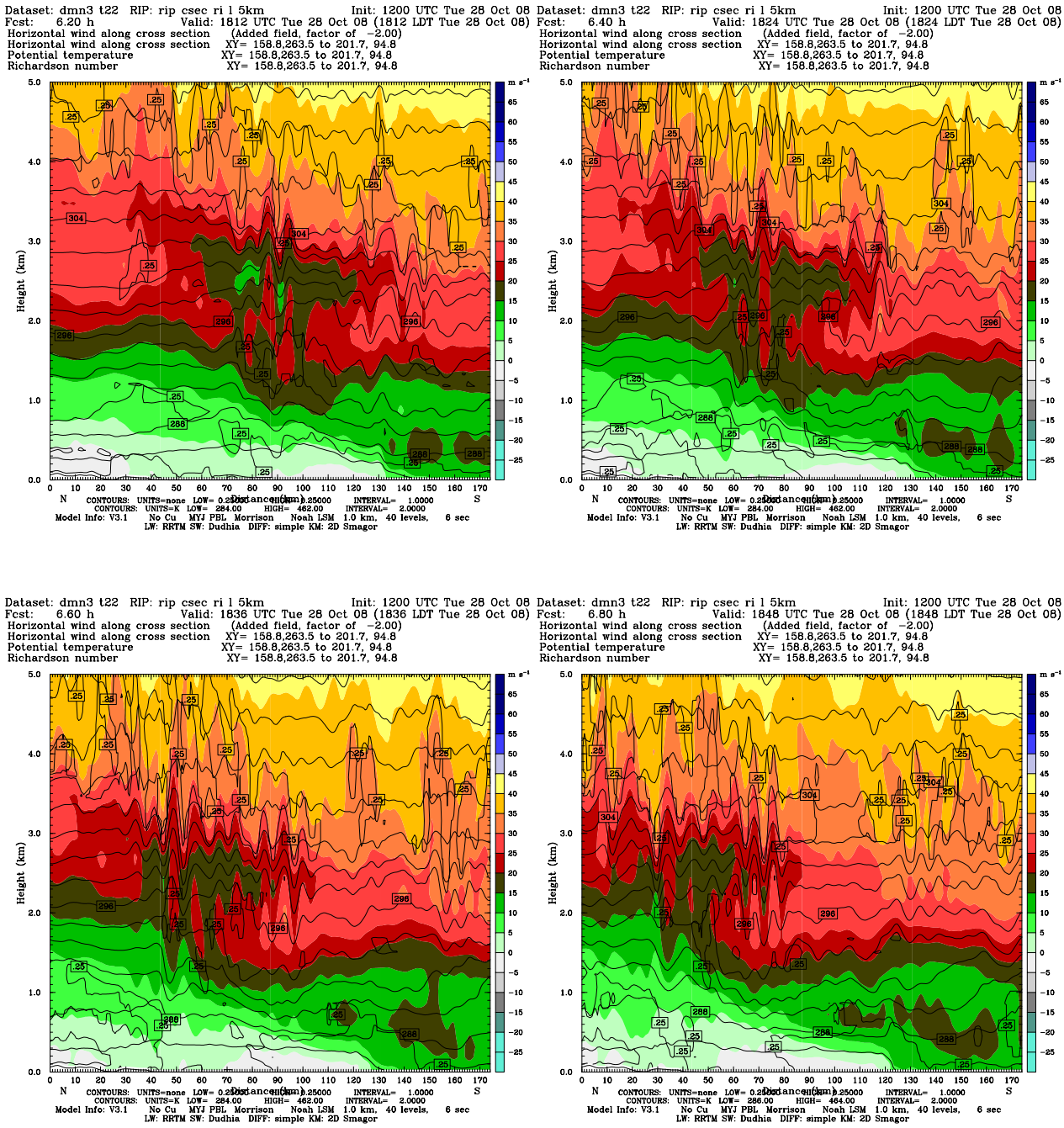

Figure 44: Potential temperature (black thin contours), Richardson number (black thick contour of Ri=0.25 only) and component of wind speed parallel to the cross-section (shaded) at 18:12, 18:24 (top) and 18:36, 18:48 UTC (bottom) in 1-way nesting simulation. Boothbay harbor is on ~40 km of the x-axis. Cross-section is denoted on Fig. 41.

8. Conclusions

Simulation of rapid short-wavelength pressure oscillations is challenging for mesoscale models and different simulations performed showed a large scatter of results. According to performed verification with in-situ, remote sensing and reanalysis data, WRF simulation with initial and lateral boundary conditions from ECMWF operational analysis (ECMWF-OA) seemed to perform better than simulations initiated with NARR and ERA-Interim reanalysis data. In fact, only simulations initialized with ECMWF_OA reproduced the precipitation zone and the associated high-pressure band moving over the Boothbay harbor and traveling from SSE-NNW. Furthermore, the gross properties of mesoscale simulations were very sensitive to increasing the length of the simulation (simulation time-horizon) suggesting the low predictability of this type of events. The choice of microphysics or convection schemes, and the type of nesting strategy (one-way or two-way) was not crucial for simulations of the gross mesoscale properties of the moving squall line. However, simulations of the wave-train of the surface pressure oscillations near the rear end of the high-pressure band were highly sensitive to the type of the convection scheme chosen. In addition, the type of feedback also showed very important for simulating the exact details of the related oscillatory surface pressure distribution.

The traveling precipitation system that moved over the Boothbay area was associated with the surface high-pressure band, whose timescale was ~35 min, spatial scale ~50 km, and the speed of propagation 20-22 m/s. The passage of the high-pressure band was associated with a persistent pressure jump near its front end and the sustained pressure oscillations near its rear end. The pressure jump reached 2 hPa, causing mean sea level pressure gradients of 0.8 hPa/km and pressure tendencies of 2.0 hPa/3min. The amplitude of pressure oscillations near the rear end of the precipitation system were even stronger and reached close to 3 hPa, with maximal pressure gradients of 0.9 hPa/km and tendencies of 2.5 hPa/3 min. The surface pressure oscillations were directly coupled to the internal gravity waves in mid-troposphere (~3 km) near and behind the precipitation system. The wave-length of both pressure oscillations and IGWs were 10-11 km and their speeds were 28-30 m/s.

The low- to mid- troposphere above near-surface pressure oscillations near the rear end of the precipitation system was a duct layer which enabled the maintenance of IGWs and consequently the surface pressure oscillations. This is evidenced by the layer of unstable air above ~3 km with $Ri<0.25$ and embedded environmental critical level for phase speeds in range ~28-30 m/s, as well as the required depth of the duct layer. Finally, the radar imagery suggests that the Boothbay meteotsunami,

which occurred around 19 UTC, arose near the rear end of the precipitation system. Therefore, it appears that pressure oscillations due to IGWs are likely the main feature of atmospheric conditions related to generation of the Boothbay meteotsunami.

In summary, the numerical weather prediction of atmospheric conditions related to meteotsunamis is attainable but challenging. It is encouraging that provided the right ICs and LBCs, the mesoscale models may, in addition to mesoscale conditions favorable for wave trapping, reproduce also the surface pressure jumps as well as wave-trains of IGWs and related surface pressure oscillations. However, the success of mesoscale models according to this study appears limited to very short-range forecasting, most advanced parametrization schemes, and very high-resolution grid spacing.

Acknowledgements: This work on this report was funded by the National Weather Service (NWS), National Oceanic and Atmospheric Administration (NOAA), U.S. Department of Commerce Meteotsunami Warning Project grant NOAA-NWS-NWSPO-2011-2002833. Meteorological and Hydrological Service is acknowledged for the use of HPC resources. A special thanks to John Jensenius, John Cannon, and Linda Mangum for providing the radar imagery and buoy data missing from the on-line database.